Determination of the Berry Phase in the Staggered Loop Current Model of the Pseudogap in the Cuprates

Etienne Bolduc

Department of Physics

McGill University, Montreal, Canada

August 2019

A thesis submitted to McGill University in partial fulfillment
of the requirements of the degree of Master of Science

ACKNOWLEDGEMENTS

I would like to thank my thesis supervisor Prof. Tami Pereg-Barnea for her endless patience, her insightful remarks, and her crucial advice, which have all been essential to the writing of this document; she was able to make me see things from different perspectives whenever I needed it. Furthermore, I would like to thank my parents and my friends for their kindness and understanding throughout the whole process, my roommates for their lenience, and Mika for the constant support.

ABSTRACT

High-temperature superconductivity in the cuprates has been at the heart of many debates since its discovery more than 30 years ago. No consensus has been reached yet about the underlying physics, but plausible descriptions usually fall into two categories each carrying various propositions. The quantum oscillations data acquired over the past few years for the normal state of the cuprates under a strong magnetic field has recently been used to obtain the electronic Berry phase of different compounds, which manifests through the phase mismatch in quantum oscillations [13]. This analysis revealed an electronic Berry phase of 0 mod 2π in three hole-doped compounds and $1.4\pi \mod 2\pi$ in one electron-doped compound. To investigate mysterious pseudogap phase of the cuprates, the theoretical candidate known as the circulating current state of Varma [51] as approached by Bulut [7] is analyzed to numerically evaluate through a semiclassical approach the electronic Berry phase in this normal state. Under a typical parameter set in line with experimental data, a phase of π is found. A comparison of the semiclassical approach with the Peierls substitution applied to this model confirms this result and further leads to an uncertainty on the phase of order 0.01π. Hence, the circulating current state is incompatible with quantum oscillations data according to the Berry phase.

ABRÉGÉ

La supraconductivité à haute température dans les cuprates a été au coeur de plusieurs débats depuis sa découverte il y a plus de 30 ans. Aucun consensus n'a été établi jusqu'à maintenant à propos de la physique sous-jacente, mais les descriptions plausibles sont généralement classées sous deux catégories possédant chacune diverses propositions. Les données acquises au cours des dernières années sur les oscillations quantiques pour l'état normal des cuprates sous un fort champ magnétique ont récemment été utilisées pour obtenir la phase électronique de Berry de différentes substances, se manifestant à travers le déphasage des oscillations quantiques [13]. Cette analyse a révélé une phase électronique de Berry de $0 \mod 2\pi$ dans trois substances dopées aux trous et de $1.4\pi \mod 2\pi$ dans une substance dopée aux électrons. Pour étudier la mystérieuse phase pseudogap des cuprates, le candidat théorique connu comme étant la phase de courant circulant de Varma [51] tel qu'approché par Bulut [7] est analysé pour évaluer numériquement au travers d'une approche semi-classique la phase électronique de Berry de cet état normal. En fonction d'un ensemble typique de paramètres s'accordant avec les données expérimentales, une phase de π est trouvée. Une comparaison de l'approche semi-classique avec la substitution de Peierls appliquée à ce modèle confirme ce résultat et implique additionellement une incertitude quant à la phase de l'ordre de 0.01π. Par conséquent, la phase de courant circulant est incompatible avec les données d'oscillations quantiques en terme de la phase de Berry.

TABLE OF CONTENTS

LIST OF TABLES

LIST OF FIGURES

1. INTRODUCTION

For transparency purposes: this work is based on Massarelli's thesis [29] as the methods are almost identical in both cases, although the theoretical models investigated are different.

1.1. Cuprates

High-temperature superconductivity was first detected in $La_{2-\delta}Ba_{\delta}CuO_4$ by Bednorz and Müller in 1986 [4]. The family of copper-oxide compounds sharing similar properties known as *cuprates* has since then been extensively studied and still is an open field of research. Indeed, no agreement has been reached yet in the scientific community over various parts of the phase diagram [32, 43], shown in figure 1.3.

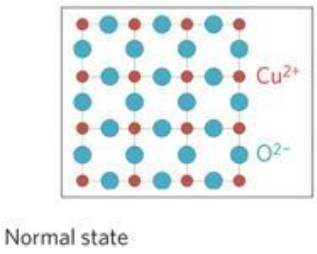

Figure 1.1: Crystal structure of a CuO_2 plane in cuprates. The lattice spacing typically ranges from 3.7 Å to 3.9 Å depending on the doping, the compound, and the axis in some cases [41]. Reproduced from [18].

Cuprates consist of CuO_2 planes stacked one on top of the other with spacer layers in-between, forming a three-dimensional compound similar to what is found in figure 1.1. As superconductivity in cuprates is believed to be mostly confined to the CuO_2 planes, these compounds are regarded as quasi-two-dimensional in their superconductive state [18]. The crystal structure of such materials slightly differs depending on their electron doping, as shown in figure 1.2. Although the models considered later may be employed in more general cases than those addressed, hole-doped compounds will be the main center of interest.

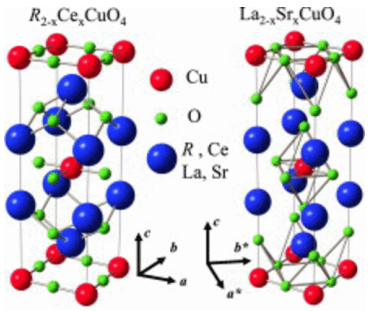

Figure 1.2: Crystal structure of (left) an electron-doped and (right) a hole-doped cuprate. Three CuO_2 layers are visible in both structures with R a placeholder for potential rare-earth ions. Different orientations of the CuO_2 plane are shown. Reproduced from [2].

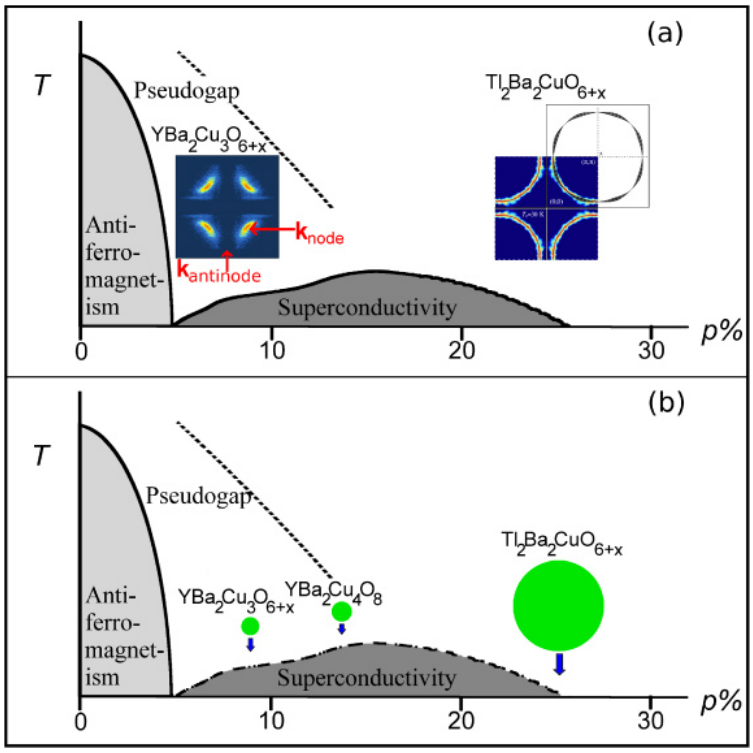

Figure 1.3: Phase diagram as a function of doping p and temperature T of hole-doped cuprates. (a) Fermi surfaces at zero magnetic field obtained in photoemission experiments for an underdoped and an overdoped compound. The location of a node and of an antinode in the Brillouin zone are shown. (b) Relative area of Fermi surfaces for compounds with different dopings according to quantum oscillations experimental data. The dashed line denotes the boundary of the superconducting dome at zero field. Reproduced from [43]; see references therein for experiments.

1.2. The Cuprates' Phase Diagram

An antiferromagnetic Mott insulator dome extending up to about 5% hole-doping is observed in the cuprates' phase diagram [32, and therein], as seen in figure 1.3. Electronic interaction is the cause of such an insulating phase. However, copper sites in undoped cuprates possess an odd number of electrons: a metallic state is thus expected according to simple band theory and because of the half-filled band represented in figure 1.4.

For higher doping, a superconducting dome with high critical temperature T_c is found more or less between 5% and 25% hole-doping. We call *optimal doping* the point where the highest T_c is attained while *overdoped* and *underdoped* are used to denote the regions respectively above and below this point. The optimal doping approximately occurs at 15% doping. Some properties of the BCS theory have been detected in the superconducting phase of cuprates, such as a Cooper pairs condensate with long-lifetime quasiparticle-like

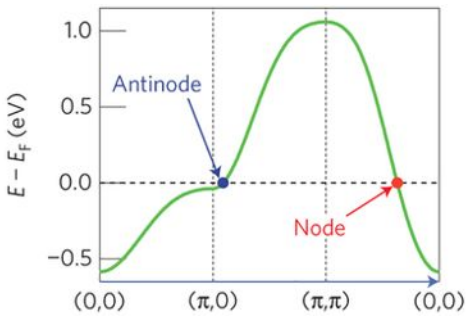

Figure 1.4: Schematic of the dispersion relation along high-symmetry directions in the Brillouin zone for cuprates. The node and the antinode are shown. Reproduced from [18].

excitations that have Bogoliubov-type dispersion relations [32, and therein]. However, contrary to the s-wave symmetry found in typical BCS superconductors [3], a d-wave symmetry is observed in the Cooper pairing and the superconducting gap function [18]. Accordingly, *nodal* and *antinodal* are used to denote the corresponding locations in the Brillouin zone of the d-wave symmetric superconducting gap function, as shown in the inset of figure 1.3 (a).

ARPES measurements above T_c in the overdoped region [43, and therein] show that the Fermi surface is hole-like and quite large since it covers more than half of the Brillouin zone, as pictured in figure 1.3. This result matches the band structure calculations found in figure 1.4 [43, and therein], which is in line with the fact that cuprates are in a simple Fermi liquid state within this regime [2, 32, 43].

Nonetheless, the mystery surrounding the cuprates concerns the underdoped region of the phase diagram, more specifically the state directly above superconductivity called the normal state [32, 43]. ARPES measurements above T_c in the underdoped region and up to 20% doping [43, and therein] show that the Fermi surface is disjoint, taking the form of Fermi arcs at the nodal regions of the Brillouin zone like in figure 1.3. Additionally, quantum oscillations experiments have led to the observation of a Fermi surface much smaller than the one in the overdoped region: it only covers about 2% of the Brillouin zone for underdoped $YBa_2Cu_3O_{6+x}$ [43, and therein].

Moreover, part of the underdoped normal state is in what is known as a *pseudogap phase*: this expression is commonly used although it is still unclear if it is a true thermodynamic phase. In BCS superconductors, the s-wave gap emerges at T_c; in underdoped cuprates, the d-wave gap starts appearing as a pseudogap at $T^* > T_c$ as noted in figure 1.3 to gradually attain its full range at T_c [32].

The functional form of the d-wave gap below T_c appears in figure 1.5: around the hole-like Fermi surface's boundary seen on the right of figure 1.3 (a), it vanishes at the nodes while it attains its maximum at the antinodes — respectively when $|k_x| = |k_y|$ and when $k_x = 0$ or $k_y = 0$. Experiments have shown that the gap slowly closes starting at the nodes as the temperature increases above T_c to completely vanish at T^* [18, and therein]. As a matter of fact, the Fermi arcs of the pseudogap phase take their origin from these extended ungapped regions centered at the nodes.

Additionally, the pseudogap phase of underdoped cuprates has been shown to display many unusual properties [32], such as magnetic, transport, thermodynamic, and optical properties. Notably, resistivity depends linearly on temperature over a wide range [28] while time-reversal symmetry breaking in this phase has seemingly manifested through neutron scattering [15] and Kerr effect [53] experiments.

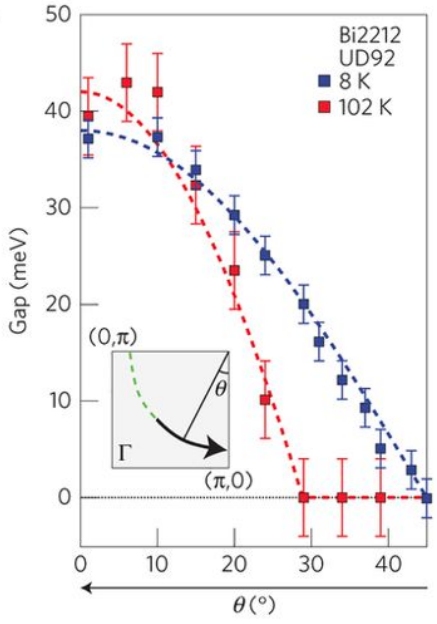

Figure 1.5: Energy gap as a function of angle θ in the Brillouin zone of underdoped $Bi_2Sr_2CaCu_2O_{8+\delta}$ where $T_c = 92\,\mathrm{K}$ at $8\,\mathrm{K}$ and $102\,\mathrm{K}$. The inset shows the geometry of θ. Reproduced from [18].

1.3. Modeling of the Pseudogap Phase

According to Norman *et al.*, "superconductivity is an instability of the normal state. Therefore, to understand the origin of superconductivity, one must understand the nature of the normal state from which it arises." [32] This turns out to be hard to accomplish for underdoped cuprates as their normal state is still not well-understood [23]. The two most likely underlying phenomena are pre-formed Cooper pairs and competing order [32]. On the one hand, Cooper pairs are thought to start forming below T^*, but that the onset of phase coherence which causes superconductivity only takes place below T_c. On the other hand, the superconducting order is presumed to be competing with another distinct, incompatible state — a *hidden order*, where the name comes from how difficult it is for ordinary probes to couple to them — over the electrons around the Fermi surface. The hidden order becoming more favorable than superconductivity as the doping decreases would be the cause of T_c going down as T^* goes up. Among the suggestions for such hidden order are the d-density wave state of Chakravarty [10] and the circulating current state of Varma [51]. Both proposals detail time-reversal symmetry breaking states generating a quantum critical phase distinct from the Fermi liquid phase for which a linear dependence of resistivity on temperature is a signature. Thus, both are consistent with experiments. Besides, additional signatures of quantum criticality have manifested through experiments, such as linearly dependent linewidths on both temperature and binding energy in photoemission spectra [32, and therein].

Competing order has been identified as a probable scenario in recent experiments, but preformed incoherent pairs is also a possibility according to other results [18, and therein].

1.4. Rationale of this Work

A clear and simple test is thus needed to compare the theoretical models of the cuprates with unambiguous experimental measurements. Experimental data on the electronic Berry phase has been available for some time, but it has not been used before to analyze theories of the cuprates. Hence, the objective of this work is to establish if one of the theoretical models is unfit for cuprates according to its Berry phase after comparing with experimental results. The model investigated here is the circulating current state of Varma [51] as approached by Bulut *et al.* [7], which presents a staggered pattern of intra-unit cell loop currents.

2. THE BERRY PHASE

By definition, the *Berry phase* — also known as the *geometric phase* — is the phase accumulated by a quantum state during an adiabatic process over the course of a cycle [46]. Although the phenomenon was discovered in the 1950s [26, 34], the concept was only generalized in 1984 in a publication by Sir Michael Berry [5]. His paper received much attention at the time and has stayed relevant since then because of its extensive and crucial implications, especially in the field of electron dynamics [54]. Notably, the Berry phase plays an integral part in the microscopic explanation of both spontaneous polarization in ferroelectric materials [38, 54] and spontaneous magnetization in ferromagnetic materials [47, 54]. Likewise, it is fundamental to the theory of topological materials along with the Chern number [1].

According to the Adiabatic Theorem, an instantaneous energy eigenstate will evolve into its corresponding smoothly connected later-time eigenstate if subjected to an adiabatic process [6, 20]. But how does the phase change with time? Berry showed in his paper that the phase evolution known as the geometric phase which is separate from the dynamical phase $e^{iEt/\hbar}$ or its generalization cannot be removed by any gauge transformation of the eigenstates, contradicting what was believed at the time. Besides, he showed that this phase could be physically meaningful in some cases and even measurable [5].

2.1. From the Adiabatic Theorem

Although Berry assumed the Adiabatic Theorem to derive the phase evolution in his original paper, we can instead obtain the geometric phase while proving the theorem, as it was done in appendix A. Only the result is reported here.

Consider a time-dependent Hamiltonian $H(t)$ with $t \in \mathbb{R}_{\geq 0}$ over the course of an adiabatic process and let $\{|n(t)\rangle\}$ be the orthonormal set of instantaneous energy eigenstates such that they satisfy

$$H(t)\,|n(t)\rangle = E_n(t)\,|n(t)\rangle\ , \tag{2.1}$$

where $E_n(t)$ is the energy corresponding to eigenstate $|n(t)\rangle$. We assume furthermore non-degenerate eigenstates.

Any state $|\Psi(t)\rangle$ which satisfy the time-evolution equation

$$\frac{d}{dt}|\Psi(t)\rangle = -\frac{i}{\hbar}H(t)|\Psi(t)\rangle \tag{2.2}$$

will then evolve in time according to

$$|\Psi(t)\rangle = \sum_n c_n(0)e^{i\theta_n(t)}e^{i\gamma_n(t)}|n(t)\rangle \ , \tag{2.3}$$

where the phase $e^{i\theta_n(t)}$ is the generalization of the dynamical phase, such that $c_n(0) \in \mathbb{C}$, $\theta_n(t) = -\frac{1}{\hbar}\int_0^t E_n(t')\,dt'$, and

$$\gamma_n(t) = i\int_0^t \langle n(t')|\frac{d}{dt'}|n(t')\rangle \ dt' \, . \tag{2.4}$$

While the dynamical phase is indeed a part of the total phase as expected, the less intuitive phase evolution given by the real function $\gamma_n(t)$ is what we refer to as the Berry phase.

2.2. Generalization to Parameter Space

For the most part, expressing the Hamiltonian as a function of a time-dependent parameter $\boldsymbol{R}(t) = \Big(R^1(t),\ R^2(t),\ \ldots,\ R^N(t)\Big) \in \mathbb{R}^N$ for smooth functions $R_i(t)$ and $N \in \mathbb{N}_{>0}$ gives essential insight on the Bery phase. In agreement with this, the notation is modified to make the Hamiltonian, the energy eigenvalues, and the energy eigenstates depend on the parameter $\boldsymbol{R}(t)$ instead of t. According to the chain rule,

$$\begin{aligned}
\gamma_n(t) &= i \int_0^t \langle n(\boldsymbol{R}(t'))| \frac{d}{dt'} |n(\boldsymbol{R}(t'))\rangle \ dt' \\
&= i \int_0^t \langle n(\boldsymbol{R}(t'))| \nabla |n(\boldsymbol{R}(t'))\rangle \cdot \frac{d\boldsymbol{R}}{dt'} \, dt' \\
&= i \int_C \langle n(\boldsymbol{R})| \nabla |n(\boldsymbol{R})\rangle \cdot d\boldsymbol{R} \\
&\equiv \int_C \boldsymbol{A}_n(\boldsymbol{R}) \cdot d\boldsymbol{R} \,,
\end{aligned} \tag{2.5}$$

where ∇ is the gradient with respect to $\boldsymbol{R}$ and where the path of integration C is the path taken of the adiabatic process from $\boldsymbol{R}(0)$ to $\boldsymbol{R}(t)$ in parameter space. We assume that the eigenvalues are non-degenerate along the path C. Additionally, we have introduced $\boldsymbol{A}_n(\boldsymbol{R}) = i \langle n(\boldsymbol{R})| \nabla |n(\boldsymbol{R})\rangle$, which is commonly known as the Berry vector potential.

Suppose we make a gauge transformation such that $|n(\boldsymbol{R})\rangle \to e^{i\delta(\boldsymbol{R})} |n(\boldsymbol{R})\rangle$ for some $\delta(\boldsymbol{R}) \in \mathbb{R}$, then

$$\begin{aligned}
\boldsymbol{A}_n(\boldsymbol{R}) &= i \langle n(\boldsymbol{R})| \nabla |n(\boldsymbol{R})\rangle \\
&\to i \left[e^{-i\delta(\boldsymbol{R})} \langle n(\boldsymbol{R})|\right] \nabla \left[e^{i\delta(\boldsymbol{R})} |n(\boldsymbol{R})\rangle\right] \\
&= i e^{-i\delta(\boldsymbol{R})} \langle n(\boldsymbol{R})| \left[e^{i\delta(\boldsymbol{R})} \nabla |n(\boldsymbol{R})\rangle + i e^{i\delta(\boldsymbol{R})} |n(\boldsymbol{R})\rangle \nabla\delta(\boldsymbol{R})\right] \\
&= i \langle n(\boldsymbol{R})| \nabla |n(\boldsymbol{R})\rangle - \nabla\delta(\boldsymbol{R}) \\
&= \boldsymbol{A}_n(\boldsymbol{R}) - \nabla\delta(\boldsymbol{R}) \,.
\end{aligned} \tag{2.6}$$

Thus, $\boldsymbol{A}_n(\boldsymbol{R})$ obtains an additional gradient term under a gauge transformation. As such, it is not gauge-invariant. In any case, one can easily see the similarities with a quantum particle in an electromagnetic field with the magnetic vector potential replaced by the Berry vector potential. Although not a physical quantity, the vector potential can be used in both cases to obtain gauge-invariant physical quantities.

Under the previous gauge transformation, the Berry phase becomes

$$\begin{aligned}\gamma_n(t) = \int_C \boldsymbol{A}_n(\boldsymbol{R}) \cdot d\boldsymbol{R} \to \int_C [\boldsymbol{A}_n(\boldsymbol{R}) - \nabla\delta(\boldsymbol{R})] \cdot d\boldsymbol{R} \\ = \gamma_n(t) - [\delta(\boldsymbol{R}(t)) - \delta(\boldsymbol{R}(0))] \,.\end{aligned} \tag{2.7}$$

As such, the Berry phase may not always be gauge-invariant, but it will be for $\boldsymbol{R}(t) = \boldsymbol{R}(0)$. This last condition is equivalent to having the path of integration C be a loop. Then, assuming that this condition holds, the notation can be modified to make the Berry phase depend on the path C instead of t. This notation has the advantage of explicitly stating the path taken in parameter space of the adiabatic process.

Furthermore, let's assume that $C \in \mathbb{R}^3$. Consequently, by Stokes' Theorem

$$\begin{aligned}\gamma_n(C) &= \oint_C \boldsymbol{A}_n(\boldsymbol{R}) \cdot d\boldsymbol{R} \\ &= \iint_S [\nabla \times \boldsymbol{A}_n(\boldsymbol{R})] \cdot d\boldsymbol{S} \\ &\equiv \iint_S \boldsymbol{B}_n(\boldsymbol{R}) \cdot d\boldsymbol{S} \,,\end{aligned} \tag{2.8}$$

where the surface of integration S is *any* smooth connected compact surface bounded by C. Additionally, we have now introduced $\boldsymbol{B}_n(\boldsymbol{R})$, commonly known as the Berry curvature. Moreover, it is now clear that the Berry phase *only* depends on the geometry of the path in parameter space and not on the specific parametrization of the path — which is why it also goes by the name of geometric phase.

Under the previous gauge transformation, the Berry curvature becomes

$$\begin{aligned}\boldsymbol{B}_n(\boldsymbol{R}) = \nabla \times \boldsymbol{A}_n(\boldsymbol{R}) \to \nabla \times [\boldsymbol{A}_n(\boldsymbol{R}) - \nabla\delta(\boldsymbol{R})] \\ = \boldsymbol{B}_n(\boldsymbol{R}) \,.\end{aligned} \tag{2.9}$$

Thus, the Berry curvature is gauge-invariant because the curl of a gradient is always equal to zero, which implies that the Berry phase must also be gauge-invariant. The similarities with electromagnetism continue when replacing the magnetic field by the Berry curvature.

2.3. The Berry Curvature

The Berry curvature is our most important tool to calculate the Berry phase. At the moment, it is expressed in a rather complicated way. A much simpler expression can be obtained by first noting that

$$\begin{aligned} \boldsymbol{B}_n(\boldsymbol{R}) &= \nabla \times \boldsymbol{A}_n(\boldsymbol{R}) \\ &= \nabla \times i \left\langle n(\boldsymbol{R}) \right| \nabla \left| n(\boldsymbol{R}) \right\rangle \\ &= i \hat{\boldsymbol{e}}^i \varepsilon^{ijk} \partial^j \left[\left\langle n(\boldsymbol{R}) \right| \partial^k \left| n(\boldsymbol{R}) \right\rangle \right] , \end{aligned} \tag{2.10}$$

where ε^{ijk} is the Levi-Civita symbol, $\hat{\boldsymbol{e}}_i$ is the unit vector along the i^{th} axis in parameter space, and $\partial^i \equiv \frac{\partial}{\partial R^i}$. Then, by the product rule and as $\partial^j \partial^k = \partial^k \partial^j$,

$$\begin{aligned} \boldsymbol{B}_n(\boldsymbol{R}) &= i \hat{\boldsymbol{e}}^i \varepsilon^{ijk} \left\{ \left[\partial^j \left\langle n(\boldsymbol{R}) \right| \right] \left[\partial^k \left| n(\boldsymbol{R}) \right\rangle \right] + \left\langle n(\boldsymbol{R}) \right| \partial^j \partial^k \left| n(\boldsymbol{R}) \right\rangle \right\} \\ &= i \hat{\boldsymbol{e}}^i \varepsilon^{ijk} \left[\partial^j \left\langle n(\boldsymbol{R}) \right| \right] \left[\partial^k \left| n(\boldsymbol{R}) \right\rangle \right] . \end{aligned} \tag{2.11}$$

Moreover, inserting the complete basis of energy eigenstates leads to

$$\begin{aligned} \boldsymbol{B}_n(\boldsymbol{R}) &= i \hat{\boldsymbol{e}}^i \varepsilon^{ijk} \sum_m \left[\partial^j \left\langle n(\boldsymbol{R}) \right| \right] \left| m(\boldsymbol{R}) \right\rangle \left\langle m(\boldsymbol{R}) \right| \left[\partial^k \left| n(\boldsymbol{R}) \right\rangle \right] \\ &= i \hat{\boldsymbol{e}}^i \varepsilon^{ijk} \sum_{m \neq n} \left\{ \left\langle m(\boldsymbol{R}) \right| \left[\partial^j \left| n(\boldsymbol{R}) \right\rangle \right] \right\}^* \left\langle m(\boldsymbol{R}) \right| \left[\partial^k \left| n(\boldsymbol{R}) \right\rangle \right] , \end{aligned} \tag{2.12}$$

where the last step is a consequence of the generalization of (A.9). Finally, by going back to vector notation and using the generalization of (A.11):

$$\begin{aligned} \boldsymbol{B}_n(\boldsymbol{R}) &= i \sum_{m \neq n} \left[\left\langle m(\boldsymbol{R}) \right| \nabla \left| n(\boldsymbol{R}) \right\rangle \right]^* \times \left\langle m(\boldsymbol{R}) \right| \nabla \left| n(\boldsymbol{R}) \right\rangle \\ &= i \sum_{m \neq n} \frac{\left\langle n(\boldsymbol{R}) \right| \left[\nabla H(\boldsymbol{R}) \right] \left| m(\boldsymbol{R}) \right\rangle \times \left\langle m(\boldsymbol{R}) \right| \left[\nabla H(\boldsymbol{R}) \right] \left| n(\boldsymbol{R}) \right\rangle}{\left[E_n(\boldsymbol{R}) - E_m(\boldsymbol{R}) \right]^2} , \end{aligned} \tag{2.13}$$

where the hermicity of $\nabla H(\boldsymbol{R})$ is a consequence of the hermicity of $H(\boldsymbol{R})$. This last equation makes it explicit that the Berry curvature is gauge-invariant. Besides, it can be inferred from those results that

$$\sum_n \boldsymbol{B}_n(\boldsymbol{R}) = 0 , \tag{2.14}$$

because of the anticommutativity of the cross product: for any $\boldsymbol{a}, \boldsymbol{b} \in \mathbb{R}^3$, $\boldsymbol{a} \times \boldsymbol{b} + \boldsymbol{b} \times \boldsymbol{a} = 0$. As a result, for any path C

$$\sum_n \gamma_n(C) = 0\,. \tag{2.15}$$

Soon after Berry's demonstration came experiments that would confirm his results [40, Section 5.6] and prove the Berry phase to be a valid measurable quantity. Resta captures perfectly well the importance of this fact: "[the] main message of Berry's milestone paper can be spelled out by saying that there are also observable effects of a completely different nature: the [Berry] phase *cannot* be expressed in terms of the eigenvalues of any operators, whereas it is by definition a gauge-invariant phase of the state vector [38]."

Before long, it was suggested that the Berry phase could have some connection with the motion of electrons in a crystal lattice since the Brillouin zone is a parameter space with different eigenstates defined at every point [55]. Indeed, an electron's quantum state can technically acquire a non-trivial Berry phase as it loops in the Brillouin zone due to an external perturbation. Accordingly, a slow dynamical variable needs to be used as a parameter [54].

2.4. Linear Two-Level Systems

A clear consequence of (2.8) and (2.13) is that degeneracy points have particular importance in the Berry phase even if they are not near the path taken in parameter space.

A two-level Hamiltonian linear in the parameter $\boldsymbol{R} \in \mathbb{R}^3$ is a perfect example of such a situation. For simplicity, the Hamiltonian is normalized by some unitary dimensionful constant in order to share units with $\boldsymbol{R}$.

Recall that the set $\{\boldsymbol{I}, \boldsymbol{\sigma}^1, \boldsymbol{\sigma}^2, \boldsymbol{\sigma}^3\}$ where $\boldsymbol{\sigma}_i$ are the Pauli matrices forms a basis for the vector space of 2×2 Hermitian matrices. Thus, this Hamiltonian can be written after an appropriate coordinate transformation as

$$\boldsymbol{H}(\boldsymbol{R}) = R^0 \boldsymbol{I} + R^1 \boldsymbol{\sigma}^1 + R^2 \boldsymbol{\sigma}^2 + R^3 \boldsymbol{\sigma}^3 \,, \tag{2.16}$$

for some $R^0 \in \mathbb{R}$. Then, the energy eigenvalues are simply

$$E_\pm(\boldsymbol{R}) = \pm\sqrt{[R^1]^2 + [R^2]^2 + [R^3]^2} = \pm\,|\boldsymbol{R}| \,, \tag{2.17}$$

with corresponding energy eigenstates $|\pm(\boldsymbol{R})\rangle$. Furthermore, note that the sole point of degeneracy is at the origin.

We want to evaluate the Berry phase $\gamma_+(C)$ of the eigenstate $|+(\boldsymbol{R})\rangle$ as $\boldsymbol{R}$ is driven around a loop C in parameter space. In particular, it is essential that $\boldsymbol{0} \notin C$ because of the eigenstates being degenerate at $\boldsymbol{R} = \boldsymbol{0}$ and since $\boldsymbol{0} \in C$ would contradict the assumption that the eigenvalues are non-degenerate along C.

We start by deriving the Berry curvature $\boldsymbol{B}_+(\boldsymbol{R})$. It can be accomplished by taking the curl of the Berry vector potential $\boldsymbol{A}_+(\boldsymbol{R}) = i\,\langle +(\boldsymbol{R})|\,\nabla\,|+(\boldsymbol{R})\rangle$; however, this method involves many steps. Instead, we will make use of (2.13): it only requires to know that both $\nabla H(\boldsymbol{R}) = \Big(\boldsymbol{\sigma}^1,\ \boldsymbol{\sigma}^2,\ \boldsymbol{\sigma}^3\Big) \equiv \boldsymbol{\sigma}$ and $E_+(\boldsymbol{R}) - E_-(\boldsymbol{R}) = 2\,|\boldsymbol{R}|$ for all $\boldsymbol{R}$. Hence, we obtain

$$\boldsymbol{B}_+(\boldsymbol{R}) = i\frac{\langle +(\boldsymbol{R})|\,\boldsymbol{\sigma}\,|-(\boldsymbol{R})\rangle \times \langle -(\boldsymbol{R})|\,\boldsymbol{\sigma}\,|+(\boldsymbol{R})\rangle}{4\,|\boldsymbol{R}|^2} \,. \tag{2.18}$$

We do not have an explicit expression for $|+(\boldsymbol{R})\rangle$ nor $|-(\boldsymbol{R})\rangle$. To approach this part of the problem, fix $\boldsymbol{R}$ and rotate the coordinate system such that $\hat{\boldsymbol{R}} \to \hat{\boldsymbol{z}}$. In this new coordinate system, $|+(\boldsymbol{R})\rangle$ and $|-(\boldsymbol{R})\rangle$ are the eigenstates of $\boldsymbol{\sigma}^3$ and the Berry curvature

equals to

$$\begin{aligned}\boldsymbol{B}_+(\boldsymbol{R}) &= i\frac{[\hat{\boldsymbol{x}} - i\hat{\boldsymbol{y}}] \times [\hat{\boldsymbol{x}} + i\hat{\boldsymbol{y}}]}{4\,|\boldsymbol{R}|^2} \\ &= -\frac{1}{2}\frac{\hat{\boldsymbol{z}}}{|\boldsymbol{R}|^2} \\ &\to -\frac{1}{2}\frac{\hat{\boldsymbol{R}}}{|\boldsymbol{R}|^2}\,,\end{aligned} \tag{2.19}$$

where we have rotated back to the original coordinate system in the last step by taking $\hat{\boldsymbol{z}} \to \hat{\boldsymbol{R}}$. Additionally, note that $\boldsymbol{B}_-(\boldsymbol{R}) = -\boldsymbol{B}_+(\boldsymbol{R})$ according to (2.14). Once again we note the similarities with electromagnetism: as the divergence of $\boldsymbol{B}_\pm(\boldsymbol{R})$ vanishes at every point except for the origin, or explicitly

$$\begin{aligned}\nabla \cdot \boldsymbol{B}_\pm(\boldsymbol{R}) &= \nabla \cdot \left[\mp\frac{1}{2}\frac{\hat{\boldsymbol{R}}}{|\boldsymbol{R}|^2}\right] \\ &= \mp 2\pi\delta^3(\boldsymbol{R})\,,\end{aligned} \tag{2.20}$$

the degeneracy must generate a field identical to one from an electric or magnetic monopole of charge of magnitude $\frac{1}{2}$. This property was expected from the beginning because the Berry curvature is defined as the curl of the Berry potential and the divergence of a curl is everywhere zero except at singular points. Therefore, the property that points of degeneracy act as monopoles for the Berry curvature and that fields may only originate from them holds for any Hamiltonian.

To conclude, the Berry phase is evaluated to be

$$\begin{aligned}\gamma_\pm(C) &= \iint_S \boldsymbol{B}_\pm(\boldsymbol{R}) \cdot d\boldsymbol{S} \\ &= \mp\frac{1}{2}\iint_S \frac{\hat{\boldsymbol{R}} \cdot d\boldsymbol{S}}{|\boldsymbol{R}|^2} \\ &\equiv \mp\tfrac{1}{2}\Omega(C)\,,\end{aligned} \tag{2.21}$$

where S can be any smooth connected compact surface bounded by C as seen before and $\Omega(C)$ is the solid angle subtended by C relative to the origin. This is a beautiful result which demonstrates the geometric nature of the Berry phase.

2.4.1. Special Case: 2D

An important special case to consider is when the parameter space is two-dimensional. In this case, $\Omega(C)$ is equal to $2\pi n$ where n is the winding number of C around the point of degeneracy. In particular, it means that it equals 0 when C does not surround the point of degeneracy. To get some intuition behind this, fix a plane in $\mathbb{R}^3$ and a closed curve on the plane. Then, the solid angle subtended by the curve relative to a point arbitrarily close to the plane either approaches zero or half of the total solid angle of a sphere, leading to a Berry phase

$$\gamma_{\pm}(C) = \mp\pi n\,. \tag{2.22}$$

A rigorous mathematical proof of this will be given using precisely this method in the next subsection. A real-life example of this result can be found in monolayer graphene where a Berry phase of π has been confirmed experimentally [56].

2.5. Generalized Two-Level Systems in 2D

It is crucial to remember that only two-level Hamiltonians *linear* in the parameter $\boldsymbol{R}$ as been considered so far. Dropping this assumption, the Hamiltonian can be written as

$$\boldsymbol{H}(\boldsymbol{R}) = Q^0(\boldsymbol{R})\boldsymbol{I} + Q^1(\boldsymbol{R})\boldsymbol{\sigma}^1 + Q^2(\boldsymbol{R})\boldsymbol{\sigma}^2 + Q^3(\boldsymbol{R})\boldsymbol{\sigma}^3\,, \tag{2.23}$$

for smooth real functions $Q^i(\boldsymbol{R})$ having the same units as $\boldsymbol{R}$. In particular, the vector $\boldsymbol{Q}(\boldsymbol{R}) = \Big(Q^1(\boldsymbol{R}),\ Q^2(\boldsymbol{R}),\ Q^3(\boldsymbol{R})\Big) \in \mathbb{R}^3$ can be viewed as a parameter in a *different* parameter space. In such a way, we can define D as the path taken of the adiabatic process from $\boldsymbol{Q}(\boldsymbol{R}(0))$ to $\boldsymbol{Q}(\boldsymbol{R}(t))$ in this parameter space. In other words, D is the image of the path C under $\boldsymbol{Q}$. And since the Hamiltonian evolves in the same way through time if it follows path C in the original parameter space or path D in the new parameter space, their Berry phase has to be the same. Hence, we must have that

$$\gamma_\pm(C) = \mp\tfrac{1}{2}\Omega(D)\,. \tag{2.24}$$

We will only consider the case where both parameter spaces $\boldsymbol{R}$ and $\boldsymbol{Q}(\boldsymbol{R})$ are two-dimensional surfaces with a unique point of degeneracy approached linearly with $\boldsymbol{R}$ in the parameter space $\boldsymbol{Q}(\boldsymbol{R})$. Without loss of generality, let the point of degeneracy be at the origin of the parameter space and $R^1 = 0$. Consequently, $\boldsymbol{Q}(\boldsymbol{R})$ must be a smooth connected surface passing through the origin since $\boldsymbol{R}$ varies in two-dimensional parameter space. We start by parameterizing the parameter space as $\boldsymbol{R}(r,\theta)$ where $r = |\boldsymbol{R}|$ and $\theta = \operatorname{atan2}(R^3, R^2)$. Thus, $\boldsymbol{Q}(r,\theta) \equiv \boldsymbol{Q}(\boldsymbol{R}(r,\theta))$ is a parametrization of the surface spanned by $\boldsymbol{Q}(\boldsymbol{R})$ with θ periodic with period 2π. Therefore,

$$\begin{aligned}\Omega(D) &= \iint_T \frac{\hat{\boldsymbol{Q}}\cdot d\boldsymbol{S}}{|\boldsymbol{Q}|^2} \\ &= \iint_S \frac{\boldsymbol{Q}(r,\theta)}{|\boldsymbol{Q}(r,\theta)|^3}\cdot\left[\frac{\partial\boldsymbol{Q}}{\partial r}\times\frac{\partial\boldsymbol{Q}}{\partial\theta}\right] dr\,d\theta\,,\end{aligned} \tag{2.25}$$

where T can be any smooth connected compact surface bounded by D and where we have defined $S \equiv \{(r,\theta) \in \mathbb{R}_{\geq 0}\times[0,2\pi)\,|\,\boldsymbol{Q}(r,\theta)\in T\}$. Although T is not uniquely defined, the surface S is.

Let Π be the tangent plane to the surface $\boldsymbol{Q}(\boldsymbol{R})$ at the origin and let $\hat{\boldsymbol{n}}$ be the unit normal vector of this plane. Because $\boldsymbol{Q}(r,\theta)$ is a smooth connected surface in $2D$, it can be expressed as

$$\boldsymbol{Q}(r,\theta) = r\boldsymbol{\Theta}(\theta) + \boldsymbol{V}(r,\theta)\,, \tag{2.26}$$

for some vectors $\boldsymbol{\Theta}(\theta), \boldsymbol{V}(r,\theta) \in \Pi$ for all (r,θ) such that $\boldsymbol{\Theta}(\theta) \neq \boldsymbol{0}$ and $\boldsymbol{V}(r,\theta) = \mathcal{O}(r^2)$, both periodic in θ with period 2π. Assume that the surface with $\boldsymbol{V}(r,\theta) = 0$ for all (r,θ) denoted as the *linear surface* has no singular point. As a result, $\boldsymbol{\Theta}(\theta) \times \boldsymbol{\Theta}'(\theta) \equiv g(\theta)\hat{\boldsymbol{n}}$ for some smooth real function $g(\theta)$ which is either strictly positive or strictly negative. This condition is equivalent to having the gap amplitude proportional to $\mathcal{O}(r)$ in every direction.

We begin by translating the surface $\boldsymbol{Q}(\boldsymbol{R})$ by $\xi\hat{\boldsymbol{n}}$ for some $\xi > 0$ known as the *mass term* although it carries units of $\boldsymbol{R}$. It has the effect of shifting the point relative to which we evaluate the solid angle. We will later take the limit $\xi \to 0$. As such,

$$\boldsymbol{Q}(r,\theta) \to \boldsymbol{Q}_\xi(r,\theta) \equiv r\boldsymbol{\Theta}(\theta) + \boldsymbol{V}(r,\theta) + \xi\hat{\boldsymbol{n}}\,. \tag{2.27}$$

The vector $\boldsymbol{Q}_\xi(r,\theta)$ has a squared length of

$$\begin{aligned} |\boldsymbol{Q}_\xi(r,\theta)|^2 &= |r\boldsymbol{\Theta}(\theta)|^2 + 2r\boldsymbol{\Theta}(\theta)\cdot\boldsymbol{V}(r,\theta) + |\boldsymbol{V}(r,\theta)|^2 + \xi^2 \\ &\equiv |r\boldsymbol{\Theta}(\theta)|^2\,[1 + v(r,\theta)] + \xi^2\,, \end{aligned} \tag{2.28}$$

where $v(r,\theta) = \mathcal{O}(r)$ includes all terms responsible for the difference in the length of the vector $\boldsymbol{Q}(r,\theta)$ from the linear case. Furthermore, the normal vector of the parametric surface $\boldsymbol{Q}_\xi(r,\theta)$ at any point (r,θ) is

$$\begin{aligned} \frac{\partial\boldsymbol{Q}_\xi}{\partial r} \times \frac{\partial\boldsymbol{Q}_\xi}{\partial\theta} &= \frac{\partial\boldsymbol{Q}}{\partial r} \times \frac{\partial\boldsymbol{Q}}{\partial\theta} \\ &= \left[\boldsymbol{\Theta}(\theta) + \frac{\partial\boldsymbol{V}}{\partial r}\right] \times \left[r\boldsymbol{\Theta}'(\theta) + \frac{\partial\boldsymbol{V}}{\partial\theta}\right] \\ &= r\boldsymbol{\Theta}(\theta) \times \boldsymbol{\Theta}'(\theta) + \boldsymbol{\Theta}(\theta) \times \frac{\partial\boldsymbol{V}}{\partial\theta} + r\frac{\partial\boldsymbol{V}}{\partial r} \times \boldsymbol{\Theta}'(\theta) + \frac{\partial\boldsymbol{V}}{\partial r} \times \frac{\partial\boldsymbol{V}}{\partial\theta} \\ &\equiv rg(\theta)\,[1 + w(r,\theta)]\,\hat{\boldsymbol{n}}\,. \end{aligned} \tag{2.29}$$

where $w(r,\theta) = \mathcal{O}(r)$ includes all terms responsible for the difference in the surface area between the tangent plane at (r,θ) and the linear surface at the same point.

Combining all results into (2.25) yields

$$\begin{aligned}
\Omega(D) &= \lim_{\xi\to 0}\iint\limits_{S} \frac{\xi r g(\theta)[1+w(r,\theta)]}{\left\{|r\boldsymbol{\Theta}(\theta)|^2\,[1+v(r,\theta)]+\xi^2\right\}^{\frac{3}{2}}}\,dr\,d\theta \\
&\equiv \lim_{\xi\to 0}\iint\limits_{S} \frac{\xi r g(\theta)[1+w(r,\theta)]}{\left[|r\boldsymbol{\Theta}(\theta)|^2+\xi^2\right]^{\frac{3}{2}}}\,dr\,d\theta + \tilde{\Omega}(D) \\
&= \lim_{\xi\to 0}\iint\limits_{S} \frac{g(\theta)}{|\boldsymbol{\Theta}(\theta)|^2}\frac{[r/\xi]\,|\boldsymbol{\Theta}(\theta)|^{-1}\,[1+w(r,\theta)]}{\left\{[r/\xi]^2+|\boldsymbol{\Theta}(\theta)|^{-2}\right\}^{\frac{3}{2}}}\,d[r/\xi]\,d\theta + \tilde{\Omega}(D) \\
&\equiv \lim_{\xi\to 0}\iint\limits_{S} \frac{g(\theta)}{|\boldsymbol{\Theta}(\theta)|^2} f(r/\xi,\theta)\,d[r/\xi]\,d\theta + \tilde{\Omega}(D) \\
&= 2\pi\bar{g}n + \tilde{\Omega}(D)\,,
\end{aligned} \tag{2.30}$$

where n is the winding number, and

$$\bar{g} = \frac{1}{2\pi}\int_0^{2\pi} \frac{g(\theta)}{|\boldsymbol{\Theta}(\theta)|^2}\,d\theta\,, \tag{2.31a}$$

$$f(r/\xi,\theta) = \frac{[r/\xi]\,|\boldsymbol{\Theta}(\theta)|^{-1}}{\left\{[r/\xi]^2+|\boldsymbol{\Theta}(\theta)|^{-2}\right\}^{\frac{3}{2}}}[1+w(r,\theta)]\,, \tag{2.31b}$$

$$\tilde{\Omega}(D) = \lim_{\xi\to 0}\iint\limits_{S} \frac{g(\theta)}{|\boldsymbol{\Theta}(\theta)|^2}\left[\left\{1+\frac{|r\boldsymbol{\Theta}(\theta)|^2\,v(r,\theta)}{|r\boldsymbol{\Theta}(\theta)|^2+\xi^2}\right\}^{-\frac{3}{2}}-1\right] f(r/\xi,\theta)\,d[r/\xi]\,d\theta\,. \tag{2.31c}$$

The last step of (2.30) can be understood very simply by making a change of variable. For any range of integration $[r_i, r_f]$ in r where $0 \le r_i \le r_f$ and fixed θ, we must obtain for any $k \in \mathbb{N}^0$ that

$$\int_{r_i}^{r_f} \frac{r^k[r/\xi]\,|\boldsymbol{\Theta}(\theta)|^{-1}}{\left\{[r/\xi]^2+|\boldsymbol{\Theta}(\theta)|^{-2}\right\}^{\frac{3}{2}}}\,d[r/\xi] = \xi^k\int_{r_i/\xi}^{r_f/\xi} \frac{r^{k+1}\,|\boldsymbol{\Theta}(\theta)|^{-1}}{\left\{r^2+|\boldsymbol{\Theta}(\theta)|^{-2}\right\}^{\frac{3}{2}}}\,dr\,. \tag{2.32}$$

Any non-zero limit of integration will go to infinity when $\xi \to 0$ while a zero limit of integration will stay zero. Hence, after taking $\xi \to 0$ the integral in (2.32) will equal zero unless $k = 0$ and $0 = r_i < r_f$ where it will converge to 1. Therefore, fixing θ and evaluating the integral over r in (2.30) will follow this rule and give the appropriate result since we have in the expression of $f(r/\xi)$ that $w(r,\theta) = \mathcal{O}(r)$.

Notice that we have not made any approximation in the calculation so far. In such a way, an explicit and exact expression for the solid angle has been obtained up to a correction

term $\tilde{\Omega}(D)$ which equals to the difference with the solid angle calculated from the linear surface. However, there should be no correction since the surface $\boldsymbol{Q}(r,\theta)$ lies on the linear surface itself. Thus, it must be the case that $\tilde{\Omega}(D)=0$. A rigorous proof of this proposition is given in appendix C. Consequently, (2.30) becomes

$$\Omega(D) = 2\pi\bar{g}n\,. \tag{2.33}$$

It is important to note that (2.33) is *exact* for $\boldsymbol{Q}(r,\theta)$ as described initially. No approximation has been made to obtain this result. According to (2.24), the Berry phase in this case must be

$$\gamma_{\pm}(C) = \mp\pi\bar{g}n\,. \tag{2.34}$$

2.5.1. Special Case: Simple Dirac Point

An important special case under the conditions found in this section is when $\boldsymbol{\Theta}(\theta)$ allows a simple Dirac point at the origin. Let $\boldsymbol{\Theta}(\theta) = \Big(0,\ \hat{\boldsymbol{r}}\cdot\boldsymbol{v}_2,\ \hat{\boldsymbol{r}}\cdot\boldsymbol{v}_3\Big)$ for $\hat{\boldsymbol{r}} = \Big(\cos\theta,\ \sin\theta\Big)$ and for $\boldsymbol{v}_2,\boldsymbol{v}_3\in\mathbb{R}^2$ some constant vectors satisfying $|\boldsymbol{v}_2\times\boldsymbol{v}_3|\neq 0$. There is no singular point if and only if $|\boldsymbol{v}_2\times\boldsymbol{v}_3|\neq 0$. Hence, let $\sigma\in\{\pm 1\}$ be such that $\boldsymbol{v}_2\times\boldsymbol{v}_3 = \sigma|\boldsymbol{v}_2\times\boldsymbol{v}_3|\hat{\boldsymbol{z}}$. In this case, it is obtained after some simplification that

$$\bar{g} = \sigma\frac{|\boldsymbol{v}_2\times\boldsymbol{v}_3|}{2\pi}\int_0^{2\pi}\frac{d\theta}{[\hat{\boldsymbol{r}}\cdot\boldsymbol{v}_2]^2+[\hat{\boldsymbol{r}}\cdot\boldsymbol{v}_3]^2}\,. \tag{2.35}$$

The easiest way to solve this integral is to define the complex variable $z(\theta) = \hat{\boldsymbol{r}}\cdot[\boldsymbol{v}_2 + i\boldsymbol{v}_3]$. It satisfies $|z|^2 = [\hat{\boldsymbol{r}}\cdot\boldsymbol{v}_2]^2+[\hat{\boldsymbol{r}}\cdot\boldsymbol{v}_3]^2$ and $z^*z' = |z||z|' + i|\boldsymbol{v}_2\times\boldsymbol{v}_3|$. Thus, in terms of z

$$\begin{aligned}\bar{g} &= \sigma\frac{|\boldsymbol{v}_2\times\boldsymbol{v}_3|}{2\pi}\oint\frac{1}{|z|^2}\cdot\frac{dz}{z'}\\ &= \sigma\,.\end{aligned} \tag{2.36}$$

according to Cauchy's integral formula. Therefore, the Berry phase equals

$$\gamma_{\pm}(C) = \mp\sigma\pi n\,. \tag{2.37}$$

2.6. Avoided Band Crossings

This analysis of two-level systems shows how a non-zero Berry phase can arise from avoided band crossings: the space spanned by $\boldsymbol{Q}(\boldsymbol{R}) \in \mathbb{R}^3$ should not include the origin. The electrons orbiting in parameter space can still acquire a Berry phase because the solid angle does not necessarily have to equal zero. As an example, take the Hamiltonian

$$\boldsymbol{H}(\boldsymbol{R}) = \xi\boldsymbol{\sigma}^1 + R^2\boldsymbol{\sigma}^2 + R^3\boldsymbol{\sigma}^3\,, \tag{2.38}$$

for small mass $\xi > 0$. It is equivalent to $\boldsymbol{Q}_\xi(\boldsymbol{R})$ as defined earlier with $\boldsymbol{\Theta}(\theta) = \Big(0,\ \cos\theta,\ \sin\theta\Big)$ and $\boldsymbol{V}(r,\theta) = \boldsymbol{0}$. For simplicity, let the surface of integration S to be the disk centered at the origin with radius ρ. Following the derivation of (2.30), the Berry phase is then

$$\gamma_\pm(C) = \mp\pi\left[1 - \frac{1}{\sqrt{[\rho/\xi]^2 + 1}}\right]. \tag{2.39}$$

By a simple change of coordinates $R^2 \to aR^2$ and $R^3 \to bR^3$ for some $a, b \in \mathbb{R} \setminus \{0\}$, the same equation (2.39) holds when one takes the surface of integration S to be the ellipse centered at the origin with the semi-axes of length $a\rho$ and $b\rho$ in the R^2-direction and in the R^3-direction respectively. In these simple cases, the dispersion has the form of a parabolic avoided crossing. More generally, the different types of parabolic avoided crossings in two-dimensional systems are classified by their *Diracness*, which determines the degree to which the Hamiltonian has Dirac-like features [17].

3. QUANTUM OSCILLATIONS

Quantum oscillations are oscillatory variations detected in most measurable quantities when changing the magnetic field strength [12]. This effect was first discovered experimentally in 1930 in magnetization by Wander Johannes de Haas and Pieter M. van Alphen — called the de Hass–van Alphen effect — and in magnetoresistance by Lev W. Shubnikov and de Haas [36] — called the Shubnikov–de Haas effect. It was only twenty years later that Lars Onsager showed that it could be used to map a metal's Fermi surface [33]. Since then, quantum oscillations have been a powerful tool to determine with high precision and along any direction the Fermi surface's extremal cross-sectional areas [44].

Similar to the physics of Landau quantization of electrons, that of quantum oscillations is described from a semi-classical perspective. To obtain some insight on the subject, it is valuable to recall the Landau quantization problem [22, Chapters 110–111]. First, consider a free electron in a constant uniform magnetic field $\boldsymbol{B}$. As the spin part of the Hamiltonian commutes with the other parts, the spin of the electron has no impact on the dispersion relation. The electronic dispersion relation for band $n \in \mathbb{N}$ under the Landau gauge is then

$$\varepsilon_n(p_y, p_z) = \frac{\hbar e|\boldsymbol{B}|}{m_e}\left[n + \frac{1}{2}\right] + \frac{p_z^2}{2m_e}\,. \tag{3.1}$$

Note that the energy being degenerate in p_y is not physical but instead comes from a choice. Still, the fact that it is degenerate in exactly one momentum coordinate is physical and is the cause of degeneracies in Landau levels. At a fixed energy ε, it gives

$$n = \frac{m_e}{\hbar e}\left[\varepsilon - \frac{p_z^2}{2m_e}\right] \cdot |\boldsymbol{B}|^{-1} - \frac{1}{2}\,. \tag{3.2}$$

We thus expect the energy levels to pass through a fixed energy with a period proportional to $|\boldsymbol{B}|^{-1}$. Although very simple, this derivation outlines the essential physics of quantum oscillations.

3.1. Semiclassical Electron Dynamics

We first lay out the fundamentals of semiclassical electron dynamics in a crystal lattice as formulated by Kittel and McEuen [21]. Assume a Bloch electron wave packet such that

the position uncertainty is much larger than the lattice spacing and at the same time much smaller than the scale on which considerable changes occur in external fields [16]. In this way, the single momentum plane wave analysis is valid while the effect of external fields is particle-like on the electron. Additionally, assume that we can neglect interband transitions. Let the average position of the wave-packet be denoted by $\boldsymbol{x}$ and the average *canonical* crystal momentum by $\hbar\boldsymbol{q}$. Suppose furthermore that the electron is in a constant uniform magnetic field $\boldsymbol{B}$. The *kinetic* crystal momentum is then $\hbar\boldsymbol{k} = \hbar\boldsymbol{q} + e\boldsymbol{A}$ where $\boldsymbol{A}$ is the magnetic vector potential. The equations of motion are

$$\dot{\boldsymbol{x}} = \tfrac{1}{\hbar}\nabla\varepsilon_n(\boldsymbol{k})\,, \tag{3.3a}$$

$$\hbar\dot{\boldsymbol{k}} = -e[\dot{\boldsymbol{x}} \times \boldsymbol{B}]\,, \tag{3.3b}$$

where ∇ is the gradient with respect to $\boldsymbol{k}$ and $\varepsilon_n(\boldsymbol{k})$ is the dispersion relation of band n at $\boldsymbol{k}$. Combining both equations leads to $\dot{\boldsymbol{k}} \propto -[\nabla\varepsilon_n(\boldsymbol{k}) \times \boldsymbol{B}]$, meaning that $\dot{\boldsymbol{k}} \perp \nabla\varepsilon_n(\boldsymbol{k})$ and $\dot{\boldsymbol{k}} \perp \boldsymbol{B}$. Because $\nabla\varepsilon_n(\boldsymbol{k})$ is perpendicular to the Fermi surface for an electron at the Fermi energy, $\boldsymbol{k}$ must lie in a plane parallel to the Fermi surface. Moreover, the component of $\boldsymbol{k}$ parallel to $\boldsymbol{B}$ must be constant. Thus, an electron at the Fermi energy will go around the Fermi surface in a plane perpendicular to the magnetic field.

The momentum-space orbit and the projection perpendicular to $\boldsymbol{B}$ of the position-space orbit can be related with one another through (3.3b). The first thing to notice is that for any vectors $\boldsymbol{a}, \boldsymbol{b}, \boldsymbol{c}$ where $\boldsymbol{c}$ is a unit vector and such that $\boldsymbol{a} = \boldsymbol{b} \times \boldsymbol{c}$, we have $\boldsymbol{b}_\perp = \boldsymbol{c} \times \boldsymbol{a}$ where $\boldsymbol{b}_\perp$ is the perpendicular part of $\boldsymbol{b}$ with respect to $\boldsymbol{c}$. Consequently,

$$\dot{\boldsymbol{x}}_\perp = -\frac{\hbar}{e|\boldsymbol{B}|}\hat{\boldsymbol{B}} \times \dot{\boldsymbol{k}}\,. \tag{3.4}$$

Recall that $\boldsymbol{B}$ remains constant in time. After integrating (3.4) with respect to time,

$$\boldsymbol{x}_\perp(t) - \boldsymbol{x}_\perp(0) = -\frac{\hbar}{e|\boldsymbol{B}|}\hat{\boldsymbol{B}} \times [\boldsymbol{k}(t) - \boldsymbol{k}(0)]\,. \tag{3.5}$$

Accordingly, the orbits are related with one another through a $\pi/2$–rotation and a scale factor of $l_B^2 \equiv \hbar/[e|\boldsymbol{B}|]$, which is the squared magnetic length. This relation is represented in figure 3.1.

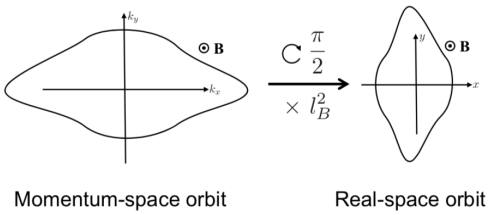

Figure 3.1: Orbit in momentum space under an external magnetic field $\boldsymbol{B}$ and its projection perpendicular to the field in position space obtained through rotating by $\pi/2$ and scaling by l_B^2. The field points out of the plane in both cases. Reproduced from [29].

3.2. Semiclassical Orbit Quantization

The Bohr-Sommerfeld quantization rule is normally the starting point of semiclassical orbit quantization [35]. Formulated before the development of modern quantum mechanics, it gives the spectrum of allowed semiclassical states through the quantization condition

$$\oint p\, dx = h \left[n + \frac{1}{2} \right] , \tag{3.6}$$

where the $\frac{1}{2}$–shift comes from the Maslov contribution, or in other words the number of caustics on the orbit integrated over. The JWKB approximation can be used to derive this by matching the phases of the wave functions near the classical turning points [22, Chapter 48] — but it is not the only way to attain this result. In 1966, the same result was obtained through a different method relating to semiclassical electron dynamics [39]. On top of leading to an analysis to higher order in the magnetic field, it showed that the right-hand side of (3.6) depends more generally on the electron orbit. It was shown many years later that the Berry phase along the momentum-space orbit takes part in the generalization of the quantization condition [30].

There is an intuitive, physical interpretation given by Fuchs [16, appendix A] to explain this generalization. In essence, the quantization condition emerges from periodicity as the particle's phase difference over a position-space orbit C must be a multiple of $2\pi\hbar$. Then, the zeroth order contribution in $\hbar$ to the phase is $\oint_C \boldsymbol{p} \cdot d\boldsymbol{x}$ as the linear momentum $\boldsymbol{p}$ is the variable conjugate to $\boldsymbol{x}$. It is thus a valid assumption to take $\boldsymbol{p} = \hbar \boldsymbol{q}$ [16]. In turn, the next contributions to the phase are to first order in $\hbar$ and consist of the momentum-space Berry phase and of the Maslov contribution.

Combining all the contributions with the quantization condition and rearranging the terms leads to

$$\frac{1}{2\pi}\oint_C \boldsymbol{q}\cdot d\boldsymbol{x} = n - \Gamma_n(\bar{C}) + \frac{1}{2}\,, \tag{3.7}$$

such that $\Gamma_n(\bar{C}) \equiv \gamma_n(\bar{C})/[2\pi]$ for $\gamma_n(\bar{C})$ the Berry phase of state $n \in \mathbb{N}^0$ over the momentum-space orbit $\bar{C}$.

The quantization condition is then applied to a semiclassical electron in a crystal lattice. We consider the position-space orbit orthogonal to $\boldsymbol{B}$ to be closed and to correspond to the position-space orbit C as defined above. In other words, we assume a two-dimensional Brillouin zone where there is a *single* Fermi surface cross-section, leading to a unique value of the area enclosed within the orbit. In this manner, allowed orbits form a spectrum similar to the Landau levels spectrum.

The next derivation is based on Chang's course notes [11].

The magnetic field appears in this situation through $\hbar\boldsymbol{q} = \hbar\boldsymbol{k} - e\boldsymbol{A}$. It follows that

$$\oint_C \hbar\boldsymbol{q}\cdot d\boldsymbol{x} = \oint_C \hbar\boldsymbol{k}\cdot d\boldsymbol{x} - e\oint_C \boldsymbol{A}\cdot d\boldsymbol{x}\,. \tag{3.8}$$

Integrating (3.3b) with respect to time yields $\hbar\boldsymbol{k} = \hbar\boldsymbol{k}_0 - e\,[\boldsymbol{x} - \boldsymbol{x}_0]\times\boldsymbol{B}$, leading to

$$\begin{aligned}\oint_C \hbar\boldsymbol{k}\cdot d\boldsymbol{x} &= -e\oint_C [\boldsymbol{x}\times\boldsymbol{B}]\cdot d\boldsymbol{x} \\ &= -e\iint_S \{\nabla\times[\boldsymbol{x}\times\boldsymbol{B}]\}\cdot d\boldsymbol{S}\,,\end{aligned} \tag{3.9}$$

by applying Strokes' theorem and where S is the plane perpendicular to $\boldsymbol{B}$ enclosed by C. Note that the constant terms vanish by integrating over C because it is a closed loop. It is straightforward to evaluate $\nabla\times[\boldsymbol{x}\times\boldsymbol{B}]$ using component notation, resulting in

$$\nabla\times[\boldsymbol{x}\times\boldsymbol{B}] = -2\boldsymbol{B}\,. \tag{3.10}$$

Consequently,

$$\oint_C \hbar\boldsymbol{k}\cdot d\boldsymbol{x} = 2e\iint_S \boldsymbol{B}\cdot d\boldsymbol{S}\,. \tag{3.11}$$

By applying Stokes' theorem to the next term we obtain that

$$\begin{aligned} -e \oint_C \boldsymbol{A} \cdot d\boldsymbol{x} &= -e \iint_S [\nabla \times \boldsymbol{A}] \cdot d\boldsymbol{S} \\ &= -e \iint_S \boldsymbol{B} \cdot d\boldsymbol{S} \,. \end{aligned} \tag{3.12}$$

Finally, combining both results gives

$$\oint_C \hbar \boldsymbol{q} \cdot d\boldsymbol{x} = e \iint_S \boldsymbol{B} \cdot d\boldsymbol{S} \,. \tag{3.13}$$

The right-hand side of (3.13) is the magnetic flux through C multiplied by e. Recall that S is perpendicular to $\boldsymbol{B}$; hence, $\iint_S \boldsymbol{B} \cdot d\boldsymbol{S} = |\boldsymbol{B}| A(C)$ where $A(C)$ is the area enclosed by C. However, we are interested in expressing this in terms of the momentum-space orbit $\bar{C}$. As the orbits are related by a rotation of $\pi/2$ radians and a scale factor of $l_B^2 = \hbar/[e|\boldsymbol{B}|]$, it means that $A(C) = l_B^4 A(\bar{C})$. In such a way,

$$\oint_C \boldsymbol{q} \cdot d\boldsymbol{x} = l_B^2 A(\bar{C}) \,. \tag{3.14}$$

The quantization condition for a semiclassical electron in a crystal lattice then becomes

$$\frac{l_B^2}{2\pi} A(\bar{C}) = n + \frac{1}{2} - \Gamma_n(\bar{C}) \,. \tag{3.15}$$

This quantization condition is known as the Lifshitz-Onsager quantization rule. The spacing between allowed cross-sectional areas is set by the magnetic field strength $|\boldsymbol{B}|$ found in l_B^2 through this relation. Since the allowed areas appear as modulations in the electronic density of states thanks to level broadening [44], any observable depending on the density of states will exhibit quantum oscillations. Note in particular that the Fermi energy oscillates around a fixed value as $|\boldsymbol{B}|$ changes [44, Section 2.5], but this is only noticeable for small n where the semiclassical analysis does not hold regardless. Hence, the allowed levels will pass through the effectively constant Fermi surface periodically as a function of the *inverse* magnetic field strength $|\boldsymbol{B}|^{-1}$ with a frequency of

$$f = \frac{\hbar}{2\pi e} A(\bar{C}) \,. \tag{3.16}$$

The last equation is known as the Onsager's relation. Besides, the phase offset stems from the Maslov contribution and the Berry phase.

Consequently, quantum oscillations data can be used to derive the Berry phase. To achieve this, the allowed energy levels n found through the crests or troughs in quantum oscillations data are plotted against $|\boldsymbol{B}|^{-1}$ as shown in figure 3.2 and (3.15) is rearranged to fit their relationship:

$$n = f \cdot |\boldsymbol{B}|^{-1} + \Gamma_n(\bar{C}) - \frac{1}{2}\,, \tag{3.17}$$

where Onsager's relation gives the frequency f. Accordingly, the Berry phase $\gamma_n(\bar{C})$ — which equals to $2\pi\Gamma_n(\bar{C})$ — associated with the electronic momentum-space orbit $\bar{C}$ is obtained by finding the intercept of the free linear fit which results from extrapolating to $|\boldsymbol{B}|^{-1} \to 0^+$. Note that the numbering of the energy levels must be chosen such that $\Gamma_n(\bar{C}) \in [0, 1]$.

In the more general three-dimensional case, there is of course a continuum of possible Fermi surface cross-sections orthogonal to $\boldsymbol{B}$, but only the ones with the area as local extrema are relevant [33]. As a consequence, different quantum oscillation frequencies given by the Onsager's relation can coexist.

3.3. Cuprate Superconductors

A large amount of quantum oscillations data for the high-field normal state of the cuprates has been collected over the past few years [43], but it only has been used to obtain the Berry phase not long ago [13]. Using the method described in the previous section, Doiron-Leyraud *et al.* found according to their data shown in figure 3.2 that the Berry phase is equal within error to $0 \mod 2\pi$ in the hole-doped cuprates $YBa_2Cu_3O_y$, $YBa_2Cu_4O_8$, and $HgBa_2CuO_{4+\delta}$, and to $1.4\pi \mod 2\pi$ in the electron-doped compound $Nd_{2-x}Ce_xCuO_4$ [13]. Although these are three-dimensional materials, there is a unique quantum oscillation frequency since they are quasi-two-dimensional in their superconductive state [18].

According to Doiron-Leyraud *et al.*, their results constrain the possible theoretical models of the high-field normal state of cuprates, especially for the hole-doped compounds where the Berry phase was determined to be zero as it must imply that the Fermi pockets are formed in decoupled bands without Dirac-like features [13]. Additionally, they consider the non-zero Berry phase found in the electron-doped compound to be a robust result because the same value is obtained at different dopings with high precision.

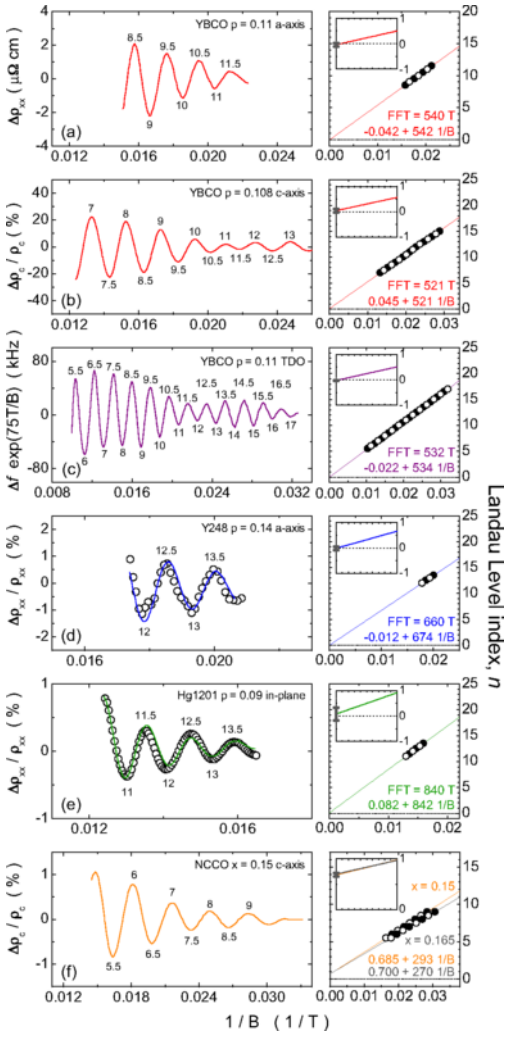

Figure 3.2: (Left column) Quantum oscillations in specified material under an external magnetic field $\boldsymbol{B}$ pointing along the c-axis in terms of $|\boldsymbol{B}|^{-1}$. All plots correspond to measurements of the electrical resistivity where the electric field points along specified axis except for the third plot which corresponds to measurements of the resonant-frequency shift of a tunnel diode oscillator (TDO). The in-plane resistivity is inversely proportional to the c-axis resistivity while it is proportional to changes in the TDO resonant frequency. The level indices n are associated with their corresponding peak or trough accordingly. (Right column) Level indices n in terms of $|\boldsymbol{B}|^{-1}$ with the corresponding linear fit. The equation for every linear fit and the frequencies obtained through fast Fourier transform are given. The Berry phase contribution is equal to the intercept. Reproduced from [13].

4. πLC MODEL OF THE PSEUDOGAP IN THE CUPRATES

In an effort to describe the pseudogap phase of cuprates, Varma suggested in 1997 a competing order model, a three-band model with the particularity of having current circulating in each unit cell as in figure 4.2, leading to this phase being referred to as the circulating current phase [50]. It was argued then and shown later that the properties of this phase are similar to those of the pseudogap phase [51]. A few years later, weak magnetic moments were detected below T^* through spin-polarized neutron scattering experiments [15, 24, 25, 45], influencing Varma to put forward the idea of intra-unit cell loop currents (LCs) [52].

More recently, Bulut *et al.* have investigated a phase having a staggered pattern of LCs, which they called πLC phase [7]. It features the ordering wave vector $\boldsymbol{Q} = \left(\frac{\pi}{a}, \frac{\pi}{a}\right)$ where a is the lattice spacing. This wave vector is the one relevant to cuprates [29] and can also be found in other proposals for competing order, such as the d-density wave (DDW) state [9]. As demonstrated in figure 4.1, it plays an essential role in the Fermi surface reconstruction suggested to be behind the small Fermi surface of the pseudogap phase and the hole and electron pockets observed in experiments [8]. As it will be shown throughout this section, a d-wave-symmetric gap will be maintained in the energy spectrum of the πLC state, similar to the DDW state and in agreement with the pseudogap phase [29]. Additionally, the πLC state breaks time-reversal symmetry and could explain the Kerr effect observed in the pseudogap phase through experiments [7].

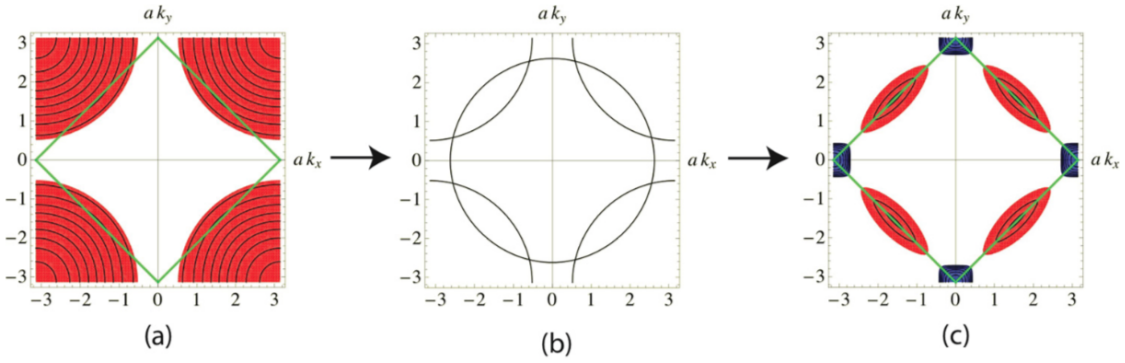

Figure 4.1: Fermi surface reconstruction due to the ordering wave vector $\boldsymbol{Q} = \left(\frac{\pi}{a}, \frac{\pi}{a}\right)$. (a) Without ordering wave vector, the Fermi surface is formed by one hole pocket. The area within the green square corresponds to the reduced Brillouin zone BZ' and the black lines are contour lines. (b) Fermi surface shifted by $\boldsymbol{Q}$ on top of the original Fermi surface. (c) Reconstructed Fermi surface formed by hole and electron pockets, shown in red and blue respectively. This dispersion shares its periodicity with BZ'. Adapted from [8].

The πLC model analyzed in this work is the same as the one explored by Bulut *et al.* [7], but an alternate current pattern will also be investigated — ultimately leading to the same Berry phase.

The πLC Hamiltonian is written on a square lattice and each site corresponds to a unit cell, i.e., a CuO_2 plane containing a copper $d_{x^2-y^2}$ orbital and oxygen p_x and p_y orbitals, denoted by Cu$d_{x^2-y^2}$, Op_x, and Op_y. The relevant bonds are the nearest neighbour p–d and p–p bonds. As discussed before, these bonds exhibit intra-unit cell loop currents, equivalent to directional hopping. Additionally, the current must switch direction between unit cells like in figure 4.2 to obtain the Fermi surface reconstruction found in figure 4.1. Any state under such considerations breaks both time-reversal and lattice-translation symmetries. The specific staggered pattern of intertwined LCs studied by Bulut *et al.* [7] is shown in figure 4.2. Note that this state has 4-fold rotational symmetry and conserves current.

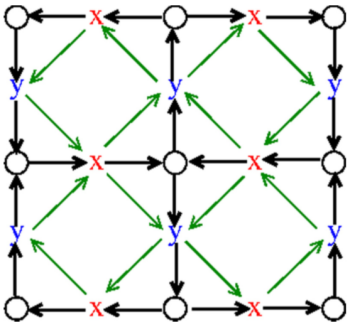

Figure 4.2: Staggered pattern of loop currents studied by Bulut *et al.* [7] Cu$d_{x^2-y^2}$, Op_x, and Op_y orbitals are represented by open circles,"x", and "y" respectively. The directional hopping on p–d and p–p bonds are shown by black and green arrows respectively. Reproduced from [7].

The πLC Hamiltonian denoted by $\hat{H}$ can be broken down in two parts: the kinetic energy $\hat{H}_0$ and the charge order $\hat{H}'$. Each one can be solved separately. However, a mean-field approach is needed to solve the charge order, which will lead to the final diagonalized Hamiltonian being a mean-field approximation.

4.1. The Mean-Field Hamiltonian

4.1.1. Kinetic Energy

The choice of unit cell for a single CuO_2 plane and of orbital phase convention can be found in figure 4.3. The inequivalent bonds are numbered to distinguish them from one another. We assume a total of N^2 unit cells with periodic boundary conditions. Each unit cell will be labeled by its position through a vector $\boldsymbol{i} = \left(i^x,\ i^y\right) \in \mathbb{Z}_N^2$. Also, the orbitals will be labeled by d for Cu$d_{x^2-y^2}$, x for Op_x, and y for Op_y. Let $\boldsymbol{R_{i\alpha}}$ be the position vector

of orbital α in unit cell $\boldsymbol{i}$: it can be expressed as $\boldsymbol{R}_{\boldsymbol{i}\alpha} = \boldsymbol{R}_{\boldsymbol{i}} + \boldsymbol{\delta}_\alpha$ with $\boldsymbol{R}_{\boldsymbol{i}} \equiv a\boldsymbol{i}$ where a is the lattice spacing corresponding to the distance between two d orbitals, and $\boldsymbol{\delta}_\alpha$ is the displacement vector defined such that $\boldsymbol{\delta}_d \equiv \boldsymbol{0}$, $\boldsymbol{\delta}_x \equiv \frac{a}{2}\hat{\boldsymbol{x}}$, and $\boldsymbol{\delta}_y \equiv \frac{a}{2}\hat{\boldsymbol{y}}$.

Let $\hat{c}_{\boldsymbol{i}\alpha\sigma}/\hat{c}^\dagger_{\boldsymbol{i}\alpha\sigma}/\hat{n}_{\boldsymbol{i}\alpha\sigma}$ be the annihilation/creation/number operator for an electron in orbital α of unit cell $\boldsymbol{i}$ and spin σ. Let ϵ_α be the orbital energy of orbital α and $t_{\boldsymbol{j}\beta,\boldsymbol{i}\alpha}$ the tunneling matrix element from orbital α in unit cell $\boldsymbol{i}$ to orbital β in unit cell $\boldsymbol{j}$. The kinetic energy is then

$$\hat{H}_0 = \sum_{\boldsymbol{i}\alpha\sigma} \epsilon_\alpha \hat{n}_{\boldsymbol{i}\alpha\sigma} + \sum_{\langle \boldsymbol{i}\alpha\sigma, \boldsymbol{j}\beta\sigma\rangle} t_{\boldsymbol{j}\beta,\boldsymbol{i}\alpha} \hat{c}^\dagger_{\boldsymbol{j}\beta\sigma} \hat{c}_{\boldsymbol{i}\alpha\sigma} \,, \tag{4.1}$$

where the sum over $\langle \boldsymbol{i}\alpha\sigma, \boldsymbol{j}\beta\sigma\rangle$ includes nearest neighbor p–d and p–p bonds [7]. The spin labels can be omitted here. Note that $t_{\boldsymbol{j}\beta,\boldsymbol{i}\alpha}$ can be expressed as $t^n_{\beta\alpha}$, in terms of α, β, and n the inequivalent bond between $\boldsymbol{i}\alpha$ and $\boldsymbol{j}\beta$. What is interesting about this expression of the tunneling matrix elements is that $\boldsymbol{i}$ or $\boldsymbol{j}$ are not needed anymore and only the inequivalent bond and corresponding orbitals are required. Under a typical parameter set, $t_{pd} = 1$ is set to define the unit energy with $t_{pp} = -0.5$ and $\epsilon_d - \epsilon_p = 2.5$, along with other parameters — which will be defined later — set to $U_d = 9$, $U_p = 3$, $V_{pd} = 2.2$, $V_{pp} = 1$, $z_{pd} = 0.04$, and $z_{pp} = z_{pd}/3$, in accordance with experimental data [7, 19].

Let $\hat{c}_{\boldsymbol{k}\alpha}/\hat{c}^\dagger_{\boldsymbol{k}\alpha}/\hat{n}_{\boldsymbol{k}\alpha}$ be the annihilation/creation/number operator for an electron in orbital α with crystal momentum $\hbar\boldsymbol{k}$ for $\boldsymbol{k} = \begin{pmatrix} k^x, & k^y \end{pmatrix} \in \frac{2\pi}{aN}\mathbb{Z}^2_N$. By periodicity, the Brillouin zone BZ is taken to be the set $\frac{1}{a}[-\pi, \pi] \times \frac{1}{a}[-\pi, \pi]$. The momentum-space operators are related

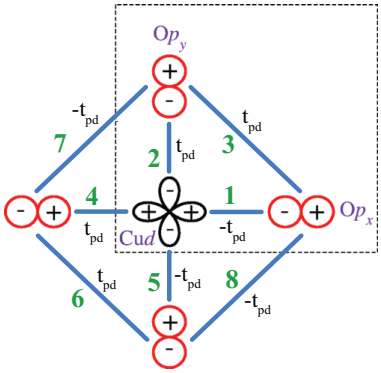

Figure 4.3: All inequivalent bonds of the CuO_2 plane. The unit cell chosen is indicated by the dashed box. All inequivalent bonds are numbered in green and their orbital phase convention is given by the sign of its hopping matrix element. Adapted from [7].

to their position-space counterparts through the Fourier transform:

$$\begin{aligned} \hat{c}_{\boldsymbol{k}\alpha} &= \tfrac{1}{N}\sum_{\boldsymbol{i}} e^{-i\boldsymbol{k}\cdot\boldsymbol{R}_{\boldsymbol{i}\alpha}}\hat{c}_{\boldsymbol{i}\alpha} & \hat{c}^{\dagger}_{\boldsymbol{k}\alpha} &= \tfrac{1}{N}\sum_{\boldsymbol{i}} e^{i\boldsymbol{k}\cdot\boldsymbol{R}_{\boldsymbol{i}\alpha}}\hat{c}^{\dagger}_{\boldsymbol{i}\alpha} \\ \hat{c}_{\boldsymbol{i}\alpha} &= \tfrac{1}{N}\sum_{\boldsymbol{k}} e^{i\boldsymbol{k}\cdot\boldsymbol{R}_{\boldsymbol{i}\alpha}}\hat{c}_{\boldsymbol{k}\alpha} & \hat{c}^{\dagger}_{\boldsymbol{i}\alpha} &= \tfrac{1}{N}\sum_{\boldsymbol{k}} e^{-i\boldsymbol{k}\cdot\boldsymbol{R}_{\boldsymbol{i}\alpha}}\hat{c}^{\dagger}_{\boldsymbol{k}\alpha}\,. \end{aligned} \tag{4.2}$$

Let $\boldsymbol{\delta}^n_{\beta\alpha} \equiv \boldsymbol{R}_{\boldsymbol{j}\beta} - \boldsymbol{R}_{\boldsymbol{i}\alpha}$ be the bond vector from orbital α to β on the inequivalent bond n for corresponding $\boldsymbol{i}$ and $\boldsymbol{j}$. To generalize this further, let also $\boldsymbol{\delta}^n_{\alpha\alpha} = \boldsymbol{0}$ for any α and n. Consequently, it is obtained that

$$\hat{c}^{\dagger}_{\boldsymbol{j}\beta}\hat{c}_{\boldsymbol{i}\alpha} = \tfrac{1}{N^2}\sum_{\boldsymbol{k},\boldsymbol{k}'} e^{-i\boldsymbol{k}'\cdot\boldsymbol{\delta}^n_{\beta\alpha}} e^{i[\boldsymbol{k}-\boldsymbol{k}']\cdot\boldsymbol{R}_{\boldsymbol{i}\alpha}}\hat{c}^{\dagger}_{\boldsymbol{k}'\beta}\hat{c}_{\boldsymbol{k}\alpha}\,, \tag{4.3}$$

for n the inequivalent bond between $\boldsymbol{i}\alpha$ and $\boldsymbol{j}\beta$. In particular, the information about $\boldsymbol{j}$ is not needed in the expression above if n is known, meaning that a sum over $\boldsymbol{j}$ can be replaced by a sum over n instead. Since $\frac{1}{N^2}\sum_{\boldsymbol{i}} e^{i\boldsymbol{k}\cdot\boldsymbol{R}_{\boldsymbol{i}\alpha}} = \delta_{\boldsymbol{k},\boldsymbol{0}}$, it follows that

$$\begin{aligned} \sum_{\boldsymbol{i}\alpha}\epsilon_\alpha\hat{n}_{\boldsymbol{i}\alpha} &= \sum_{\boldsymbol{k}\alpha,\boldsymbol{k}'}\epsilon_\alpha\left[\tfrac{1}{N^2}\sum_{\boldsymbol{i}} e^{i[\boldsymbol{k}-\boldsymbol{k}']\cdot\boldsymbol{R}_{\boldsymbol{i}\alpha}}\right]\hat{c}^{\dagger}_{\boldsymbol{k}'\alpha}\hat{c}_{\boldsymbol{k}\alpha} \\ &= \sum_{\boldsymbol{k}\alpha}\epsilon_\alpha\hat{n}_{\boldsymbol{k}\alpha}\,, \end{aligned} \tag{4.4}$$

$$\begin{aligned} \sum_{\langle\boldsymbol{i}\alpha,\boldsymbol{j}\beta\rangle} t_{\boldsymbol{j}\beta,\boldsymbol{i}\alpha}\hat{c}^{\dagger}_{\boldsymbol{j}\beta}\hat{c}_{\boldsymbol{i}\alpha} &= \sum_{\boldsymbol{k}\alpha,\boldsymbol{k}'\beta,n} t^n_{\beta\alpha}e^{-i\boldsymbol{k}'\cdot\boldsymbol{\delta}^n_{\beta\alpha}}\left[\tfrac{1}{N^2}\sum_{\boldsymbol{i}} e^{i[\boldsymbol{k}-\boldsymbol{k}']\cdot\boldsymbol{R}_{\boldsymbol{i}\alpha}}\right]\hat{c}^{\dagger}_{\boldsymbol{k}'\beta}\hat{c}_{\boldsymbol{k}\alpha} \\ &= \sum_{\boldsymbol{k}\alpha\beta,n} t^n_{\beta\alpha}e^{-i\boldsymbol{k}\cdot\boldsymbol{\delta}^n_{\beta\alpha}}\hat{c}^{\dagger}_{\boldsymbol{k}\beta}\hat{c}_{\boldsymbol{k}\alpha} \\ &\equiv \sum_{\boldsymbol{k}\alpha\beta} f_{\beta\alpha}(\boldsymbol{k})\hat{c}^{\dagger}_{\boldsymbol{k}\beta}\hat{c}_{\boldsymbol{k}\alpha}\,, \end{aligned} \tag{4.5}$$

where $f_{\beta\alpha}(\boldsymbol{k})$ must clearly satisfy $f^*_{\beta\alpha}(\boldsymbol{k}) = f_{\alpha\beta}(\boldsymbol{k})$. Letting $\Psi^{\dagger}_{\boldsymbol{k}} \equiv \begin{bmatrix}\hat{c}^{\dagger}_{\boldsymbol{k}d} & \hat{c}^{\dagger}_{\boldsymbol{k}x} & \hat{c}^{\dagger}_{\boldsymbol{k}y}\end{bmatrix}$,

$$\begin{aligned} \hat{H}_0 &= \sum_{\boldsymbol{k}}\Psi^{\dagger}_{\boldsymbol{k}}\begin{bmatrix}\epsilon_d & f^*_{xd}(\boldsymbol{k}) & f^*_{yd}(\boldsymbol{k}) \\ f_{xd}(\boldsymbol{k}) & \epsilon_x & f^*_{yx}(\boldsymbol{k}) \\ f_{yd}(\boldsymbol{k}) & f_{yx}(\boldsymbol{k}) & \epsilon_y\end{bmatrix}\Psi_{\boldsymbol{k}} \\ &\equiv \sum_{\boldsymbol{k}}\Psi^{\dagger}_{\boldsymbol{k}}\boldsymbol{H}_0(\boldsymbol{k})\Psi_{\boldsymbol{k}}\,. \end{aligned} \tag{4.6}$$

Introducing the ordering wave vector $\boldsymbol{Q} = \left(\frac{\pi}{a},\ \frac{\pi}{a}\right)$ for the Fermi surface reconstruction,

$$\hat{H}_0 = \sum_{\boldsymbol{k}\in BZ'} \begin{bmatrix} \Psi^\dagger_{\boldsymbol{k}} & \Psi^\dagger_{\boldsymbol{k}+\boldsymbol{Q}} \end{bmatrix} \begin{bmatrix} \boldsymbol{H}_0(\boldsymbol{k}) & \boldsymbol{0} \\ \boldsymbol{0} & \boldsymbol{H}_0(\boldsymbol{k}+\boldsymbol{Q}) \end{bmatrix} \begin{bmatrix} \Psi_{\boldsymbol{k}} \\ \Psi_{\boldsymbol{k}+\boldsymbol{Q}} \end{bmatrix}, \tag{4.7}$$

where BZ' is the reduced Brillouin zone pictured in figure 4.4 consisting of the closed ball of radius $\frac{\pi}{a}$ centered at the origin with the p-norm L_1.

Next, a gauge transformation is applied:

$$\begin{aligned} \hat{c}_{\boldsymbol{k}x} &\to i\hat{c}_{\boldsymbol{k}x} & \hat{c}_{\boldsymbol{k}y} &\to i\hat{c}_{\boldsymbol{k}y} \\ \hat{c}^\dagger_{\boldsymbol{k}x} &\to -i\hat{c}^\dagger_{\boldsymbol{k}x} & \hat{c}^\dagger_{\boldsymbol{k}y} &\to -i\hat{c}^\dagger_{\boldsymbol{k}y}\,. \end{aligned} \tag{4.8}$$

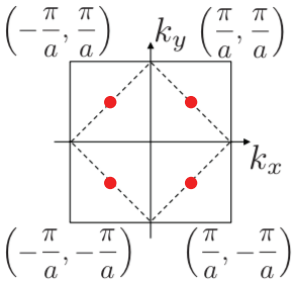

Figure 4.4: Full and reduced Brillouin zone shown by the solid and the dashed square respectively. The red points denote D. Adapted from [29].

explicitly, we have after the gauge transformation that

$$\boldsymbol{H}_0(\boldsymbol{k}) = \begin{bmatrix} \epsilon_d & 2t_{pd}s_x & -2t_{pd}s_y \\ 2t_{pd}s_x & \epsilon_p & 4t_{pp}s_xs_y \\ -2t_{pd}s_y & 4t_{pp}s_xs_y & \epsilon_p \end{bmatrix}, \tag{4.9}$$

as $\epsilon_x = \epsilon_y \equiv \epsilon_p$ and for $s_x \equiv \sin\left(\frac{a}{2}k^x\right)$ and $s_y \equiv \sin\left(\frac{a}{2}k^y\right)$.

It is useful to investigate the eigenvalues $E_n(\boldsymbol{k})$ of $\boldsymbol{H}_0(\boldsymbol{k})$ and their corresponding eigenstates $|n(\boldsymbol{k})\rangle$ for $\boldsymbol{k} \in BZ$ under a typical parameter set [7, 19]. The details of this analysis can be found in appendix D. What comes out of it is that there is an energy gap $\epsilon_d - \epsilon_p$ between the highest energy band and the two other bands. Furthermore, the energy bands have the property that $E_n(\boldsymbol{k}+\boldsymbol{Q}) = E_n(\boldsymbol{k})$ if and only if $\boldsymbol{k} \in \partial BZ'$.

4.1.2. Mean-Field Decomposition of the Charge Order

Let U_α and $V_{\beta\alpha}$ be the intraorbital and interorbital Coulomb interactions respectively. The charge order in position space is

$$\hat{H}' = \sum_{\boldsymbol{i}\alpha} U_\alpha \hat{n}_{\boldsymbol{i}\alpha\uparrow}\hat{n}_{\boldsymbol{i}\alpha\downarrow} + \tfrac{1}{2} \sum_{\langle \boldsymbol{i}\alpha\sigma, \boldsymbol{j}\beta\sigma'\rangle} V_{\beta\alpha}\hat{n}_{\boldsymbol{j}\beta\sigma'}\hat{n}_{\boldsymbol{i}\alpha\sigma}\,, \tag{4.10}$$

where the sum over $\langle \boldsymbol{i}\alpha\sigma, \boldsymbol{j}\beta\sigma'\rangle$ includes nearest neighbor p–d and p–p bonds [7].

From H', it is possible to obtain its mean-field version $\hat{H}'_{MF}$ which includes circulating currents. The intraorbital interactions lead to Hartree shifts to the orbital energies which merely renormalize in ϵ_d and ϵ_p. Since we are looking for solutions that do not break spin-rotational symmetries, the spin labels are omitted for the rest of this work. The interorbital interactions can be decomposed in terms of the circulating current: the Hermitian operator $\hat{J}_{\boldsymbol{j}\beta,\boldsymbol{i}\alpha} = -it_{\boldsymbol{j}\beta,\boldsymbol{i}\alpha}[\hat{c}^\dagger_{\boldsymbol{j}\beta}\hat{c}_{\boldsymbol{i}\alpha} - \hat{c}^\dagger_{\boldsymbol{i}\alpha}\hat{c}_{\boldsymbol{j}\beta}]$ is the current operator for the bond between $\boldsymbol{i}\alpha$ and $\boldsymbol{j}\beta$ such that the current flows from $\boldsymbol{i}\alpha$ to $\boldsymbol{j}\beta$ if $\langle \hat{J}_{\boldsymbol{j}\beta,\boldsymbol{i}\alpha}\rangle \equiv z_{\boldsymbol{j}\beta,\boldsymbol{i}\alpha} > 0$ and from $\boldsymbol{j}\beta$ to $\boldsymbol{i}\alpha$ if $z_{\boldsymbol{j}\beta,\boldsymbol{i}\alpha} < 0$.

The framework described above to obtain the mean-field version of H' has been done explicitely in appendix E, leading to

$$\hat{H}'_{MF} = \sum_{\boldsymbol{k}\in BZ'} \begin{bmatrix} \Psi^\dagger_{\boldsymbol{k}} & \Psi^\dagger_{\boldsymbol{k}+\boldsymbol{Q}} \end{bmatrix} \begin{bmatrix} \tilde{\boldsymbol{\epsilon}} & \boldsymbol{H}_1(\boldsymbol{k}) \\ \boldsymbol{H}_1^\dagger(\boldsymbol{k}) & \tilde{\boldsymbol{\epsilon}} \end{bmatrix} \begin{bmatrix} \Psi_{\boldsymbol{k}} \\ \Psi_{\boldsymbol{k}+\boldsymbol{Q}} \end{bmatrix}, \tag{4.11}$$

where an explicit expression for $\boldsymbol{H}_1(\boldsymbol{k})$ depends on the current pattern. Note that $\tilde{\boldsymbol{\epsilon}}$ simply represents a shift in the orbital energies equivalent to $\tilde{\epsilon}_d = V_{pd} + 2V_{pp}$ and $\tilde{\epsilon}_p = 2V_{pd}$.

The focus needs to be made on *physical* current patterns — meaning that the current is conserved on each orbital site — with 4-fold rotational symmetry. Such current patterns have the particularity that all elements of $\boldsymbol{H}_1(\boldsymbol{k})$ *after* the gauge transformation are purely imaginary. There are only two possible inequivalent physical current patterns with 4-fold rotational symmetry, and the one investigated by Bulut *et al.* [7] shown in figure 4.2 is one of them. The second current pattern can be obtained from the one in figure 4.2 by merely inverting the current along p–p bonds.

Throughout the rest of this work, the two current patterns satisfying the above conditions will be distinguished by $\phi \in \{\pm 1\}$ with the current pattern investigated by Bulut *et al.* [7] corresponding to $\phi = 1$. Explicitly, we have for these two current patterns under the gauge transformation from (4.8) that $\tilde{\boldsymbol{\epsilon}}$ stays invariant while

$$\boldsymbol{H}_1(\boldsymbol{k}) = \begin{bmatrix} 0 & 2iR_{pd}c_x & 2iR_{pd}c_y \\ -2iR_{pd}s_x & 0 & -4i\phi R_{pp}s_x c_y \\ -2iR_{pd}s_y & 4i\phi R_{pp}c_x s_y & 0 \end{bmatrix}, \tag{4.12}$$

for $R_{pd} \equiv \frac{V_{pd}z_{pd}}{t_{pd}}$, $R_{pp} \equiv \frac{V_{pp}z_{pp}}{t_{pp}}$, $c_x \equiv \cos\left(\frac{a}{2}k^x\right)$ and $c_y \equiv \cos\left(\frac{a}{2}k^y\right)$.

4.1.3. Full Mean-Field Hamiltonian

Combining both (4.7) and (4.11) yields the effective mean-field πLC Hamiltonian:

$$\begin{aligned}\hat{H}_{MF} &= \sum_{\boldsymbol{k}\in BZ'} \begin{bmatrix}\Psi_{\boldsymbol{k}}^\dagger & \Psi_{\boldsymbol{k}+\boldsymbol{Q}}^\dagger\end{bmatrix} \begin{bmatrix}\boldsymbol{H}_0(\boldsymbol{k}) & \boldsymbol{H}_1(\boldsymbol{k}) \\ \boldsymbol{H}_1^\dagger(\boldsymbol{k}) & \boldsymbol{H}_0(\boldsymbol{k}+\boldsymbol{Q})\end{bmatrix} \begin{bmatrix}\Psi_{\boldsymbol{k}} \\ \Psi_{\boldsymbol{k}+\boldsymbol{Q}}\end{bmatrix} \\ &\equiv \sum_{\boldsymbol{k}\in BZ'} \overline{\Psi}_{\boldsymbol{k}}^\dagger \boldsymbol{H}_{MF}(\boldsymbol{k}) \overline{\Psi}_{\boldsymbol{k}}\,,\end{aligned} \tag{4.13}$$

where $\epsilon_d \to \epsilon_d + \tilde{\epsilon}_d \equiv \varepsilon_d$ and $\epsilon_p \to \epsilon_p + \tilde{\epsilon}_p \equiv \varepsilon_p$ in $\boldsymbol{H}_0(\boldsymbol{k})$. $\boldsymbol{H}_{MF}(\boldsymbol{k})$ has the particularity of having real diagonal block matrices and imaginary off-diagonal block matrices.

Define the unitless parameter $\lambda \equiv z_{pd}/t_{pd}$. Then,

$$\boldsymbol{H}_{MF}(\boldsymbol{k}) = \begin{bmatrix}\boldsymbol{H}_0(\boldsymbol{k}) & -i\lambda \boldsymbol{V}(\boldsymbol{k}) \\ i\lambda \boldsymbol{V}^T(\boldsymbol{k}) & \boldsymbol{H}_0(\boldsymbol{k}+\boldsymbol{Q})\end{bmatrix}, \tag{4.14}$$

for real matrix $\boldsymbol{V}(\boldsymbol{k}) \equiv i\lambda^{-1}\boldsymbol{H}_1(\boldsymbol{k})$. Note that the matrix elements of $\boldsymbol{V}(\boldsymbol{k})$ are of the order of magnitude of 1 or lower for any $\boldsymbol{k}$ while $\lambda \ll 1$ under a typical parameter set. Four points are of particular interest here: the points $\boldsymbol{k}^*$ such that $|k^{*x}| = |k^{*y}| = \frac{\pi}{2a}$, which form a set that we denote by D. As seen in figure 4.4, they are located in the middle of the quadrants of the full Brillouin zone. As discussed in appendix F, $\boldsymbol{V}(\boldsymbol{k})$ has the property that within each individual hole pocket, $\langle n(\boldsymbol{k})|\, \boldsymbol{V}(\boldsymbol{k})\, |n(\boldsymbol{k}+\boldsymbol{Q})\rangle = 0$ for $\boldsymbol{k} \in \partial BZ'$ if and only if $\boldsymbol{k} \in D$. Hence, the momenta in D correspond to the degeneracy points.

Recall from section 4.1.1 that $E_n(\boldsymbol{k}+\boldsymbol{Q}) = E_n(\boldsymbol{k})$ if and only if $\boldsymbol{k} \in \partial BZ'$. According to this along with the property of $\boldsymbol{V}(\boldsymbol{k})$ above, the eigenstates of $\boldsymbol{H}_{MF}(\boldsymbol{k}^*)$ for $\boldsymbol{k}^* \in D$ are

$$|n_\uparrow(\boldsymbol{k}^*)\rangle = \begin{bmatrix}|n(\boldsymbol{k}^*)\rangle \\ \boldsymbol{0}\end{bmatrix} \qquad |n_\downarrow(\boldsymbol{k}^*)\rangle = \begin{bmatrix}\boldsymbol{0} \\ |n(\boldsymbol{k}^*+\boldsymbol{Q})\rangle\end{bmatrix}, \tag{4.15}$$

where both $|n_\uparrow(\boldsymbol{k}^*)\rangle$ and $|n_\downarrow(\boldsymbol{k}^*)\rangle$ share the eigenvalue $E_n(\boldsymbol{k}^*)$ for every n. Hence, all the eigenvalues of $\boldsymbol{H}_{MF}(\boldsymbol{k}^*)$ for the momenta $\boldsymbol{k}^* \in D$ are 2-fold degenerate. An alternate and more rigorous proof is given in appendix F.

4.2. Projection of the Hamiltonian on the Two Highest Energy Bands

We put our focus on the two highest energy bands which are half-filled and related to the energy of the Cu$d_{x^2-y^2}$ orbital [49]; the other energy bands are irrelevant because they are restricted to energies well below the Fermi energy. We start our investigation by looking at the energy bands in the reduced Brillouin zone BZ'. We can try to find the eigenvalues of $\boldsymbol{H}_{MF}(\boldsymbol{k})$ at any point $\boldsymbol{k} \in BZ'$, but those eigenvalues are practically impossible to find analytically because it requires solving a polynomial equation of degree 6.

We must rely on perturbation theory for an energy subspace as described in Section B.2 to simplify the task of finding explicit expressions for the dispersion relation. The unperturbed Hamiltonian is taken to be

$$\begin{bmatrix} \boldsymbol{H}_0(\boldsymbol{k}) & \boldsymbol{0} \\ \boldsymbol{0} & \boldsymbol{H}_0(\boldsymbol{k}+\boldsymbol{Q}) \end{bmatrix}. \tag{4.16}$$

Let the energy eigenvalues and corresponding eigenstates of $\boldsymbol{H}_0(\boldsymbol{k})$ be denoted by $E_n(\boldsymbol{k})$ and $|n(\boldsymbol{k})\rangle$ for $n \in \{\pm, 0\}$ such that $E_+(\boldsymbol{k}) \geq E_0(\boldsymbol{k}), E_-(\boldsymbol{k})$. Hence, the unperturbed energy

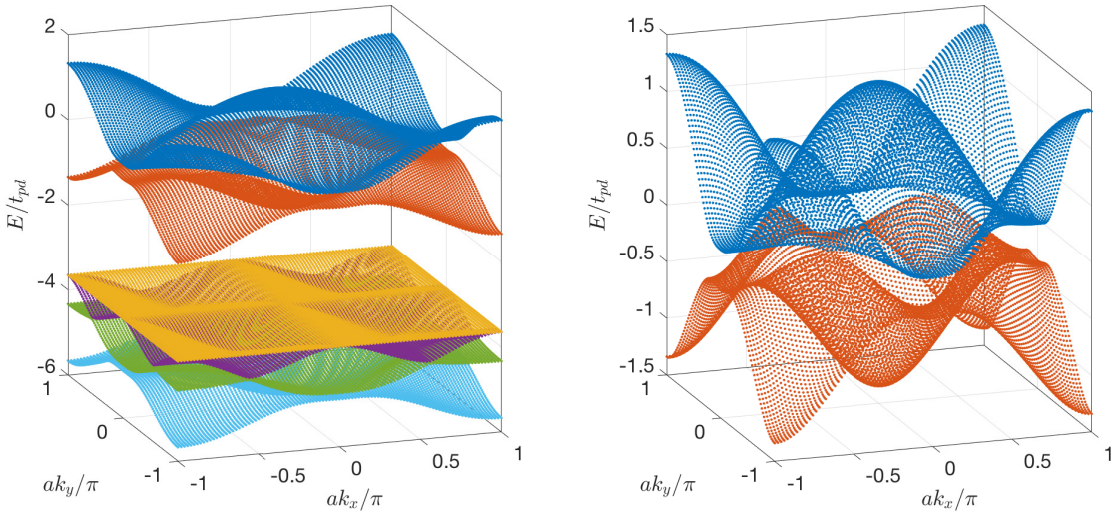

(a) (b)

Figure 4.5: (a) Dispersion relation over the full Brillouin zone for the mean-field πLC Hamiltonian as investigated by Bulut *et al.* [7] ($\phi = 1$) under a typical parameter set. The zero energy corresponds to the Fermi energy. (b) Zoom on the highest energy bands. The Dirac points are visible at $\boldsymbol{k} \in D$.

eigenvalues are $E_n(\boldsymbol{k})$ and $E_n(\boldsymbol{k}+\boldsymbol{Q})$ with respective corresponding eigenstates

$$|n_\uparrow(\boldsymbol{k})\rangle = \begin{bmatrix} |n(\boldsymbol{k})\rangle \\ \mathbf{0} \end{bmatrix} \qquad |n_\downarrow(\boldsymbol{k})\rangle = \begin{bmatrix} \mathbf{0} \\ |n(\boldsymbol{k}+\boldsymbol{Q})\rangle \end{bmatrix}. \tag{4.17}$$

As pointed out above, we are only interested in the two highest energy bands. According to section 4.1.1, the two highest energy bands are separated from the four other bands by $\Delta\varepsilon \equiv \varepsilon_d - \varepsilon_p$ under a typical parameter set. As $\max_{i,j} |\lambda V_{ij}(\boldsymbol{k})|/|\Delta\varepsilon| \lesssim \lambda \ll 1$ in this case, the two highest energy eigenstates $|+_\uparrow(\boldsymbol{k})\rangle$ and $|+_\downarrow(\boldsymbol{k})\rangle$ form a subspace that is separated well enough energetically from the rest of the Hilbert space to apply perturbation theory as layed out in appendix B.2 and effectively project the mean-field Hamiltonian onto this subspace. Thus, the projected Hamiltonian at any point $\boldsymbol{k}$ is

$$\begin{aligned} \boldsymbol{H}_U(\boldsymbol{k}) &= \begin{bmatrix} E_+(\boldsymbol{k}) & -i\lambda\Delta(\boldsymbol{k}) \\ i\lambda\Delta(\boldsymbol{k}) & E_+(\boldsymbol{k}+\boldsymbol{Q}) \end{bmatrix} \\ &= \bar{E}(\boldsymbol{k})\boldsymbol{I} + \lambda\Delta(\boldsymbol{k})\boldsymbol{\sigma}_2 + \varepsilon(\boldsymbol{k})\boldsymbol{\sigma}_3\,, \end{aligned} \tag{4.18}$$

where we have defined $\bar{E}(\boldsymbol{k}) \equiv \frac{1}{2}[E_+(\boldsymbol{k}) + E_+(\boldsymbol{k}+\boldsymbol{Q})]$, $\Delta(\boldsymbol{k}) \equiv \langle +(\boldsymbol{k})|\, \boldsymbol{V}(\boldsymbol{k})\, |+(\boldsymbol{k}+\boldsymbol{Q})\rangle$, and $\varepsilon(\boldsymbol{k}) \equiv \frac{1}{2}[E_+(\boldsymbol{k}) - E_+(\boldsymbol{k}+\boldsymbol{Q})]$.

The first thing to notice is that $\varepsilon(\boldsymbol{k}) = 0$ if and only if $\boldsymbol{k} \in \partial BZ'$. Since we have within each individual hole pocket that $\Delta(\boldsymbol{k}) = 0$ for $\boldsymbol{k} \in \partial BZ'$ if and only if $\boldsymbol{k} \in D$, it means that the projection does not lift the degeneracies of momenta in D and that there is also no other degeneracy. Thus, the highest energy bands of the full mean-field Hamiltonian and of the projected Hamiltonian share the same degeneracy points located at the momenta in D and there is no other degeneracy. Supporting this fact, it can easily be observed numerically through figure 4.5 (b) that there is no other degeneracy associated with the two highest energy bands.

4.3. Berry Phase of the Projected Hamiltonian

As we are interested in the hole pockets surrounding the degeneracy points, we have to consider the Hamiltonian in a shifted momentum space. We thus express any point $\boldsymbol{k}$ in the Brillouin zone BZ in terms of a vector $\tilde{\boldsymbol{k}}$ centered at one of the degeneracy points. As detailed in appendix G, taking $\boldsymbol{k} = \left(\sigma_x[\frac{\pi}{2a} + \tilde{k}^x],\ \sigma_y[\frac{\pi}{2a} + \tilde{k}^y]\right)$ for $\sigma_x, \sigma_y \in \{\pm 1\}$ yields

$$\varepsilon(\boldsymbol{k}) = \tilde{\boldsymbol{k}} \cdot \boldsymbol{\varepsilon}^{(1)} + \mathcal{O}(|\tilde{\boldsymbol{k}}|^2)\,, \tag{4.19a}$$

$$\Delta(\boldsymbol{k}) = \tilde{\boldsymbol{k}} \cdot \boldsymbol{\Delta}^{(1)} + \mathcal{O}(|\tilde{\boldsymbol{k}}|^2)\,, \tag{4.19b}$$

for some vectors $\boldsymbol{\varepsilon}^{(1)}$ and $\boldsymbol{\Delta}^{(1)}$ which satisfy $|\boldsymbol{\Delta}^{(1)} \times \boldsymbol{\varepsilon}^{(1)}| \neq 0$. Let $\sigma \in \{\pm 1\}$ be such that $\boldsymbol{\Delta}^{(1)} \times \boldsymbol{\varepsilon}^{(1)} = \sigma |\boldsymbol{\Delta}^{(1)} \times \boldsymbol{\varepsilon}^{(1)}| \hat{\boldsymbol{z}}$. For the Hamiltonian $\boldsymbol{H}_U(\boldsymbol{k})$, the Berry phase along a path C corresponding to an orbit around the hole pocket surrounding the point $\frac{\pi}{2a}\left(\sigma_x,\ \sigma_y\right) \in D$ where $\sigma_x, \sigma_y \in \{\pm 1\}$ in momentum space can be calculated with the help of section 2.5.1:

$$\gamma_{\pm}(C) = \mp \sigma \sigma_x \sigma_y \pi\,. \tag{4.20}$$

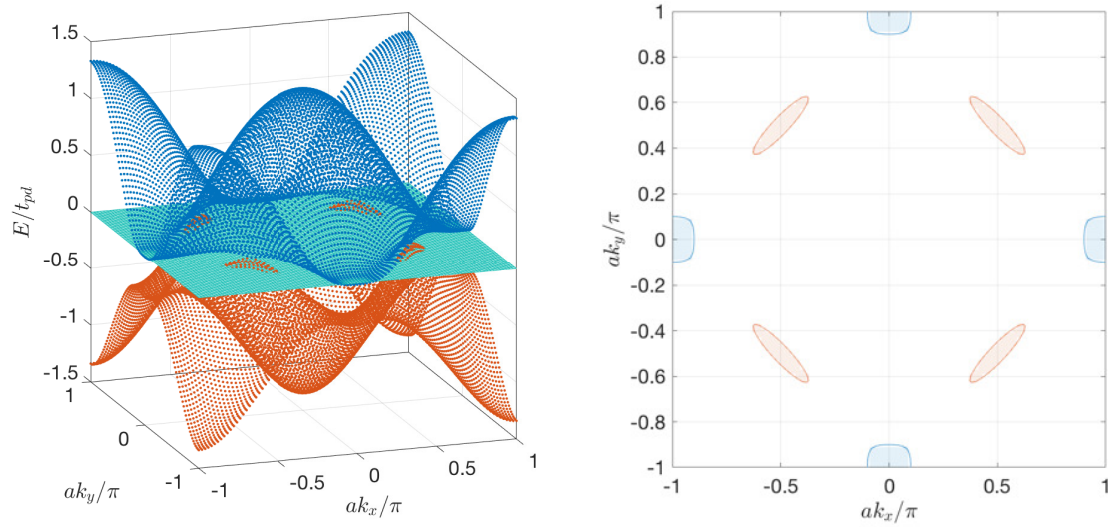

(a) (b)

Figure 4.6: (a) Zoom on the highest energy bands of the dispersion relation over the full Brillouin zone for the mean-field πLC Hamiltonian as investigated by Bulut *et al.* [7] ($\phi = 1$) under a typical parameter set. The green plane is at the Fermi energy. (b) Resulting Fermi surface with hole and electron pockets shown in orange and blue respectively.

4.3.1. Numerical Evaluatation

It is possible to evaluate numerically the Berry phase accumulated by an electron orbiting a hole pocket. The method is straightforward: first, the Hamiltonian in momentum space in its matrix form is diagonalized numerically on a discrete grid of points; then, the Berry curvature is calculated at all points using (2.13); finally, the Berry phase is evaluated by integrating over the area of the hole pocket which is enclosed by the electron's orbit as in (2.8). This approach is more straightforward numerically than calculating the line integral of the Berry vector potential given in (2.5) since there is no derivative of eigenstates involved.

Special considerations must be taken in the presence of a Dirac point because numerical methods do not adequately work at discontinuous points. In the case of a two-level system in 2D, we have seen in section 2.5 that a mass term must be added to the Hamiltonian in order to evaluate the Berry phase. Given a small finite value, the mass term provides a way to approximate the Dirac delta function located at the Dirac points in the Berry curvature. In such a way, numerical methods can be used to approximate the Berry phase without any problem. In order to make this precise, the mass term should be small enough to make the delta function's weight negligible outside the area of integration whereas the grid resolution must be taken high enough to approximate around the peak accurately.

In our case, adding the mass term to evaluate the Berry phase accumulated by an electron orbiting a hole pocket in one of the two highest energy bands is done by

$$\boldsymbol{H}_U(\boldsymbol{k}) \to \boldsymbol{H}_U(\boldsymbol{k}) + \alpha\xi\boldsymbol{\sigma}^1\,, \tag{4.21}$$

for small mass $\xi > 0$ and for α a unitary dimensionful constant carrying units of energy times length. Regarding the full mean-field Hamiltonian, it is equivalent to having

$$\begin{aligned}\boldsymbol{H}_{MF}(\boldsymbol{k}) &\to \boldsymbol{H}_{MF}(\boldsymbol{k}) + \alpha\xi\left[|+_\uparrow(\boldsymbol{k})\rangle\langle+_\downarrow(\boldsymbol{k})| + \{|+_\uparrow(\boldsymbol{k})\rangle\langle+_\downarrow(\boldsymbol{k})|\}^\dagger\right] \\ &= \boldsymbol{H}_{MF}(\boldsymbol{k}) + \alpha\xi\begin{bmatrix}\boldsymbol{0} & |+(\boldsymbol{k})\rangle\langle+(\boldsymbol{k}+\boldsymbol{Q})| \\ \{|+(\boldsymbol{k})\rangle\langle+(\boldsymbol{k}+\boldsymbol{Q})|\}^\dagger & \boldsymbol{0}\end{bmatrix}.\end{aligned} \tag{4.22}$$

As pointed out above, the mass term needs to be appropriately chosen. Recall from (2.39) that for a simple linear dispersion, a fraction $\{1+[\rho/\xi]^2\}^{-\frac{1}{2}}$ of the delta function's weight is lost outside of a radius ρ around the Dirac point. Hence, ρ and ξ must be set such that

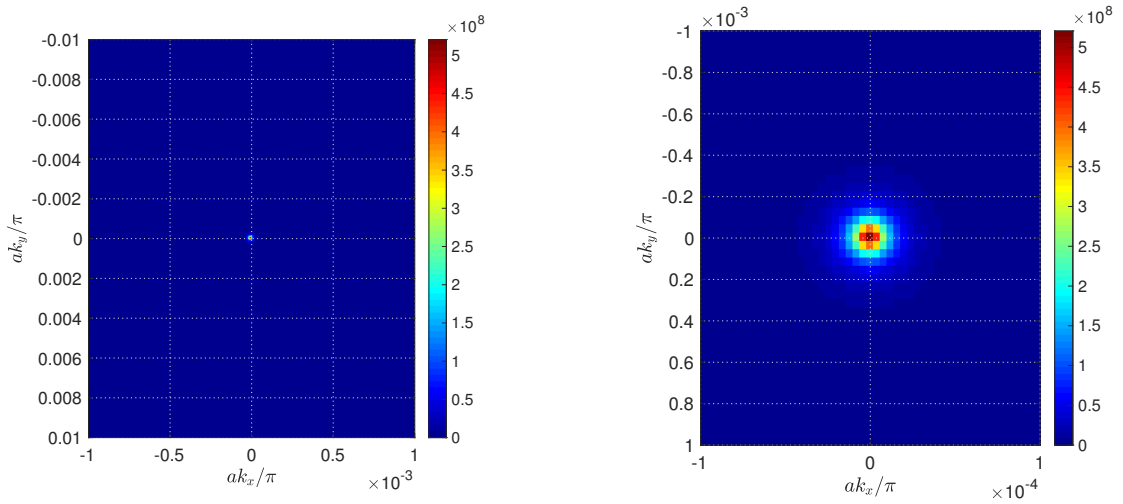

Figure 4.7: (a) Magnitude of the Berry curvature in units of $[a/\pi]^2$ close to a degeneracy point for the mean-field πLC Hamiltonian as investigated by Bulut *et al.* [7] ($\phi = 1$) under a typical parameter set. Similar results are obtained for $\phi = -1$. The momentum space has been translated to the degeneracy point $\left(\frac{\pi}{2a}, \frac{\pi}{2a}\right)$ and rotated by $\pi/4$ clockwise, the grid spacing is $4 \cdot 10^{-6}\,[a/\pi]^{-1}$ in the k_x-direction and $4 \cdot 10^{-5}\,[a/\pi]^{-1}$ in the k_y-direction, and the mass term $\xi = 1 \cdot 10^{-5}\,[a/\pi]^{-1}$. (b) Zoom on the plot.

ρ/ξ is big enough. In particular, about 1% of the delta function's weight is lost when taking $\rho/\xi = 100$. For a more general dispersion, more can be lost through the correction to the solid angle found in (2.31c), but we can assume this to be negligible because it is of order $\lambda \ll 1$ under a typical parameter set. Additionally, asymmetry in the rate of growth of the gap needs to be considered when choosing the mass term and the grid.

It should be noted that the Berry phase accumulated by an electron orbiting a hole pocket will be equal with opposite signs in the two highest energy bands. Moreover, it should also give the same value around every hole pocket with alternating signs as found in (4.20). This is in line with the fact that Dirac points come in pairs of opposite topological charge [54]. Therefore, it is enough to merely compute the Berry phase of the hole pocket surrounding $\left(\frac{\pi}{2a}, \frac{\pi}{2a}\right)$ for an electron in the lowest of the two highest energy bands.

The desired Berry phase can be evaluated by taking a few things into considerations specific to the mean-field πLC Hamiltonian under a typical parameter set. It can be seen numerically that the distance between the Dirac point and the boundary of the surrounding hole pocket ranges from approximately $0.025\,[a/\pi]^{-1}$ to $0.16\,[a/\pi]^{-1}$ for both current patterns. To make the calculation more efficient, the elongated shape of the hole pocket and

ϕ	$+1$	-1
$\gamma_-(C)/\pi$	99.1%	98.9%

Table 4.1: Berry phase for the counterclockwise orbit around the hole pocket surrounding $\left(\frac{\pi}{2a}, \frac{\pi}{2a}\right)$ in percentage of π of the lowest of the two highest energy bands for the mean-field πLC Hamiltonian with $\phi = \pm 1$ under a typical parameter set.

its positioning need to be taken into account. Thus, the momentum space is translated such that the origin corresponds to the degeneracy point considered, and it is then rotated clockwise by $\pi/4$. Furthermore, a rectangular grid centered at the origin of this transformed momentum space is taken with the horizontal 10 times smaller than the vertical. The same number of discrete points is taken horizontally and vertically. Specifically, the vertical side is set to have a length of $2 \cdot 10^{-2} \, [a/\pi]^{-1}$ with a grid spacing of $4 \cdot 10^{-5} \, [a/\pi]^{-1}$ along this direction. Finally, a mass term of $\xi = 1 \cdot 10^{-5} \, [a/\pi]^{-1}$ is chosen.

For both possible current patterns, a Berry phase approximately equal to π is obtained, in accordance with (4.20). The results are listed in table 4.2 and are all within expectations: almost equal to π, but not exactly because of the delta function's weight that is lost outside of the grid. No specific uncertainty on the Berry phase can be derived because of the nature of the approximation leading to unknown discretization errors. On the one hand, the contribution from discretizing the grid is assumed to be negligible because of the high grid resolution. On the other hand, the delta function's weight loss can be approximated to be around 1% by taking $\rho/\xi \approx 100$.

The above analysis of the semi-classical electron orbits does not take into account the effect of strong magnetic fields as used in quantum oscillations experiments. As such, the mean-field πLC Hamiltonian derived and investigated in this section could turn out to be invalid if magnetic suppression occurs. Still, it has been shown in mean-field-theoretic studies that the gap is insensitive to strong magnetic fields when the gap amplitude is sufficiently large in the non-magnetic regime [31]. This supports the assumption of a constant gap amplitude under any magnetic field that can be attained in laboratories.

To conclude, the results obtained so far lead one to believe that the πLC state is inconsistent with quantum oscillations data: an electron orbiting the Fermi surface acquires a nonzero Berry phase, in contradiction with recent experiments.

4.4. Quantum Treatment of the Magnetic Field through Peierls Substitution

A different method which does not rely on the semiclassical approach can be used to derive the Landau-like quantization relation. Known as the Peierls substitution, this particular approach allows us to incorporate an external magnetic field in a Bloch electron problem.

In quantum mechanics, an external magnetic field is typically introduced in equations by redefining the canonical momentum of a particle in terms of the magnetic vector potential $\boldsymbol{A}(\boldsymbol{r})$ in function of position $\boldsymbol{r}$ [48, Appendix E]:

$$\boldsymbol{p} \to \boldsymbol{p} - q\boldsymbol{A}(\boldsymbol{r})\,, \tag{4.23}$$

where q is the particle's charge. However, the energy eigenstates of electrons in a crystal lattice are no longer the usual Bloch states, but *modified* Bloch states instead as the initial discrete translational invariance of the Hamiltonian is now broken [27, and therein].

When the vector potential varies slowly over a lattice cell, the effect of the transformation done in (4.23) is to add a phase factor dependent on the vector potential to the hopping terms of the Hamiltonian [14]:

$$\hat{c}_{\boldsymbol{j}}^{\dagger}\hat{c}_{\boldsymbol{i}} \to \exp\left[i2\pi\frac{q}{h}\int_{\boldsymbol{R_i}}^{\boldsymbol{R_j}} \boldsymbol{A}(\boldsymbol{r})\cdot d\boldsymbol{r}\right]\hat{c}_{\boldsymbol{j}}^{\dagger}\hat{c}_{\boldsymbol{i}}\,, \tag{4.24}$$

where the path of the integral is by convention the shortest path from $\boldsymbol{R_i}$ to $\boldsymbol{R_j}$. This result can easily be derived from the path-integral formulation of quantum mechanics [48, Section 14.1]: as the classical action changes through the redefinition of the canonical momentum, the amplitude of a path gets a phase factor from the line integral over the path.

According to the justification found at the end of section 4.3.1, the gap amplitude is assumed to be approximately constant over the range of magnetic field magnitudes relevant to quantum oscillation experiments which are considered in this section. In such a way, all of the terms in the mean-field πLC Hamiltonian are assumed to transform following (4.24) under a typical parameter set.

Fortunately, the mean-field πLC Hamiltonian can be diagonalized for the specific magnetic fields which make the modified hopping terms share the same periodicity. Under such fields, a *magnetic* cell is defined. As derived in appendix H, the strength of an external constant magnetic field $\boldsymbol{B} = B\hat{\boldsymbol{z}}$ perpendicular to the CuO_2 plane which would allow di-

agonalization of our model is related to the dimensionless constant $\chi = eBa^2/[2h]$. Notice that $\chi = \Phi/\Phi_0$ for $\Phi = Ba^2/4$ the magnetic flux through one unit cell and $\Phi_0 = h/[2e]$ the magnetic flux quantum. By taking $a = 3.9\,\text{Å}$, the strength of the magnetic field is $B \approx 5.4\chi \cdot 10^4\,T$ in terms of χ. In any case, the Hamiltonian can be diagonalized by transforming to momentum space *specifically* when χ is a rational number. If we let $\chi = p/q$ be an irreducible fraction where $p \in \mathbb{Z}$ and $q \in \mathbb{N}$, the magnetic cell is composed of $2q$ unit cells in one of the diagonal directions as shown in figure 4.8. Therefore, a magnetic cell of many unit cells is required in order to have a magnetic field strength equivalent to what is found in experiments.

Rotating the system by $\pi/4$ clockwise like in section 4.3.1 leads to magnetic cells elongated in the y-direction. Furthermore, the magnetic Brillouin zone BZ_q associated with a system having $\chi = p/q$ is the rectangle $\frac{1}{a}[-\pi, \pi] \times \frac{1}{aq}[-\pi, \pi]$. A few factors need to be taken into consideration when diagonalizing the Hamiltonian on a discrete grid in momentum space. First, the number of grid points in the x-direction has to be q times greater than in the y-direction in order to have a square grid in momentum space. However, it is computationally expensive to take such a grid because of the increasing number of points as q gets large. On top of this, the mean-field πLC Hamiltonian matrix is a $6q \times 6q$ matrix and thus takes longer to diagonalize at any point as q increases. Thankfully, taking a low-resolution rectangular grid is enough in flat-level regimes [29], which we are solely concerned with.

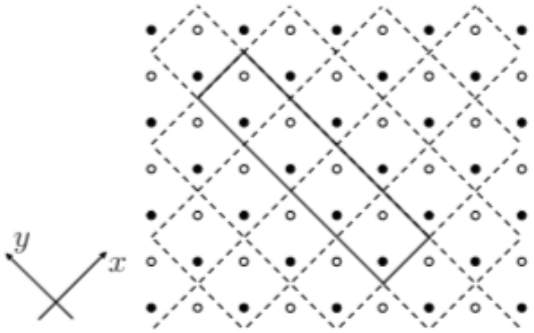

Figure 4.8: Different types of cells for the πLC state. The full and empty circles denote CuO_2 unit cells as found in figure 4.3 having opposite directional hopping due to $\boldsymbol{Q}$. The dashed lines determine the current cells of the system, corresponding to the true unit cells once the direction of the current is taken into account. The solid lines encompass a magnetic unit cell of $2q$ unit cells equivalent to q current cells with $q = 4$ in this case. Reproduced from [29].

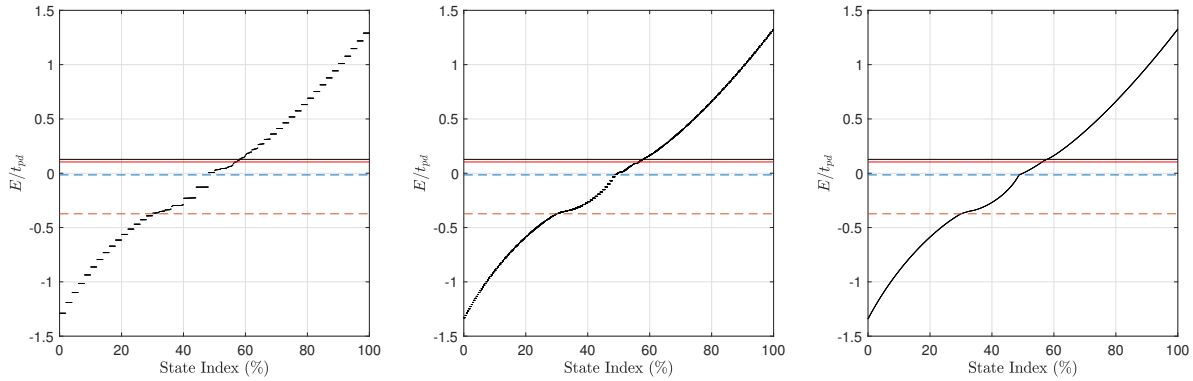

(a) $\chi = 1/100$ (b) $\chi = 1/500$ (c) $\chi = 0$

Figure 4.9: Energy distribution given by the Peierls substitution for the mean-field πLC Hamiltonian as investigated by Bulut *et al.* [7] ($\phi = 1$) under a typical parameter set for different values of χ on a 3×3 discrete grid over the magnetic Brillouin zone. Similar results are obtained for $\phi = -1$. The dashed orange and blue lines denote the energy at which hole and electron pockets appear respectively while the solid black horizontal line denotes where they both disappear. The solid red line denotes the energy at which the area of the hole pockets goes to zero, or in other words where the two bands meet.

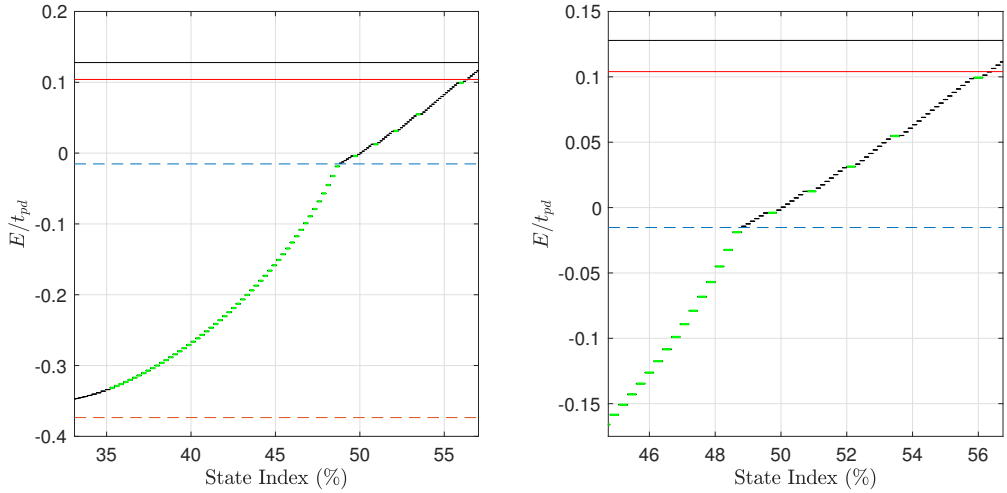

(a) (b)

Figure 4.10: Zoom on the energy distribution given by the Peierls substitution for the mean-field πLC Hamiltonian as investigated by Bulut *et al.* [7] ($\phi = 1$) under a typical parameter set for $\chi = 1/1500$, corresponding to $B \approx 36\,T$, on a 3×3 discrete grid over BZ_{1500}. Similar results are obtained for $\phi = -1$. The dashed orange and blue lines denote the energy at which hole and electron pockets appear respectively while the solid black horizontal line denotes where they both disappear. The solid red line denotes the energy at which the area of the hole pockets goes to zero, or in other words where the two bands meet. The green flat levels are those of the lowest of the two highest energy bands in the range where hole pockets are formed by this band.

Examples of resulting energy distributions where all states within BZ_q are sorted by energy for different $\chi = p/q$ are shown in figure 4.9. It mainly consists of flat levels except at energies where there are changes in the Fermi surface topology. More specifically, those changes occur at the minimum and maximum energies attained by the two highest energy bands in the non-magnetic regime along the border of the reduced Brillouin zone. Note that the density of flat levels — and hence their total number — increases with q.

On the one hand, there is only a small overlap between the energy distribution of the lower and upper electronic bands. In particular, most of the energy range where the lower band forms the hole pockets is not overlapped with any other energy state, and the flat levels from this band are clearly visible. Even where there *is* an overlap, the flat levels of this particular band are distinguishable for high enough q because of their distinct size, as seen in figure 4.10 (b). On the other hand, the energy range where the upper band forms the hole pockets is completely overlapped with the one where the electron pockets are formed. The flat levels from this electronic band for the hole pockets are thus impossible to distinguish.

Accordingly, it is then possible to extract the frequency and the phase of the quantum oscillations associated with the energy levels for any allowed magnetic field through the Onsager's relation and the Lifshitz-Onsager quantization rule respectively. In particular, the former is obtained by evaluating the area enclosed by the contour around a single hole pocket in momentum space at the energy level and using (3.16) while the latter is directly connected to the relation between the numbering of the allowed energy levels and the magnetic field as $|\boldsymbol{B}| \to \infty$ through (3.17). This analysis is explicitely found in the next section.

4.5. Comparison of the Semiclassical Approach with the Peierls Substitution

As a test of validity, the semiclassical approach can be compared to the Peierls substitution method. We begin by assuming the validity of the results obtained in section 4.3, specifically that the Berry phase acquired by an electron orbiting a hole pocket corresponding to a contour C in momentum space is equal to $\pm\pi$ where the sign depends on the contour and on the electronic band. Note that there is always a contour with Berry phase equal to $+\pi$ at any energy in the range of interest. Hence, (3.15) implies for the allowed levels that

$$\frac{l_B^2}{2\pi} A(C_n) = n\,, \tag{4.25}$$

where $A(C_n)$ is the area enclosed by C_n the contour of level $n \in \mathbb{N}^0$ in momentum space. Recall that $l_B^2 = \hbar/[eB]$ while $\chi = eBa^2/[2h]$, leading to

$$\frac{1}{2\chi}\frac{A(C_n)}{[2\pi/a]^2} = n\,. \tag{4.26}$$

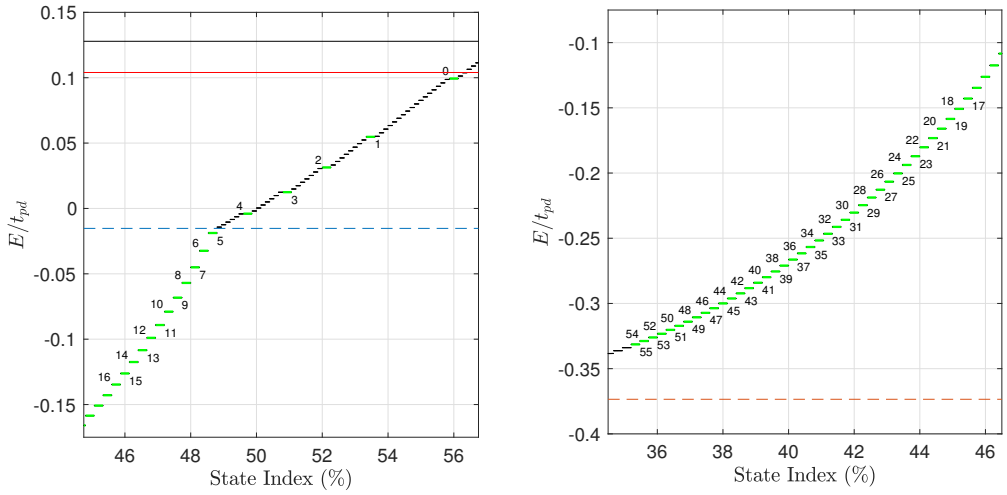

(a) (b)

Figure 4.11: Numbering of the energy levels of the lower band given by the Peierls substitution for the mean-field πLC Hamiltonian as investigated by Bulut *et al.* [7] ($\phi = 1$) under a typical parameter set when $\chi = 1/1500$, corresponding to $B \approx 36\,T$, on a 3×3 discrete grid over BZ_{1500}. Similar results are obtained for $\phi = -1$. The dashed orange and blue lines denote the energy at which hole and electron pockets appear respectively while the solid black horizontal line denotes where they both disappear. The solid red line denotes the energy at which the area of the hole pockets goes to zero, or in other words where the two bands meet. The green flat levels are those coming from the lower of the two highest energy bands in the range where hole pockets are formed by this band.

The last result is obtained through the semiclassical approach only. Comparing this approach with the Peierls substitution method is then possible by defining

$$n_{SC} \equiv \frac{1}{2\chi} \frac{A(C_{n_{PS}})}{[2\pi/a]^2} \,, \tag{4.27}$$

where $A(C_{n_{PS}})$ is the area of a hole pocket in momentum space under no external magnetic field at the energy level of n_{PS} obtained through the Peierls substitution. In such a way, similarity beween n_{SC} and n_{PS} over a range of values would signify that both approaches are consistent with one another and consequently confirm the prior assumption. Still, the mismatch between n_{SC} and n_{PS} can be quantified through $\delta \equiv n_{SC} - n_{PS}$. This value is in fact a measure of the difference from an exact Berry phase of π. More specifically, letting $\gamma_n(C) = \pi - 2\pi\delta$ in (3.15) yields

$$\frac{1}{2\chi} \frac{A(C_n)}{[2\pi/a]^2} = n + \delta \,, \tag{4.28}$$

in line with the definition of δ and (4.27). In such a way, δ or more explicitly $2\pi\delta$ may be used to obtain a bound on the Berry phase found from the mean-field πLC Hamiltonian.

The analysis was carried out for both possible current patterns under a typical parameter set with $\chi = 1/1500$, corresponding to $B \approx 36\,T$. The resulting energy distribution and the numbering of the energy levels for $\phi = 1$ can be found in figure 4.11, where similar results were obtained for $\phi = -1$. To derive n_{SC}, the area was calculated numerically at the energy level of n_{PS} for each level. The values of δ obtained are listed in table 4.2. In particular, zero is within error with high precision, and there is an excellent agreement between n_{SC} and n_{PS} over an extensive range of values. Additionally, the largest standard deviation on $2\pi\delta$ is 0.014π. It thus confirms that the Berry phase accumulated by an electron orbiting a hole pocket according to the mean-field πLC Hamiltonian equals to π with an uncertainty of order 0.01π.

ϕ	$+1$	-1
δ	-0.001 ± 0.004	0.002 ± 0.007

Table 4.2: Mean and standard deviation of δ for the lower of the two highest energy bands of the mean-field πLC Hamiltonian with $\phi = \pm 1$ under a typical parameter set.

4.6. Conclusions

To conclude, the electronic Berry phase was found to be π within error for an electron orbiting a hole pocket in the Brillouin zone of the mean-field πLC Hamiltonian under a typical parameter set, for all possible physical current patterns with 4-fold rotational symmetry. This was done in two different ways semiclassically: analytically and numerically. Additionally, a Peierls substitution analysis was used to compare with the semiclassical approach, thus confirming the Berry phase of $\pi \mod 2\pi$ and giving an uncertainty of order 0.01π on this value. These results contrast with the electronic Berry phase found to be $0 \mod 2\pi$ and $1.4 \mod 2\pi$ through the quantum oscillations experiments on hole-doped and electron-doped cuprates respectively.

In such a way, we conclude that the theoretical model of cuprates exhibiting circulating currents is inconsistent with present quantum oscillation data because of the discrepancy in the range of validity of their electronic Berry phases. Accordingly, this suggestion of a hidden order is unfit for cuprates.

Appendix A: The Adiabatic Theorem

This analysis is based on Sakurai [40, Supplement I]. Consider a time-dependent Hamiltonian $H(t)$ with $t \in \mathbb{R}_{\geq 0}$ that evolves slowly in time, where "slow" will be defined rigorously later in this analysis. Essentially, it means that the system has enough time to adapt before the conditions change significantly. The instantaneous energy eigenstates $\{|n(t)\rangle\}$ are orthonormal and satisfy

$$H(t)\,|n(t)\rangle = E_n(t)\,|n(t)\rangle\ , \tag{A.1}$$

where $E_n(t)$ is the energy corresponding to eigenstate $|n(t)\rangle$.

Assume nondegenerate eigenstates. We must solve the time-evolution equation

$$\frac{d}{dt}\,|\Psi(t)\rangle = -\frac{i}{\hbar}H(t)\,|\Psi(t)\rangle \tag{A.2}$$

in order to derive the time dependence of any state $|\Psi(t)\rangle$. To accomplish this, we have to express $|\Psi(t)\rangle$ as a superposition of the instantaneous eigenstates of $H(t)$. Accordingly,

$$|\Psi(t)\rangle = \sum_n c_n(t)e^{i\theta_n(t)}\,|n(t)\rangle\ , \tag{A.3}$$

where $c_n(t) \in \mathbb{C}$ and $\theta_n(t) \equiv -\frac{1}{\hbar}\int_0^t E_n(t')\,dt'$. The phase $e^{i\theta_n(t)}$ — the known time dependence and generalization of the dynamical phase — is factored out explicitly to simplify the analysis. In such a way, the coefficients $c_n(t)$ hold the unknown time dependence.

Replacing $|\Psi(t)\rangle$ as expressed in (A.3) on the right-hand side of (A.2) gives

$$\begin{aligned} -\frac{i}{\hbar}H(t)\,|\Psi(t)\rangle &= -\frac{i}{\hbar}H(t)\left[\sum_n c_n(t)e^{i\theta_n(t)}\,|n(t)\rangle\right] \\ &= \sum_n -\frac{i}{\hbar}c_n(t)e^{i\theta_n(t)}E_n(t)\,|n(t)\rangle\ , \end{aligned} \tag{A.4}$$

while it gives on the left-hand side

$$\begin{aligned} \frac{d}{dt}\,|\Psi(t)\rangle &= \frac{d}{dt}\left[\sum_n c_n(t)e^{i\theta_n(t)}\,|n(t)\rangle\right] \\ &= \sum_n e^{i\theta_n(t)}\left[\dot{c}_n(t)\,|n(t)\rangle - \frac{i}{\hbar}c_n(t)E_n(t)\,|n(t)\rangle + c_n(t)\frac{d}{dt}\,|n(t)\rangle\right]\ , \end{aligned} \tag{A.5}$$

as $\dot{\theta}_n(t) = -\frac{1}{\hbar}E_n(t)$. By combining (A.4) and (A.5), it should be clear that

$$0 = \sum_n e^{i\theta_n(t)} \left[\dot{c}_n(t) \left| n(t) \right\rangle + c_n(t) \frac{d}{dt} \left| n(t) \right\rangle \right] . \tag{A.6}$$

By then taking the inner product with $\langle m(t)|$ from the left,

$$0 = e^{i\theta_m(t)} \dot{c}_m(t) + \sum_n e^{i\theta_n(t)} c_n(t) \left\langle m(t) \right| \frac{d}{dt} \left| n(t) \right\rangle . \tag{A.7}$$

By rearranging the terms, we end up with a differential equation for the coefficients:

$$\dot{c}_m(t) = -\sum_n e^{i[\theta_n(t) - \theta_m(t)]} c_n(t) \left\langle m(t) \right| \frac{d}{dt} \left| n(t) \right\rangle . \tag{A.8}$$

Here, we need to take into account that $\frac{d}{dt}\left|n(t)\right\rangle$ will be different depending on the phase we choose for $\left|n(t)\right\rangle$ as t changes. Nevertheless, the final result should be invariant of this phase. Hence, it can be assume that the phase of $\left|n(t)\right\rangle$ is such that $\frac{d}{dt}\left|n(t)\right\rangle$ is well behaved at any time t. Note that by orthogonality of $\{\left|n(t)\right\rangle\}$,

$$\begin{aligned} 0 &= \frac{d}{dt} \left(\langle m(t) | m(t) \rangle \right) \\ &= \left\langle m(t) \right| \frac{d}{dt} \left| m(t) \right\rangle + \left[\frac{d}{dx} \left\langle m(t) \right| \right] \left| m(t) \right\rangle \\ &= 2 \operatorname{Re} \left(\left\langle m(t) \right| \frac{d}{dt} \left| m(t) \right\rangle \right) . \end{aligned} \tag{A.9}$$

Consequently, $\left\langle m(t) \right| \frac{d}{dt} \left| m(t) \right\rangle$ must be purely imaginary.

Differentiating the instantaneous Schrödinger equation (A.1) with time and taking the inner product with $\langle m(t)| \neq \langle n(t)|$ from the left gives

$$\begin{aligned} \left\langle m(t) \right| \left[\dot{H}(t) \left| n(t) \right\rangle + H(t) \frac{d}{dt} \left| n(t) \right\rangle \right] &= \left\langle m(t) \right| \left[\dot{E}_n(t) \left| n(t) \right\rangle + E_n(t) \frac{d}{dt} \left| n(t) \right\rangle \right] \\ \left\langle m(t) \right| \dot{H}(t) \left| n(t) \right\rangle + E_m(t) \left\langle m(t) \right| \frac{d}{dt} \left| n(t) \right\rangle &= E_n(t) \left\langle m(t) \right| \frac{d}{dt} \left| n(t) \right\rangle , \end{aligned} \tag{A.10}$$

which yields after rearranging the terms

$$\left\langle m(t) \right| \frac{d}{dt} \left| n(t) \right\rangle = \frac{\left\langle m(t) \right| \dot{H}(t) \left| n(t) \right\rangle}{E_n(t) - E_m(t)} . \tag{A.11}$$

In fact, (A.9) and (A.11) can easily be generalized to any non-degenerate orthogonal set and for the derivative with respect to any variable by going through the exact same steps taken.

Making use of the last equation, $\dot{c}_m(t)$ can be expressed as

$$\dot{c}_m(t) = -c_m(t) \langle m(t)| \frac{d}{dt} |m(t)\rangle - \sum_{n \neq m} e^{i[\theta_n(t) - \theta_m(t)]} c_n(t) \frac{\langle m(t)| \dot{H}(t) |n(t)\rangle}{E_n(t) - E_m(t)} . \tag{A.12}$$

Here is where the assumption that $H(t)$ evolves slowly with time takes its meaning. Indeed, we make here the assumption that at any time t and for all m

$$\max_{n \neq m} \left| \frac{\langle m(t)| \dot{H}(t) |n(t)\rangle}{E_n(t) - E_m(t)} \right| \ll \left| \langle m(t)| \frac{d}{dt} |m(t)\rangle \right| . \tag{A.13}$$

In other words, the mixed terms of $\dot{H}(t)$ which are responsible for the mixing between energy eigenstates with time are negligible. Hence, changes in the Hamiltonian occur slowly enough such that there is no mixing of the energy eigenstates. As a result, a state starting in an energy eigenstate stays the same up to a phase at all time and the second term on the right-hand side of (A.12) can be dropped.

Solving the equation of motion of the coefficients in the adiabatic regime yields

$$c_n(t) = c_n(0) e^{i\gamma_n(t)} , \tag{A.14}$$

where $\gamma_n(t)$ is a real function defined as

$$\gamma_n(t) \equiv i \int_0^t \langle n(t')| \frac{d}{dt'} |n(t')\rangle \, dt' . \tag{A.15}$$

Ultimately, a state will evolve in time according to

$$|\Psi(t)\rangle = \sum_n c_n(0) e^{i\gamma_n(t)} e^{i\theta_n(t)} |n(t)\rangle . \tag{A.16}$$

While the dynamical phase is indeed a part of the total phase as expected, the less intuitive phase evolution is given by $\gamma_n(t)$, known as the Berry phase.

Appendix B: Time-Independent Perturbation Theory

Most problems in quantum mechanics are impossible to solve exactly. However, there are powerful approximation methods that can reduce considerably the complexity of a problem. Those methods can also provide us with a better undertanding of the underlying processes by putting the focus on what is important.

One of the most important approximation methods is the time-independent perturbation theory. It was first presented in 1926 by Erwin Schrödinger [42] who was referring to Lord Rayleigh [37] — hence it is also known as the Rayleigh-Schrödinger perturbation theory. The basic idea is to describe a complicated system using a simple one. We will base our description of this method on Sakurai [40, Sections 5.1-5.2].

B.1. For a State

We start by considering a time-independent Hamiltonian H which can be expressed as

$$H = H_0 + \lambda V \,, \tag{B.1}$$

for which it is assumed that the exact energy eigenvalues $E_n^{(0)}$ of H_0 and corresponding eigenstates $|n^{(0)}\rangle$ are known:

$$H_0 \, |n^{(0)}\rangle = E_n^{(0)} \, |n^{(0)}\rangle \ . \tag{B.2}$$

The set $\{|n^{(0)}\rangle\}$ must satisfy the closure relation $1 = \sum_n |n^{(0)}\rangle \, \langle n^{(0)}|$ and we assume that the eigenvalues $E_n^{(0)}$ are nondegenerate. Additionally, note that λ is a continuous parameter that keeps track of the strength of the perturbation V.

We are then interested in solving

$$[H_0 + \lambda V] \, |n\rangle = E_n \, |n\rangle \ , \tag{B.3}$$

where the eigenvalues E_n and eigenstates $|n\rangle$ are functions of λ. As λ changes from zero, the energy eigenvalue E_n also changes from $E_n^{(0)}$. This energy shift as a function depending on λ can be defined as

$$\Delta_n \equiv E_n - E_n^{(0)} \, . \tag{B.4}$$

In particular, it means that $\Delta_n = 0$ when $\lambda = 0$. Consequently, (B.3) can be rewritten as

$$[E_n^{(0)} - H_0]\,|n\rangle = [\lambda V - \Delta_n]\,|n\rangle\ . \tag{B.5}$$

We cannot invert the operator $E_n^{(0)} - H_0$ because $1/[E_n^{(0)} - H_0]$ is ill defined when acting on $|n^{(0)}\rangle$. Nevertheless, by defining the complementary projection operator

$$\phi_n \equiv 1 - |n^{(0)}\rangle\,\langle n^{(0)}| = \sum_{m\neq n} |m^{(0)}\rangle\,\langle m^{(0)}|\ , \tag{B.6}$$

we see that $1/[E_n^{(0)} - H_0]$ is well defined when multiplied by ϕ_n on the right:

$$\frac{1}{E_n^{(0)} - H_0}\phi_n = \sum_{m\neq n} \frac{1}{E_n^{(0)} - E_m^{(0)}}\,|m^{(0)}\rangle\,\langle m^{(0)}|\ . \tag{B.7}$$

Clearly, it follows that

$$\frac{1}{E_n^{(0)} - H_0}\phi_n = \phi_n\frac{1}{E_n^{(0)} - H_0} = \phi_n\frac{1}{E_n^{(0)} - H_0}\phi_n \equiv \frac{\phi_n}{E_n^{(0)} - H_0}\,. \tag{B.8}$$

Notice that $[\lambda V - \Delta_n]\,|n\rangle$ has no component along $|n^{(0)}\rangle$ since multiplying (B.5) on the left by $\langle n^{(0)}|$ yields

$$\langle n^{(0)}|\,[\lambda V - \Delta_n]\,|n\rangle = 0\,. \tag{B.9}$$

Hence, it satisfies

$$[\lambda V - \Delta_n]\,|n\rangle = \phi_n[\lambda V - \Delta_n]\,|n\rangle\ . \tag{B.10}$$

That being so, simply multiplying (B.5) by $1/[E_n^{(0)} - H_0]$ would lead to

$$|n\rangle = \frac{\phi_n}{E_n^{(0)} - H_0}[\lambda V - \Delta_n]\,|n\rangle\ . \tag{B.11}$$

However, this equation is *not* right because we do not obtain that $|n\rangle = |n^{(0)}\rangle$ when $\lambda = 0$. To solve this problem, notice that (B.5) does not change upon adding to $|n\rangle$ a term proportional to $|n^{(0)}\rangle$. Thus, the left-hand side of (B.11) is in fact $\phi_n\,|n\rangle$ and it is then possible to add to $|n\rangle$ a term equal to $|n^{(0)}\rangle$ — but keep note that $|n\rangle$ will not be normalized in this case.

Therefore,

$$|n\rangle = |n^{(0)}\rangle + \frac{\phi_n}{E_n^{(0)} - H_0}[\lambda V - \Delta_n]\,|n\rangle\ . \tag{B.12}$$

Furthermore, rearranging (B.9) now yields

$$\Delta_n = \lambda\,\langle n^{(0)}|\,V\,|n\rangle\ . \tag{B.13}$$

The state $|n\rangle$ can then be renormalized by defining the state

$$|n\rangle_N \equiv Z_n^{\frac{1}{2}}\,|n\rangle\ , \tag{B.14}$$

for a constant Z_n such that $Z_n^{-1} = \langle n|n\rangle$. As $Z_n^{\frac{1}{2}} = \langle n^{(0)}|n\rangle_N$, its value can be understood as the probability of finding the perturbed state in its corresponding unperturbed state.

Although very simple expressions involving $|n\rangle$ have been found, solving exactly (B.12) to obtain $|n\rangle$ may be difficult or even impossible. The strategy is then to expand Δ_n and $|n\rangle$ in powers of λ and to match the coefficients of same power. In order to do so, we have to assume the analyticity of both E_n and $|n\rangle$ as functions of λ in a complex λ-plane around zero. Accordingly, let

$$\Delta_n = \lambda\Delta_n^{(1)} + \lambda^2\Delta_n^{(2)} + \cdots = \sum_{k=1}^{\infty}\lambda^k\Delta_n^{(k)}\,, \tag{B.15a}$$

$$|n\rangle = |n^{(0)}\rangle + \lambda\,|n^{(1)}\rangle + \cdots = \sum_{k=0}^{\infty}\lambda^k\,|n^{(k)}\rangle\ . \tag{B.15b}$$

In such a way, for $k \in \mathbb{N}$

$$\Delta_n^{(k+1)} = \langle n^{(0)}|\,V\,|n^{(k)}\rangle\ , \tag{B.16a}$$

$$|n^{(k+1)}\rangle = \frac{\phi_n}{E_n^{(0)} - H_0}[V\,|n^{(k)}\rangle - \sum_{k'=0}^{k}\Delta_n^{(k-k'+1)}\,|n^{(k')}\rangle]\,, \tag{B.16b}$$

along with

$$Z_n^{-1} = 1 + \sum_{k=2}^{\infty}\lambda^k \cdot \sum_{k'=1}^{k-1}\langle n^{(k')}|n^{(k-k')}\rangle\ . \tag{B.17}$$

Higher order terms are negligible when $\left|\frac{\langle m^{(0)}|\lambda V|n^{(0)}\rangle}{E_n^{(0)} - E_m^{(0)}}\right| \ll 1$ for all $m \neq n$. In this case, we

can focus on first order where

$$\Delta_n^{(1)} = \langle n^{(0)}| V |n^{(0)}\rangle \ , \tag{B.18a}$$

$$|n^{(1)}\rangle = \sum_{m\neq n} \frac{\langle m^{(0)}| V |n^{(0)}\rangle}{E_n^{(0)} - E_m^{(0)}} |m^{(0)}\rangle \ , \tag{B.18b}$$

while

$$Z_n = 1 - \lambda^2 \sum_{m\neq n} \left| \frac{\langle m^{(0)}| V |n^{(0)}\rangle}{E_n^{(0)} - E_m^{(0)}} \right|^2 + \mathcal{O}(\lambda^3) \, . \tag{B.19}$$

In the more general case that $\lambda V \to \lambda V + F(\lambda)$ for some $F(\lambda)$ that can be expanded in powers of λ and such that $F(\lambda) = \mathcal{O}(\lambda^2)$, the strategy is the same and we have that (B.18) remains invariant, i.e. only the first order perturbation to the Hamiltonian is needed to find the first order corrections.

B.2. For a Subspace

Instead of looking at the perturbation of a single unperturbed eigenstate, it can be interesting to look at the perturbation of a *subspace* of unperturbed eigenstates that is separated energically from the rest of the states.

Suppose that we are interested in a subspace M of unperturbed eigenstates which will be denoted by $\{|m^{(0)}\rangle\}$. Assume that there is an energy gap of at least ΔE between the subspace M and the rest of the Hilbert space and that ΔE is large enough where "enough" will be rigorously defined later on. As the perturbation changes from 0, the perturbed eigenstates which evolved from M will form a set $\{|l\rangle\}$ such that $|l\rangle \to |l^{(0)}\rangle$ as $\lambda \to 0$ where the set $\{|l^{(0)}\rangle\}$ spans M. Note that $\{|l^{(0)}\rangle\}$ need not to coincide with $\{|m^{(0)}\rangle\}$, but

$$|l^{(0)}\rangle = \sum_{m\in M} \langle m^{(0)}|l^{(0)}\rangle \, |m^{(0)}\rangle \ . \tag{B.20}$$

To approach this problem, let P_0 be a projection operator onto the subspace $\{|m^{(0)}\rangle\}$ and $P_1 \equiv 1 - P_0$ be the projection onto the remaining states of the Hilbert space. The

Schrödinger equation for the state $|l\rangle$ can then be rewritten as

$$\begin{aligned} 0 &= [E_l - H_0 - \lambda V]\,|l\rangle \\ &= [E_l - H_0 - \lambda V]P_0\,|l\rangle + [E_l - H_0 - \lambda V]P_1\,|l\rangle\ . \end{aligned} \tag{B.21}$$

We can then separate (B.21) into two equations by simply projecting by P_0 and by P_1 from the left:

$$[E_l - H_0 - \lambda P_0 V]P_0\,|l\rangle - \lambda P_0 V P_1\,|l\rangle = 0\,, \tag{B.22a}$$

$$-\lambda P_1 V P_0\,|l\rangle + [E_l - H_0 - \lambda P_1 V]P_1\,|l\rangle = 0\,. \tag{B.22b}$$

First, the assumption that the energy bands of subspace M are separated enough energically from the others means in particular that $P_1[E_l - H_0 - \lambda P_1 V P_1]$ is not singular in the P_1 subspace. In such a way, (B.22b) can be solved in this subspace and we have

$$P_1\,|l\rangle = \lambda \frac{P_1}{E_l - H_0 - \lambda V} V P_0\,|l\rangle\ . \tag{B.23}$$

By then substituting (B.23) in (B.22a) and letting $\Delta_l \equiv E_l - E_l^{(0)}$ where $E_l^{(0)} \equiv \langle l^{(0)}|\,H_0\,|l^{(0)}\rangle$,

$$\left[E_l^{(0)} - H_0 + \Delta_l - \lambda P_0 V P_0 - \lambda^2 P_0 V \frac{P_1}{E_l - H_0 - \lambda V} V P_0\right] P_0\,|l\rangle = 0\,. \tag{B.24}$$

Following the same logic as before, we can impose the normalization convention that $\langle l^{(0)}|l\rangle = 1$ so that by rearranging (B.21) and multiplying it on the left by $\langle l^{(0)}|$

$$\Delta_l = \lambda\,\langle l^{(0)}|\,V\,|l\rangle\ . \tag{B.25}$$

The state $|l\rangle$ can then be renormalized by defining the state

$$|l\rangle_N \equiv Z_l^{\frac{1}{2}}\,|l\rangle\ , \tag{B.26}$$

for a constant Z_l such that $Z_l^{-1} = \langle l|l\rangle$. As $Z_l^{\frac{1}{2}} = \langle l^{(0)}|l\rangle_N$, its value can be understood once again as the probability of finding the perturbed state in its corresponding unperturbed state.

Note that it is still not clear what $|l^{(0)}\rangle$ is explicitly in terms of $\{|m^{(0)}\rangle\}$. The previous strategy of expanding Δ_l and $|l\rangle$ in the powers of λ and matching the coefficients of same power will not allow us to solve the problem unless M is a degenerate subspace, i.e. when $E_m^{(0)} = E_M^{(0)}$ for all m for some $E_M^{(0)}$, as $[E_l^{(0)} - H_0]P_0 |l\rangle = 0$ in that case. Still, there is valuable information to be found in (B.23) and (B.24) when M is not a degenerate subspace.

Let H_0 and V be matrix operators sharing the same basis and let $\tilde{\lambda} \equiv \max_{i,j} |\lambda V_{ij}|/|\Delta E|$. Suppose that λV is such that $\tilde{\lambda} \ll 1$. Thus, $\langle l| P_1 |l\rangle \,/\, \langle l| P_0 |l\rangle = \mathcal{O}(\tilde{\lambda}) \ll 1$ from (B.23) and

$$E_l \cdot P_0 |l\rangle = P_0\{H_0 + \lambda V[1 + \mathcal{O}(\tilde{\lambda})]\}P_0 \cdot P_0 |l\rangle \approx P_0\{H_0 + \lambda V\}P_0 \cdot P_0 |l\rangle \ , \tag{B.27}$$

from (B.24) since $H_0 P_0 |l\rangle = [P_0 H_0 P_0]P_0 |l\rangle$. In particular, it implies that $|l\rangle \approx P_0 |l\rangle$ and that $|l\rangle$ approximately satisfies the Schrödinger equation of the perturbed Hamiltonian projected onto the subspace M. Hence, it means that we can effectively project the Hamiltonian onto the subspace M when investigating the perturbed eigenvalues and eigenstates from this subspace.

Appendix C: Absence of Berry Phase Correction Term in 2D

Recall that with $v(r,\theta) = \mathcal{O}(r)$ and $w(r,\theta) = \mathcal{O}(r)$ we had

$$f(r/\xi,\theta) = \frac{[1+w(r,\theta)][r/\xi]\,|\boldsymbol{\Theta}(\theta)|^{-1}}{\left\{[r/\xi]^2 + |\boldsymbol{\Theta}(\theta)|^{-2}\right\}^{\frac{3}{2}}}\,, \tag{C.1a}$$

$$\tilde{\Omega}(D) = \lim_{\xi\to 0}\iint\limits_{S} \frac{g(\theta)}{|\boldsymbol{\Theta}(\theta)|^2}\left[\left\{1+\frac{|r\boldsymbol{\Theta}(\theta)|^2\, v(r,\theta)}{|r\boldsymbol{\Theta}(\theta)|^2+\xi^2}\right\}^{-\frac{3}{2}} - 1\right] f(r/\xi,\theta)\, d[r/\xi]\, d\theta\,. \tag{C.1b}$$

Let $B_0 = \{(r,\theta)\in\mathbb{R}_{\geq 0}\times[0,2\pi)\,|\,|v(r,\theta)|<1\}$. Since $v(r,\theta)=\mathcal{O}(r)$ and by continuity of the function, there exists $\epsilon>0$ such that $(r,\theta)\in B_0$ for all $r\in[0,\epsilon)$ and θ. Hence, any $(r,\theta)\in S\backslash B_0$ has the property that $r>\epsilon$. Consequently, $\frac{|r\boldsymbol{\Theta}(\theta)|^2 v(r,\theta)}{|r\boldsymbol{\Theta}(\theta)|^2+\xi^2}<1$ for all $(r,\theta)\in B_0$ and

$$\begin{aligned}
&\iint\limits_{S\cap B_0} \frac{g(\theta)}{|\boldsymbol{\Theta}(\theta)|^2}\left[\left\{1+\frac{|r\boldsymbol{\Theta}(\theta)|^2\, v(r,\theta)}{|r\boldsymbol{\Theta}(\theta)|^2+\xi^2}\right\}^{-\frac{3}{2}} - 1\right] f(r/\xi,\theta)\, d[r/\xi]\, d\theta \\
&\quad= \sum_{k=1}^{\infty}\binom{-\frac{3}{2}}{k}\iint\limits_{S\cap B_0}\frac{g(\theta)}{|\boldsymbol{\Theta}(\theta)|^2}\left\{\frac{|r\boldsymbol{\Theta}(\theta)|^2\, v(r,\theta)}{|r\boldsymbol{\Theta}(\theta)|^2+\xi^2}\right\}^{k} f(r/\xi,\theta)\, d[r/\xi]\, d\theta \\
&\quad= \sum_{k=1}^{\infty}\binom{-\frac{3}{2}}{k}\iint\limits_{S\cap B_0}\frac{g(\theta)}{|\boldsymbol{\Theta}(\theta)|^3}\frac{[1+w(r,\theta)][r/\xi]^{2k+1} v^k(r,\theta)}{\left\{[r/\xi]^2+|\boldsymbol{\Theta}(\theta)|^{-2}\right\}^{k+\frac{3}{2}}}\, d[r/\xi]\, d\theta\,.
\end{aligned} \tag{C.2}$$

As $v(r,\theta)=\mathcal{O}(r)$, it implies that $v^k(r,\theta)$ is a sum of terms proportional to r^l with $l\geq k$. Additionally, $1+w(r,\theta)$ is a sum of terms proportional to r^m with $m\geq 0$. However, for any $l\geq k\geq 1$ and $m\geq 0$

$$\begin{aligned}
&\lim_{\xi\to 0}\iint\limits_{S\cap B_0}\frac{g(\theta)}{|\boldsymbol{\Theta}(\theta)|^3}\frac{r^m[r/\xi]^{2k+1}r^l}{\left\{[r/\xi]^2+|\boldsymbol{\Theta}(\theta)|^{-2}\right\}^{k+\frac{3}{2}}}\, d[r/\xi]\, d\theta \\
&\qquad= \lim_{\xi\to 0}\xi^{l+m}\iint\limits_{S\cap B_0}\frac{g(\theta)}{|\boldsymbol{\Theta}(\theta)|^3}\frac{[r/\xi]^{2k+l+m+1}}{\left\{[r/\xi]^2+|\boldsymbol{\Theta}(\theta)|^{-2}\right\}^{k+\frac{3}{2}}}\, d[r/\xi]\, d\theta \\
&\qquad= 0\,,
\end{aligned} \tag{C.3}$$

since the integral over r in the second line converges, but is multiplied by a stricly positive power of ξ which then goes to zero on the next step.

On top of this, we must obtain that

$$\lim_{\xi\to 0}\iint_{S\setminus B_0}\frac{g(\theta)}{|\boldsymbol{\Theta}(\theta)|^2}\left[\left\{1+\frac{|r\boldsymbol{\Theta}(\theta)|^2\,v(r,\theta)}{|r\boldsymbol{\Theta}(\theta)|^2+\xi^2}\right\}^{-\frac{3}{2}}-1\right]f(r/\xi,\theta)\,d[r/\xi]\,d\theta=0 \tag{C.4}$$

Note that $v(r,\theta)\neq -1$ as it would imply a second degeneracy point otherwise — which we assumed there is not. In such a way, $\left|\left\{1+\frac{|r\boldsymbol{\Theta}(\theta)|^2 v(r,\theta)}{|r\boldsymbol{\Theta}(\theta)|^2+\xi^2}\right\}^{-\frac{3}{2}}-1\right|<M$ for all $(r,\theta)\in S\setminus B_0$ for some $M\in[0,\infty)$. However, we have already proven in section 2.5 that

$$\lim_{\xi\to 0}\iint_{R}\frac{g(\theta)}{|\boldsymbol{\Theta}(\theta)|^2}f(r/\xi,\theta)\,d[r/\xi]\,d\theta=0 \tag{C.5}$$

for any set R such that $\mathbf{0}\notin R$. Thus, the integral in (C.4) must equal zero since $\mathbf{0}\in B_0$.

Therefore, by combining both results, one must come to the conclusion that $\tilde{\Omega}(D)=0$ as it was argued in section 2.5.

Appendix D: Analysis of the Kinetic Energy

Without loss of generality, let $\boldsymbol{H}_0(\boldsymbol{k}) \to \boldsymbol{H}_0(\boldsymbol{k}) - \epsilon_p \boldsymbol{I}$ so that $\epsilon_d \to \epsilon_d - \epsilon_p \equiv \Delta\epsilon$ and $\epsilon_p \to 0$. The energy eigenvalues of $\boldsymbol{H}_0(\boldsymbol{k})$ then satisfy the equation

$$[E_n(\boldsymbol{k}) - \Delta\epsilon][E_n^2(\boldsymbol{k}) - 16t_{pp}^2 s_x^2 s_y^2] - 4E_n(\boldsymbol{k})t_{pd}^2[s_x^2 + s_y^2] + 32t_{pd}^2 t_{pp} s_x^2 s_y^2 = 0\,. \tag{D.1}$$

The first thing to notice is that $E_n(\boldsymbol{k})$ is even with respect to the k_x-axis, the k_y-axis, and both the diagonal axes, and that it is periodic with a period of 2π. Although we cannot solve exactly for $E_n(\boldsymbol{k})$, finding the extrema of $E_n(\boldsymbol{k})$ is still possible and will give some intuition. To achieve this, we can take the gradient of (D.1) with respect to $\boldsymbol{k}$ and let $\nabla E_n(\boldsymbol{k}) \to 0$. It yields that the extrema of $E_n(\boldsymbol{k})$ are located at $\boldsymbol{k} = \pi\left(n^x,\ n^y\right)$ for $n^x, n^y \in \mathbb{Z}$.

Although this tells us where the extrema are and the energy at those points, it does not indicate what band they correspond to. To find this, we need to derive explicit formulas for $E_n(\boldsymbol{k})$ that can connect the extrema. It is enough to derive $E_n(\boldsymbol{k})$ for the two cases $k^y = 0$ and $k^y = k^x$ because of the symmetry between k^x and k^y in (D.1) and periodicity. When $k^y = 0$, the eigenvalues are given by the set $\{0, \frac{1}{2}[\Delta\epsilon \pm \{\Delta\epsilon^2 + 4t_{pd}^2 s_x^2\}^{\frac{1}{2}}]\}$ while when $k^y = k^x$ they are given by the set $\{4t_{pp}s_x^2, \frac{1}{2}[\Delta\epsilon - 4t_{pp}s_x^2 \pm \{[\Delta\epsilon + 4t_{pp}s_x^2]^2 + 32t_{pd}^2 s_x^2\}^{\frac{1}{2}}]\}$.

Under the condition that $\Delta\epsilon > -4t_{pp} > 0$ and $t_{pd} > 0$, there is an energy band that is separated from the other two bands. This band attains its minimum $\Delta\epsilon$ at the origin while the other two bands equal to 0 at the same point. More importantly, it never crosses any of the two lowest bands at any point because their maximum value is strictly less than $-4t_{pp}$. Hence, this energy band is higher in energy than any other band. In the particular case that $t_{pp} = -t_{pd}/2$ and $\Delta\epsilon < 4t_{pd}$ — which is satisfied under a typical parameter set of the cuprates — the maximum value attained by the two lower bands is 0. Hence, there is an energy gap of $\Delta\epsilon$ between the highest energy band and the rest.

Furthermore, it follows from everything above that $E_n(\boldsymbol{k} + \boldsymbol{Q}) = E_n(\boldsymbol{k})$ if and only if $\boldsymbol{k} \in \partial BZ'$ under a typical parameter set.

Although the system cannot be solved exactly in function of $\boldsymbol{k}$, it is possible to solve it at individual points. Points of particular interest are of the form $\boldsymbol{k}^* = \frac{\pi}{2a}\left(\sigma_x,\ \sigma_y\right)$ for

$\sigma_x, \sigma_y \in \{\pm 1\}$. By defining

$$\boldsymbol{J} \equiv \begin{bmatrix} 1 & 0 & 0 \\ 0 & \sigma_x & 0 \\ 0 & 0 & \sigma_y \end{bmatrix}, \tag{D.2}$$

we have at such points

$$\boldsymbol{J}\boldsymbol{H}_0(\boldsymbol{k}^*)\boldsymbol{J} = \begin{bmatrix} \Delta\epsilon & \sqrt{2}t_{pd} & -\sqrt{2}t_{pd} \\ \sqrt{2}t_{pd} & 0 & 2t_{pp} \\ -\sqrt{2}t_{pd} & 2t_{pp} & 0 \end{bmatrix}. \tag{D.3}$$

The eigenvalues are easy to find, especially considering that we have already obtained the characteristic equation (D.1). They are $E_\pm = \frac{1}{2}\left\{[\Delta\epsilon - 2t_{pp}] \pm \sqrt{[\Delta\epsilon + 2t_{pp}]^2 + 16t_{pd}^2}\right\}$ and $E_0 = 2t_{pp}$. The corresponding eigenstates are then

$$|n\rangle = \frac{c_n}{\sqrt{2}} \begin{bmatrix} \sqrt{2}a_n \\ 1 \\ (-1)^n \end{bmatrix}, \tag{D.4}$$

for $a_\pm \equiv [E_\pm + 2t_{pp}]/[2t_{pd}] = [2t_{pd}]/[E_\pm - \Delta\epsilon]$, $c_\pm \equiv 1/[1 + a_\pm]^{\frac{1}{2}}$, and $a_0 \equiv 0$, $c_0 \equiv 1$. Therefore, the eigenstates of $\boldsymbol{H}_0(\boldsymbol{k}^*)$ are $|n(\boldsymbol{k}^*)\rangle = \boldsymbol{J}\,|n\rangle$ with eigenvalues $E_n(\boldsymbol{k}^*) = E_n$.

Appendix E: Mean-Field Version of the Charge Order

First, the current operator $\hat{J}_{\boldsymbol{j}\beta,\boldsymbol{i}\alpha} = -it_{\boldsymbol{j}\beta,\boldsymbol{i}\alpha}[\hat{c}^{\dagger}_{\boldsymbol{j}\beta}\hat{c}_{\boldsymbol{i}\alpha} - \hat{c}^{\dagger}_{\boldsymbol{i}\alpha}\hat{c}_{\boldsymbol{j}\beta}]$ for the bond between $\boldsymbol{i}\alpha$ and $\boldsymbol{j}\beta$ satisfies the operator identity

$$2\hat{n}_{\boldsymbol{j}\beta}\hat{n}_{\boldsymbol{i}\alpha} = -\left[\frac{\hat{J}_{\boldsymbol{j}\beta,\boldsymbol{i}\alpha}}{t_{\boldsymbol{j}\beta,\boldsymbol{i}\alpha}}\right]^2 + \hat{n}_{\boldsymbol{i}\alpha} + \hat{n}_{\boldsymbol{j}\beta}\,, \tag{E.1}$$

for $\boldsymbol{i}\alpha$ different from $\boldsymbol{j}\beta$, which leads to

$$\tfrac{1}{2}\sum_{\langle \boldsymbol{i}\alpha,\boldsymbol{j}\beta\rangle} V_{\beta\alpha}\hat{n}_{\boldsymbol{j}\beta}\hat{n}_{\boldsymbol{i}\alpha} = \sum_{\boldsymbol{i}\alpha}\tilde{\epsilon}_{\alpha}\hat{n}_{\boldsymbol{i}\alpha} - \tfrac{1}{2}\sum_{\langle \boldsymbol{i}\alpha,\boldsymbol{j}\beta\rangle}\frac{V_{\beta\alpha}}{2t^2_{\boldsymbol{j}\beta,\boldsymbol{i}\alpha}}\hat{J}^2_{\boldsymbol{j}\beta,\boldsymbol{i}\alpha}\,, \tag{E.2}$$

for $\tilde{\epsilon}_d \equiv V_{pd} + 2V_{pp}$ and $\tilde{\epsilon}_p \equiv 2V_{pd}$. The current amplitudes $z_{\boldsymbol{j}\beta,\boldsymbol{i}\alpha} = \langle \hat{J}_{\boldsymbol{j}\beta,\boldsymbol{i}\alpha}\rangle$ are then used to decouple the interorbital interactions in mean-field:

$$\begin{aligned}
\tfrac{1}{2}\sum_{\langle \boldsymbol{i}\alpha\sigma,\boldsymbol{j}\beta\sigma'\rangle} V_{\beta\alpha}\hat{n}_{\boldsymbol{j}\beta\sigma'}\hat{n}_{\boldsymbol{i}\alpha\sigma} &\xrightarrow{MF} \sum_{\boldsymbol{i}\alpha}\tilde{\epsilon}_{\alpha}\hat{n}_{\boldsymbol{i}\alpha} - \tfrac{1}{2}\sum_{\langle \boldsymbol{i}\alpha,\boldsymbol{j}\beta\rangle}\frac{V_{\beta\alpha}z_{\boldsymbol{j}\beta,\boldsymbol{i}\alpha}}{t^2_{\boldsymbol{j}\beta,\boldsymbol{i}\alpha}}\hat{J}_{\boldsymbol{j}\beta,\boldsymbol{i}\alpha} \\
&= \sum_{\boldsymbol{i}\alpha}\tilde{\epsilon}_{\alpha}\hat{n}_{\boldsymbol{i}\alpha} + \sum_{\langle \boldsymbol{i}\alpha,\boldsymbol{j}\beta\rangle} i\frac{V_{\beta\alpha}z_{\boldsymbol{j}\beta,\boldsymbol{i}\alpha}}{t_{\boldsymbol{j}\beta,\boldsymbol{i}\alpha}}\hat{c}^{\dagger}_{\boldsymbol{j}\beta}\hat{c}_{\boldsymbol{i}\alpha} \\
&\equiv \sum_{\boldsymbol{i}\alpha}\tilde{\epsilon}_{\alpha}\hat{n}_{\boldsymbol{i}\alpha} + \sum_{\langle \boldsymbol{i}\alpha,\boldsymbol{j}\beta\rangle} iR_{\boldsymbol{j}\beta,\boldsymbol{i}\alpha}e^{-i\boldsymbol{Q}\cdot\boldsymbol{R_i}}\hat{c}^{\dagger}_{\boldsymbol{j}\beta}\hat{c}_{\boldsymbol{i}\alpha}\,,
\end{aligned} \tag{E.3}$$

since $V_{\beta\alpha} = V_{\alpha\beta}$, $t_{\boldsymbol{j}\beta,\boldsymbol{i}\alpha} = t_{\boldsymbol{i}\alpha,\boldsymbol{j}\beta}$, and $z_{\boldsymbol{j}\beta,\boldsymbol{i}\alpha} = -z_{\boldsymbol{i}\alpha,\boldsymbol{j}\beta}$. We have defined above the parameters $R_{\boldsymbol{j}\beta,\boldsymbol{i}\alpha} = \frac{V_{\beta\alpha}z_{\boldsymbol{j}\beta,\boldsymbol{i}\alpha}}{t_{\boldsymbol{j}\beta,\boldsymbol{i}\alpha}}e^{i\boldsymbol{Q}\cdot\boldsymbol{R_i}}$ which share similarities with $t_{\boldsymbol{j}\beta,\boldsymbol{i}\alpha}$ since they can be expressed in terms of α, β, and n the inequivalent bond between $\boldsymbol{i}\alpha$ and $\boldsymbol{j}\beta$ as $R^n_{\beta\alpha}$. In light of this, we let $R_{pd} \equiv \frac{V_{pd}z_{pd}}{t_{pd}}$ and $R_{pp} \equiv \frac{V_{pp}z_{pp}}{t_{pp}}$. Note that the sign of $R^n_{\beta\alpha}$ depends on both the orbital phase convention and the direction of the current from α to β on the inequivalent bond n. Hence, the order of the orbitals in the notation is essential. Notice the difference with the tunneling matrix elements: $t^n_{\beta\alpha} = t^n_{\alpha\beta}$ while $R^n_{\beta\alpha} = -R^n_{\alpha\beta}$.

As a result, the mean-field version of the charge order in position space is expressed as

$$\hat{H}'_{MF} = \sum_{\boldsymbol{i}\alpha}\tilde{\epsilon}_{\alpha}\hat{n}_{\boldsymbol{i}\alpha} + \sum_{\langle \boldsymbol{i}\alpha,\boldsymbol{j}\beta\rangle} iR_{\boldsymbol{j}\beta,\boldsymbol{i}\alpha}e^{-i\boldsymbol{Q}\cdot\boldsymbol{R_i}}\hat{c}^{\dagger}_{\boldsymbol{j}\beta}\hat{c}_{\boldsymbol{i}\alpha}\,, \tag{E.4}$$

where the sum over $\langle \boldsymbol{i}\alpha, \boldsymbol{j}\beta\rangle$ includes nearest neighbor p–d and p–p bonds.

According to (4.3) and together with the fact that $\frac{1}{N^2}\sum_{\boldsymbol{i}} e^{i\boldsymbol{k}\cdot\boldsymbol{R}_{\boldsymbol{i}\alpha}} = \delta_{\boldsymbol{k},\boldsymbol{0}}$,

$$\begin{aligned}\sum_{\boldsymbol{i}\alpha}\tilde{\epsilon}_\alpha\hat{n}_{\boldsymbol{i}\alpha} &= \sum_{\boldsymbol{k}\alpha,\boldsymbol{k}'}\tilde{\epsilon}_\alpha\left[\tfrac{1}{N^2}\sum_{\boldsymbol{i}} e^{i[\boldsymbol{k}-\boldsymbol{k}']\cdot\boldsymbol{R}_{\boldsymbol{i}\alpha}}\right]\hat{c}^\dagger_{\boldsymbol{k}'\alpha}\hat{c}_{\boldsymbol{k}\alpha} \\ &= \sum_{\boldsymbol{k}\alpha}\tilde{\epsilon}_\alpha\hat{n}_{\boldsymbol{k}\alpha}\,,\end{aligned} \tag{E.5}$$

$$\begin{aligned}&\sum_{\langle\boldsymbol{i}\alpha,\boldsymbol{j}\beta\rangle} iR_{\boldsymbol{j}\beta,\boldsymbol{i}\alpha}e^{-i\boldsymbol{Q}\cdot\boldsymbol{R}_{\boldsymbol{i}}}\hat{c}^\dagger_{\boldsymbol{j}\beta}\hat{c}_{\boldsymbol{i}\alpha} \\ &\qquad= \sum_{\boldsymbol{k}\alpha,\boldsymbol{k}'\beta,n} ie^{i\boldsymbol{Q}\cdot\boldsymbol{\delta}_\alpha}R^n_{\beta\alpha}e^{-i\boldsymbol{k}'\cdot\boldsymbol{\delta}^n_{\beta\alpha}}\left[\tfrac{1}{N^2}\sum_{\boldsymbol{i}} e^{i[\boldsymbol{k}-\{\boldsymbol{k}'+\boldsymbol{Q}\}]\cdot\boldsymbol{R}_{\boldsymbol{i}\alpha}}\right]\hat{c}^\dagger_{\boldsymbol{k}'\beta}\hat{c}_{\boldsymbol{k}\alpha} \\ &\qquad= \sum_{\boldsymbol{k}\alpha\beta,n} ie^{i\boldsymbol{Q}\cdot\boldsymbol{\delta}_\alpha}R^n_{\beta\alpha}e^{-i\boldsymbol{k}\cdot\boldsymbol{\delta}^n_{\beta\alpha}}\hat{c}^\dagger_{\boldsymbol{k}\beta}\hat{c}_{\boldsymbol{k}+\boldsymbol{Q}\alpha} \\ &\qquad\equiv \sum_{\boldsymbol{k}\alpha\beta} g_{\beta\alpha}(\boldsymbol{k})\hat{c}^\dagger_{\boldsymbol{k}\beta}\hat{c}_{\boldsymbol{k}+\boldsymbol{Q}\alpha}\,.\end{aligned} \tag{E.6}$$

Because of Hermicity and by definition of the momentum operators,

$$\sum_{\boldsymbol{k}\alpha\beta} g_{\beta\alpha}(\boldsymbol{k})\hat{c}^\dagger_{\boldsymbol{k}\beta}\hat{c}_{\boldsymbol{k}+\boldsymbol{Q}\alpha} = \sum_{\boldsymbol{k}\alpha\beta} e^{2i\boldsymbol{Q}\cdot\boldsymbol{\delta}_\beta}g^*_{\alpha\beta}(\boldsymbol{k}+\boldsymbol{Q})\hat{c}^\dagger_{\boldsymbol{k}\beta}\hat{c}_{\boldsymbol{k}+\boldsymbol{Q}\alpha}\,. \tag{E.7}$$

In such a way,

$$\begin{aligned}\hat{H}'_{MF} &= \sum_{\boldsymbol{k}\alpha}\tilde{\epsilon}_\alpha\hat{n}_{\boldsymbol{k}\alpha} + \sum_{\boldsymbol{k}\alpha\beta} g_{\beta\alpha}(\boldsymbol{k})\hat{c}^\dagger_{\boldsymbol{k}\beta}\hat{c}_{\boldsymbol{k}+\boldsymbol{Q}\alpha} \\ &= \sum_{\boldsymbol{k}}\Psi^\dagger_{\boldsymbol{k}}\begin{bmatrix}\tilde{\epsilon}_d & 0 & 0\\ 0 & \tilde{\epsilon}_p & 0\\ 0 & 0 & \tilde{\epsilon}_p\end{bmatrix}\Psi_{\boldsymbol{k}} + \sum_{\boldsymbol{k}}\Psi^\dagger_{\boldsymbol{k}}\begin{bmatrix}0 & g^*_{xd}(\boldsymbol{k}+\boldsymbol{Q}) & g^*_{yd}(\boldsymbol{k}+\boldsymbol{Q})\\ g_{xd}(\boldsymbol{k}) & 0 & -g^*_{yx}(\boldsymbol{k}+\boldsymbol{Q})\\ g_{yd}(\boldsymbol{k}) & g_{yx}(\boldsymbol{k}) & 0\end{bmatrix}\Psi_{\boldsymbol{k}+\boldsymbol{Q}} \\ &\equiv \sum_{\boldsymbol{k}}\Psi^\dagger_{\boldsymbol{k}}\tilde{\boldsymbol{\epsilon}}\Psi_{\boldsymbol{k}} + \sum_{\boldsymbol{k}}\Psi^\dagger_{\boldsymbol{k}}\boldsymbol{H}_1(\boldsymbol{k})\Psi_{\boldsymbol{k}+\boldsymbol{Q}} \\ &= \sum_{\boldsymbol{k}\in BZ'}\begin{bmatrix}\Psi^\dagger_{\boldsymbol{k}} & \Psi^\dagger_{\boldsymbol{k}+\boldsymbol{Q}}\end{bmatrix}\begin{bmatrix}\tilde{\boldsymbol{\epsilon}} & \boldsymbol{H}_1(\boldsymbol{k})\\ \boldsymbol{H}^\dagger_1(\boldsymbol{k}) & \tilde{\boldsymbol{\epsilon}}\end{bmatrix}\begin{bmatrix}\Psi_{\boldsymbol{k}}\\ \Psi_{\boldsymbol{k}+\boldsymbol{Q}}\end{bmatrix},\end{aligned} \tag{E.8}$$

where explicit expressions for $g_{\beta\alpha}(\boldsymbol{k})$ depend on the current pattern. Note that the gauge transformation from (4.8) has not been applied yet.

Appendix F: Alternative Way of Expressing the Mean-Field Hamiltonian

Without loss of generality, let $\boldsymbol{H}_{MF}(\boldsymbol{k}) \to \boldsymbol{H}_{MF}(\boldsymbol{k}) - \varepsilon_p \boldsymbol{I}$ so that $\varepsilon_d \to \varepsilon_d - \varepsilon_p \equiv \Delta\varepsilon$ and $\varepsilon_p \to 0$. By defining $\boldsymbol{K} \equiv \frac{1}{\sqrt{2}} \begin{bmatrix} \boldsymbol{J} & -\boldsymbol{I} \\ \boldsymbol{J} & \boldsymbol{I} \end{bmatrix}$ for J as defined in (D.2), one finds

$$\begin{aligned} \boldsymbol{K}\boldsymbol{H}_{MF}(\boldsymbol{k})\boldsymbol{K}^\dagger &= \begin{bmatrix} \boldsymbol{H}_0^+(\boldsymbol{k}) + \boldsymbol{H}_1^+(\boldsymbol{k}) & \boldsymbol{H}_0^-(\boldsymbol{k}) - \boldsymbol{H}_1^-(\boldsymbol{k}) \\ \boldsymbol{H}_0^-(\boldsymbol{k}) + \boldsymbol{H}_1^-(\boldsymbol{k}) & \boldsymbol{H}_0^+(\boldsymbol{k}) - \boldsymbol{H}_1^+(\boldsymbol{k}) \end{bmatrix} \\ &\equiv \begin{bmatrix} \boldsymbol{H}_+(\boldsymbol{k}) & \boldsymbol{H}_-^*(\boldsymbol{k}) \\ \boldsymbol{H}_-(\boldsymbol{k}) & \boldsymbol{H}_+^*(\boldsymbol{k}) \end{bmatrix}, \end{aligned} \tag{F.1}$$

for $\boldsymbol{H}_0^\pm(\boldsymbol{k}) \equiv \frac{1}{2}[\boldsymbol{J}\boldsymbol{H}_0(\boldsymbol{k})\boldsymbol{J} \pm \boldsymbol{H}_0(\boldsymbol{k}+\boldsymbol{Q})]$ and $\boldsymbol{H}_1^\pm(\boldsymbol{k}) \equiv -\frac{\lambda}{2i}[\boldsymbol{J}\boldsymbol{V}(\boldsymbol{k}) \mp \boldsymbol{V}^T(\boldsymbol{k})\boldsymbol{J}]$. To simplify further the analysis around points in D, $\boldsymbol{k}$ must be expressed in terms of another vector $\tilde{\boldsymbol{k}}$ such that $\boldsymbol{k}(\tilde{\boldsymbol{k}}) = \Big(\sigma_x[\frac{\pi}{2a} + \tilde{k}^x],\ \sigma_y[\frac{\pi}{2a} + \tilde{k}^y]\Big)$. In such a way,

$$\begin{aligned} \boldsymbol{K}\boldsymbol{H}_{MF}(\boldsymbol{k}(\tilde{\boldsymbol{k}}))\boldsymbol{K}^\dagger &= \begin{bmatrix} \boldsymbol{H}_+(\boldsymbol{k}(\tilde{\boldsymbol{k}})) & \boldsymbol{H}_-^*(\boldsymbol{k}(\tilde{\boldsymbol{k}})) \\ \boldsymbol{H}_-(\boldsymbol{k}(\tilde{\boldsymbol{k}})) & \boldsymbol{H}_+^*(\boldsymbol{k}(\tilde{\boldsymbol{k}})) \end{bmatrix} \\ &\equiv \begin{bmatrix} \boldsymbol{H}'_+(\tilde{\boldsymbol{k}}) & \boldsymbol{H}'^*_-(\tilde{\boldsymbol{k}}) \\ \boldsymbol{H}'_-(\tilde{\boldsymbol{k}}) & \boldsymbol{H}'^*_+(\tilde{\boldsymbol{k}}) \end{bmatrix}. \end{aligned} \tag{F.2}$$

Although it may look complicated, it leads to very simple matrices:

$$\boldsymbol{H}'_+(\boldsymbol{k}) = \begin{bmatrix} \Delta\varepsilon & \sqrt{2}t_d^* c_x & -\sqrt{2}t_d c_y \\ \sqrt{2}t_d c_x & 0 & 2t_p^* s_x s_y + 2t_p c_x c_y \\ -\sqrt{2}t_d^* c_y & 2t_p s_x s_y + 2t_p^* c_x c_y & 0 \end{bmatrix} \tag{F.3a}$$

$$\boldsymbol{H}'_-(\boldsymbol{k}) = \begin{bmatrix} 0 & \sqrt{2}t_d s_x & -\sqrt{2}t_d^* s_y \\ \sqrt{2}t_d s_x & 0 & 2t_p s_x c_y + 2t_p^* c_x s_y \\ -\sqrt{2}t_d^* s_y & 2t_p s_x c_y + 2t_p^* c_x s_y & 0 \end{bmatrix}, \tag{F.3b}$$

where we have defined $t_d \equiv t_{pd} + iR_{pd}$ and $t_p \equiv t_{pp} + i\phi R_{pp}$. This form shows that all the eigenvalues at points in D are 2-fold degenerate since $\boldsymbol{H}'_-(\boldsymbol{0}) = \boldsymbol{0}$.

It is valuable to express $\boldsymbol{H}_{MF}(\boldsymbol{k}(\tilde{\boldsymbol{k}}))$ in its original form in terms of the two matrices found in (F.3). It can be done by doing a matrix transformation on (F.2) using $\boldsymbol{K}$. In turn,

new expressions for the block matrices are obtained:

$$\boldsymbol{H}_0(\boldsymbol{k}(\tilde{\boldsymbol{k}})) = \boldsymbol{J}\,\mathrm{Re}[\boldsymbol{H}'_+(\tilde{\boldsymbol{k}}) + \boldsymbol{H}'_-(\tilde{\boldsymbol{k}})]\boldsymbol{J} \tag{F.4a}$$

$$\boldsymbol{H}_0(\boldsymbol{k}(\tilde{\boldsymbol{k}}) + \boldsymbol{Q}) = \mathrm{Re}[\boldsymbol{H}'_+(\tilde{\boldsymbol{k}}) - \boldsymbol{H}'_-(\tilde{\boldsymbol{k}})] \tag{F.4b}$$

$$\boldsymbol{V}(\boldsymbol{k}(\tilde{\boldsymbol{k}})) = \boldsymbol{J}\lambda^{-1}\,\mathrm{Im}[\boldsymbol{H}'_+(\tilde{\boldsymbol{k}}) + \boldsymbol{H}'_-(\tilde{\boldsymbol{k}})]\,. \tag{F.4c}$$

In fact, these expressions are easier to work with when investigating the vicinity of any point of the form $\frac{\pi}{2a}\left(\sigma_x,\ \sigma_y\right) \in D$. When expanding in powers of $|\tilde{\boldsymbol{k}}|$ specifically, $\boldsymbol{H}'_+(\tilde{\boldsymbol{k}})$ will only contain even powers while $\boldsymbol{H}'_-(\tilde{\boldsymbol{k}})$ will only contain odd ones. Consequently, it should be the case that $\boldsymbol{H}_0(\boldsymbol{k}(\tilde{\boldsymbol{k}}) + \boldsymbol{Q}) = \boldsymbol{J}\boldsymbol{H}_0(\boldsymbol{k}(-\tilde{\boldsymbol{k}}))\boldsymbol{J}$, leading the eigenstates to then satisfy $|n(\boldsymbol{k}(\tilde{\boldsymbol{k}}) + \boldsymbol{Q})\rangle = \pm\boldsymbol{J}\,|n(\boldsymbol{k}(-\tilde{\boldsymbol{k}}))\rangle$. Notice furthermore that $\mathrm{Re}[\boldsymbol{H}'_\pm(\tilde{\boldsymbol{k}})]$ and $\mathrm{Im}[\boldsymbol{H}'_-(\tilde{\boldsymbol{k}})]$ are symmetric matrices while $\mathrm{Im}[\boldsymbol{H}'_+(\tilde{\boldsymbol{k}})]$ is antisymmetric.

It is under such considerations that we can make the assumption that along $\boldsymbol{k} \in \partial BZ'$ in the vicinity of D, $\langle n(\boldsymbol{k})|\,\boldsymbol{V}(\boldsymbol{k})\,|n(\boldsymbol{k}+\boldsymbol{Q})\rangle = 0$ if and only if $\boldsymbol{k} \in D$. First, by letting the dependence of $\boldsymbol{k}$ on $\tilde{\boldsymbol{k}}$ implicit on the left-hand side:

$$\langle n(\boldsymbol{k})|\,\boldsymbol{V}(\boldsymbol{k})\,|n(\boldsymbol{k}+\boldsymbol{Q})\rangle = \pm\lambda^{-1}\,\langle n(\boldsymbol{k}(\tilde{\boldsymbol{k}}))|\,\boldsymbol{J}\,\mathrm{Im}[\boldsymbol{H}'_+(\tilde{\boldsymbol{k}}) + \boldsymbol{H}'_-(\tilde{\boldsymbol{k}})]\boldsymbol{J}\,|n(\boldsymbol{k}(-\tilde{\boldsymbol{k}}))\rangle\ . \tag{F.5}$$

However, since $\mathrm{Im}[\boldsymbol{H}'_+(\tilde{\boldsymbol{k}})]$ is antisymmetric, $\langle n(\boldsymbol{k}(\tilde{\boldsymbol{k}}))|\,\boldsymbol{J}\,\mathrm{Im}[\boldsymbol{H}'_+(\tilde{\boldsymbol{k}})]\boldsymbol{J}\,|n(\boldsymbol{k}(-\tilde{\boldsymbol{k}}))\rangle$ is identically zero when $|n(\boldsymbol{k}(\tilde{\boldsymbol{k}}))\rangle \propto |n(\boldsymbol{k}(-\tilde{\boldsymbol{k}}))\rangle$. On top of this, since $\mathrm{Im}[\boldsymbol{H}'_-(\tilde{\boldsymbol{k}})]$ is symmetric, $\langle n(\boldsymbol{k}(\tilde{\boldsymbol{k}}))|\,\boldsymbol{J}\,\mathrm{Im}[\boldsymbol{H}'_-(\tilde{\boldsymbol{k}})]\boldsymbol{J}\,|n(\boldsymbol{k}(-\tilde{\boldsymbol{k}}))\rangle$ is identically zero when $\mathrm{Im}[\boldsymbol{H}'_-(\tilde{\boldsymbol{k}})] = \boldsymbol{0}$. Both conditions are satisfied at $\tilde{\boldsymbol{k}} = \boldsymbol{0}$, i.e. when $\boldsymbol{k} \in D$. More generally, it is practically impossible for both terms to sum up to zero at any other point around — more evidences will be given in appendix G.

In fact, the assumption made above is something observed numerically: for any $k \in \partial BZ'$, $\langle n(\boldsymbol{k})|\,\boldsymbol{V}(\boldsymbol{k})\,|n(\boldsymbol{k}+\boldsymbol{Q})\rangle = 0$ if and only if $\boldsymbol{k} \in D$ for both the lowest and highest energy bands, or if $\boldsymbol{k} \in D$ and either $k_x = 0$ or $k_y = 0$ for the middle energy band. However, note that momenta along $\partial BZ'$ with $k_x = 0$ or $k_y = 0$ are not part of the hole pockets surrounding the points in D. Having $\langle n(\boldsymbol{k})|\,\boldsymbol{V}(\boldsymbol{k})\,|n(\boldsymbol{k}+\boldsymbol{Q})\rangle = 0$ at some point $\boldsymbol{k} \in \partial BZ' \setminus D$ means that there is another degeneracy point; hence, there must be a single degeneracy within each individual hole pocket.

Appendix G: Absence of Singular Points

The focus needs to be made on the degeneracies and their vicinity. It can be achieved by letting $\boldsymbol{k}(\tilde{\boldsymbol{k}}) = \Big(\sigma_x[\frac{\pi}{2a} + \tilde{k}^x],\ \sigma_y[\frac{\pi}{2a} + \tilde{k}^y]\Big)$ for $\sigma_x, \sigma_y \in \{\pm 1\}$. Furthermore, it helps to consider the block matrices of $\boldsymbol{H}_{MF}(\boldsymbol{k})$ as expressed in (F.4). In light of this, we now consider the eigenvalues $E_n(\boldsymbol{k})$ and corresponding eigenstates $|n(\boldsymbol{k})\rangle$ of $\boldsymbol{H}_0(\boldsymbol{k})$ with $\boldsymbol{k}$ in terms of $\tilde{\boldsymbol{k}}$. By taking $|\tilde{\boldsymbol{k}}|$ as the perturbation parameter and θ such that $\tilde{\boldsymbol{k}} = |\tilde{\boldsymbol{k}}|\hat{\boldsymbol{r}}$ for $\hat{\boldsymbol{r}} = \Big(\cos\theta,\ \sin\theta\Big)$, $\boldsymbol{J}\boldsymbol{H}_0(\boldsymbol{k}(\tilde{\boldsymbol{k}}))\boldsymbol{J}$ can be expressed in powers of $|\tilde{\boldsymbol{k}}|$ as

$$\boldsymbol{J}\boldsymbol{H}_0(\boldsymbol{k}(\tilde{\boldsymbol{k}}))\boldsymbol{J} = \mathrm{Re}[\boldsymbol{H}'_+(\boldsymbol{0})] + |\tilde{\boldsymbol{k}}|\hat{\boldsymbol{r}} \cdot \mathrm{Re}[\nabla \boldsymbol{H}'_-(\boldsymbol{0})] + \mathcal{O}(|\tilde{\boldsymbol{k}}|^2)\,, \tag{G.1}$$

where ∇ is the gradient with respect to $\tilde{\boldsymbol{k}}$.

Perturbation theory can be used by taking $\mathrm{Re}[\boldsymbol{H}'_+(\boldsymbol{0})]$ as the unperturbed Hamiltonian and $|\tilde{\boldsymbol{k}}|$ as the perturbation parameter. Let $|n^{(0)}\rangle$ be the eigenstates of $\mathrm{Re}[\boldsymbol{H}'_+(\boldsymbol{0})]$ with corresponding eigenvalues $E_n^{(0)}$. The solutions have been derived in appendix D, but with $\Delta\epsilon$ instead of $\Delta\varepsilon$. According to perturbation theory in section B.1:

$$E_+(\boldsymbol{k}(\tilde{\boldsymbol{k}})) = E_+^{(0)} + |\tilde{\boldsymbol{k}}|\hat{\boldsymbol{r}} \cdot \langle +^{(0)}| \,\mathrm{Re}[\nabla \boldsymbol{H}'_-(\boldsymbol{0})]\, |+^{(0)}\rangle + \mathcal{O}(|\tilde{\boldsymbol{k}}|^2)\,, \tag{G.2a}$$

$$|+(\boldsymbol{k}(\tilde{\boldsymbol{k}}))\rangle = \boldsymbol{J}\,|+^{(0)}\rangle + \boldsymbol{J}|\tilde{\boldsymbol{k}}|\hat{\boldsymbol{r}} \cdot \sum_{n\neq +} \frac{\langle n^{(0)}| \,\mathrm{Re}[\nabla \boldsymbol{H}'_-(\boldsymbol{0})]\, |+^{(0)}\rangle}{E_+^{(0)} - E_n^{(0)}}\, |n^{(0)}\rangle + \mathcal{O}(|\tilde{\boldsymbol{k}}|^2)\,. \tag{G.2b}$$

Furthermore, recall that $\boldsymbol{H}_0(\boldsymbol{k}(\tilde{\boldsymbol{k}}) + \boldsymbol{Q}) = \boldsymbol{J}\boldsymbol{H}_0(\boldsymbol{k}(-\tilde{\boldsymbol{k}}))\boldsymbol{J}$ from (F.4). Consequently, it must hold that $E_+(\boldsymbol{k}(\tilde{\boldsymbol{k}}) + \boldsymbol{Q}) = E_+(\boldsymbol{k}(-\tilde{\boldsymbol{k}}))$ and $|+(\boldsymbol{k}(\tilde{\boldsymbol{k}}) + \boldsymbol{Q})\rangle = \pm\boldsymbol{J}\,|+(\boldsymbol{k}(-\tilde{\boldsymbol{k}}))\rangle$.

It is now possible to find explicit expressions for $\bar{E}(\boldsymbol{k})$, $\varepsilon(\boldsymbol{k})$, and $\Delta(\boldsymbol{k})$ by taking $\boldsymbol{k}$ in terms of $\tilde{\boldsymbol{k}}$. In such a way, $\bar{E}(\boldsymbol{k}(\tilde{\boldsymbol{k}})) = E_+^{(0)} + \mathcal{O}(|\tilde{\boldsymbol{k}}|^2)$, $\varepsilon(\boldsymbol{k}(\tilde{\boldsymbol{k}})) = |\tilde{\boldsymbol{k}}|\hat{\boldsymbol{r}} \cdot \boldsymbol{\varepsilon}^{(1)} + \mathcal{O}(|\tilde{\boldsymbol{k}}|^2)$ and $\Delta(\boldsymbol{k}(\tilde{\boldsymbol{k}})) = |\tilde{\boldsymbol{k}}|\hat{\boldsymbol{r}} \cdot \boldsymbol{\Delta}^{(1)} + \mathcal{O}(|\tilde{\boldsymbol{k}}|^2)$ for

$$\boldsymbol{\varepsilon}^{(1)} = \langle +^{(0)}| \,\mathrm{Re}[\nabla \boldsymbol{H}'_-(\boldsymbol{0})]\, |+^{(0)}\rangle\ , \tag{G.3a}$$

$$\boldsymbol{\Delta}^{(1)} = \pm \begin{bmatrix} \langle +^{(0)}| \,\lambda^{-1}\,\mathrm{Im}[\nabla \boldsymbol{H}'_-(\boldsymbol{0})]\, |+^{(0)}\rangle \\ + \sum_{n\neq +} \frac{2\langle n^{(0)}|\lambda^{-1}\,\mathrm{Im}[\boldsymbol{H}'_+(\boldsymbol{0})]|+^{(0)}\rangle}{E_+^{(0)} - E_n^{(0)}}\, \langle n^{(0)}| \,\mathrm{Re}[\nabla \boldsymbol{H}'_-(\boldsymbol{0})]\, |+^{(0)}\rangle \end{bmatrix}\ . \tag{G.3b}$$

It is reassuring so far that $\boldsymbol{\varepsilon}^{(1)}$ and $\boldsymbol{\Delta}^{(1)}$ are not identically zero.

It is in fact possible to find explicit expressions for both $\boldsymbol{\varepsilon}^{(1)}$ and $\boldsymbol{\Delta}^{(1)}$. Since

$$\mathrm{Re}[\nabla \boldsymbol{H}'_{-}(\mathbf{0})] = \frac{a}{2}\left(\begin{bmatrix} 0 & \sqrt{2}t_{pd} & 0 \\ \sqrt{2}t_{pd} & 0 & 2t_{pp} \\ 0 & 2t_{pp} & 0 \end{bmatrix}, \begin{bmatrix} 0 & 0 & -\sqrt{2}t_{pd} \\ 0 & 0 & 2t_{pp} \\ -\sqrt{2}t_{pd} & 2t_{pp} & 0 \end{bmatrix}\right), \tag{G.4}$$

we obtain $\boldsymbol{\varepsilon}^{(1)} = \frac{1}{2}ac_{+}^{2}E_{+}^{(0)}\begin{pmatrix}1, & 1\end{pmatrix}$ while $\langle 0^{(0)}|\,\mathrm{Re}[\nabla \boldsymbol{H}'_{-}(\mathbf{0})]\,|+^{(0)}\rangle = \frac{1}{2}ac_{+}a_{+}t_{pd}\begin{pmatrix}1, & -1\end{pmatrix}$ and $\langle -^{(0)}|\,\mathrm{Re}[\nabla \boldsymbol{H}'_{-}(\mathbf{0})]\,|+^{(0)}\rangle = \frac{1}{4}ac_{+}c_{-}[\Delta\varepsilon - 2t_{pp}]\begin{pmatrix}1, & 1\end{pmatrix}$. Additionally,

$$\lambda^{-1}\,\mathrm{Im}[\nabla \boldsymbol{H}'_{-}(\mathbf{0})] = \frac{a}{2}\left(\begin{bmatrix} 0 & \sqrt{2}r_{pd} & 0 \\ \sqrt{2}r_{pd} & 0 & 2\phi r_{pp} \\ 0 & 2\phi r_{pp} & 0 \end{bmatrix}, \begin{bmatrix} 0 & 0 & \sqrt{2}r_{pd} \\ 0 & 0 & -2\phi r_{pp} \\ \sqrt{2}r_{pd} & -2\phi r_{pp} & 0 \end{bmatrix}\right), \tag{G.5}$$

where $r_{pd} \equiv R_{pd}/\lambda = V_{pd}$ and $r_{pp} \equiv R_{pp}/\lambda = \frac{z_{pp}/z_{pd}}{t_{pp}/t_{pd}}V_{pp}$ which are both of the order of magnitude of 1, and $\langle +^{(0)}|\,\lambda^{-1}\,\mathrm{Im}[\nabla \boldsymbol{H}'_{-}(\mathbf{0})]\,|+^{(0)}\rangle = ac_{+}^{2}\,[a_{+}r_{pd} - \phi r_{pp}]\begin{pmatrix}1, & -1\end{pmatrix}$. Finally, with

$$\lambda^{-1}\,\mathrm{Im}[\boldsymbol{H}'_{+}(\mathbf{0})] = \begin{bmatrix} 0 & -\sqrt{2}r_{pd} & -\sqrt{2}r_{pd} \\ \sqrt{2}r_{pd} & 0 & 2\phi r_{pp} \\ \sqrt{2}r_{pd} & -2\phi r_{pp} & 0 \end{bmatrix}, \tag{G.6}$$

we obtain $\langle 0^{(0)}|\,\lambda^{-1}\,\mathrm{Im}[\boldsymbol{H}'_{+}(\mathbf{0})]\,|+^{(0)}\rangle = 2c_{+}\,[a_{+}r_{pd} - \phi r_{pp}]$.

Those multiple results yield in the end that

$$|\boldsymbol{\varepsilon}^{(1)} \times \boldsymbol{\Delta}^{(1)}| = a^{2}c_{+}^{4}E_{+}^{(0)}t_{pd}\,|1 + f_{E}|\,|a_{+}r_{pd} - \phi r_{pp}|\,, \tag{G.7}$$

for $f_{E} \equiv \frac{1}{2}\frac{E_{+}^{(0)}+E_{0}^{(0)}}{E_{+}^{(0)}-E_{0}^{(0)}}$. Under a typical parameter set, $|\boldsymbol{\varepsilon}^{(1)} \times \boldsymbol{\Delta}^{(1)}| \neq 0$ for *any* current pattern. More generally, the parameters still need to be fine-tuned for $|\boldsymbol{\varepsilon}^{(1)} \times \boldsymbol{\Delta}^{(1)}| = 0$ to hold.

Appendix H: Peierls Substitution for the πLC Hamiltonian

We start by expressing the full mean-field Hamiltonian in terms of the position-space operators:

$$\begin{aligned}\hat{H}_{MF} &= \sum_{\boldsymbol{i}\alpha} \varepsilon_\alpha \hat{n}_{\boldsymbol{i}\alpha} + \sum_{\langle \boldsymbol{i}\alpha, \boldsymbol{j}\beta\rangle} t_{\boldsymbol{j}\beta,\boldsymbol{i}\alpha} \hat{c}^\dagger_{\boldsymbol{j}\beta} \hat{c}_{\boldsymbol{i}\alpha} + \sum_{\langle \boldsymbol{i}\alpha, \boldsymbol{j}\beta\rangle} iR_{\boldsymbol{j}\beta,\boldsymbol{i}\alpha} e^{-i\boldsymbol{Q}\cdot\boldsymbol{R_i}} \hat{c}^\dagger_{\boldsymbol{j}\beta} \hat{c}_{\boldsymbol{i}\alpha} \\ &= \sum_{\boldsymbol{i}\alpha} \varepsilon_\alpha \hat{n}_{\boldsymbol{i}\alpha} + \sum_{\langle \boldsymbol{i}\alpha, \boldsymbol{j}\beta\rangle} t'_{\boldsymbol{j}\beta,\boldsymbol{i}\alpha} \hat{c}^\dagger_{\boldsymbol{j}\beta} \hat{c}_{\boldsymbol{i}\alpha}\,,\end{aligned} \tag{H.1}$$

where $t'_{\boldsymbol{j}\beta,\boldsymbol{i}\alpha} \equiv t_{\boldsymbol{j}\beta,\boldsymbol{i}\alpha} + iR_{\boldsymbol{j}\beta,\boldsymbol{i}\alpha} e^{-i\boldsymbol{Q}\cdot\boldsymbol{R_i}}$. This form has the advantage of grouping together all the hopping terms from one specific site to another.

In order to simplify the next derivation, we take a *current* unit cell of two *primitive* unit cells corresponding to the true unit cells of the system once the direction of the current is taken into account. explicitly, a current cell labeled by $\boldsymbol{i}$ will be composed of the $\Big(i_x - i_y,\ i_x + i_y\Big)^{th}$ and $\Big(i_x - i_y,\ i_x + i_y + 1\Big)^{th}$ primitive cells. Then, we rotate the frame by 45° counterclockwise, which is equivalent to rotating the position of the atoms by 45° clockwise. In such a way, the Hamiltonian can be expressed in terms of operators $\hat{c}_{\boldsymbol{i}\alpha\nu}$ where $\boldsymbol{i}$ labels each current cell of two primitive cells, α labels the orbitals, and $\nu \in \{1, 2\}$ labels the primitive cells within the current cell:

$$\hat{H}_{MF} = \sum_{\boldsymbol{i}\alpha\nu} \varepsilon_\alpha \hat{n}_{\boldsymbol{i}\alpha\nu} + \sum_{\langle \boldsymbol{i}\alpha\nu, \boldsymbol{j}\beta\mu\rangle} t'_{\boldsymbol{j}\beta\mu,\boldsymbol{i}\alpha\nu} \hat{c}^\dagger_{\boldsymbol{j}\beta\mu} \hat{c}_{\boldsymbol{i}\alpha\nu}\,, \tag{H.2}$$

where $t'_{\boldsymbol{j}\beta\mu,\boldsymbol{i}\alpha\nu} \equiv t_{\boldsymbol{j}\beta\mu,\boldsymbol{i}\alpha\nu} + iR_{\boldsymbol{j}\beta\mu,\boldsymbol{i}\alpha\nu}(-1)^{\nu-1}$. Note in particular that $\boldsymbol{Q} = \Big(\frac{\pi}{\sqrt{2}a},\ 0\Big)$. Without loss of generality, let $t'_{\boldsymbol{j}\beta\mu,\boldsymbol{i}\alpha\nu} \to t_{\boldsymbol{j}\beta\mu,\boldsymbol{i}\alpha\nu} + iR_{\boldsymbol{j}\beta\mu,\boldsymbol{i}\alpha\nu}(-1)^{\nu}$.

To include an external magnetic field in the Hamiltonian, we apply the Peierls substition:

$$\hat{c}^\dagger_{\boldsymbol{j}\beta\mu} \hat{c}_{\boldsymbol{i}\alpha\nu} \to \exp\left[-i2\pi \frac{e}{h} \int_{\boldsymbol{R}_{\boldsymbol{i}\alpha\nu}}^{\boldsymbol{R}_{\boldsymbol{j}\beta\mu}} \boldsymbol{A}(\boldsymbol{r}) \cdot d\boldsymbol{r}\right] \hat{c}^\dagger_{\boldsymbol{j}\beta\mu} \hat{c}_{\boldsymbol{i}\alpha\nu}\,, \tag{H.3}$$

where e is the charge of the electron, $\boldsymbol{A}(\boldsymbol{r})$ is the magnetic vector potential in function of position $\boldsymbol{r}$, and $\boldsymbol{R}_{\boldsymbol{i}\alpha\nu} \equiv \boldsymbol{R_i} + [\nu - 1]\left(\frac{a}{\sqrt{2}},\ \frac{a}{\sqrt{2}}\right) + \boldsymbol{\delta}_\alpha$ such that $\boldsymbol{R_i}$ is the position vector of current cell $\boldsymbol{i}$. explicitly, $\boldsymbol{R_i} = \sqrt{2}a\boldsymbol{i} = \Big(\sqrt{2}ai_x,\ \sqrt{2}ai_y\Big)$, while $\boldsymbol{\delta}_d = \Big(0,\ 0\Big)$, $\boldsymbol{\delta}_x = \Big(\frac{a}{2\sqrt{2}},\ -\frac{a}{2\sqrt{2}}\Big)$ and $\boldsymbol{\delta}_y = \Big(\frac{a}{2\sqrt{2}},\ \frac{a}{2\sqrt{2}}\Big)$. Without loss of generality, let $\boldsymbol{R}_{\boldsymbol{i}\alpha\nu} \to \boldsymbol{R_i} + \nu\left(\frac{a}{\sqrt{2}},\ \frac{a}{\sqrt{2}}\right) + \boldsymbol{\delta}_\alpha$.

Consider a constant magnetic field $\boldsymbol{B} = B\hat{\boldsymbol{z}}$. The Landau gauge chosen is such that $\boldsymbol{A}(\boldsymbol{r}) = -By\hat{\boldsymbol{x}}$. Then, let $\boldsymbol{R}_{\boldsymbol{i}\alpha\nu} = X_{\boldsymbol{i}\alpha\nu}\hat{\boldsymbol{x}} + Y_{\boldsymbol{i}\alpha\nu}\hat{\boldsymbol{y}}$. Hence,

$$\begin{aligned}
\int_{\boldsymbol{R}_{\boldsymbol{i}\alpha\nu}}^{\boldsymbol{R}_{\boldsymbol{j}\beta\mu}} \boldsymbol{A}(\boldsymbol{r}) \cdot d\boldsymbol{r} &= -B \int_{\boldsymbol{R}_{\boldsymbol{i}\alpha\nu}}^{\boldsymbol{R}_{\boldsymbol{j}\beta\mu}} y(x)\, dx \\
&= -B \int_{\boldsymbol{R}_{\boldsymbol{i}\alpha\nu}}^{\boldsymbol{R}_{\boldsymbol{j}\beta\mu}} \left[Y_{\boldsymbol{i}\alpha\nu} + \frac{Y_{\boldsymbol{j}\beta\mu} - Y_{\boldsymbol{i}\alpha\nu}}{X_{\boldsymbol{j}\beta\mu} - X_{\boldsymbol{i}\alpha\nu}} \left\{ x - X_{\boldsymbol{i}\alpha\nu} \right\} \right] dx \\
&= -B \left[Y_{\boldsymbol{i}\alpha\nu} \left\{ X_{\boldsymbol{j}\beta\mu} - X_{\boldsymbol{i}\alpha\nu} \right\} + \frac{Y_{\boldsymbol{j}\beta\mu} - Y_{\boldsymbol{i}\alpha\nu}}{X_{\boldsymbol{j}\beta\mu} - X_{\boldsymbol{i}\alpha\nu}} \frac{\left\{ X_{\boldsymbol{j}\beta\mu} - X_{\boldsymbol{i}\alpha\nu} \right\}^2}{2} \right] \\
&= -B \left[X_{\boldsymbol{j}\beta\mu} - X_{\boldsymbol{i}\alpha\nu} \right] \left[Y_{\boldsymbol{i}\alpha\nu} + \tfrac{1}{2} \left\{ Y_{\boldsymbol{j}\beta\mu} - Y_{\boldsymbol{i}\alpha\nu} \right\} \right] \\
&= -B\, \hat{\boldsymbol{x}} \cdot \boldsymbol{\delta}_{\boldsymbol{i}\alpha\nu}^{\boldsymbol{j}\beta\mu} \left[Y_{\boldsymbol{i}\alpha\nu} + \tfrac{1}{2} \hat{\boldsymbol{y}} \cdot \boldsymbol{\delta}_{\boldsymbol{i}\alpha\nu}^{\boldsymbol{j}\beta\mu} \right] ,
\end{aligned} \tag{H.4}$$

where $\boldsymbol{\delta}_{\boldsymbol{i}\alpha\nu}^{\boldsymbol{j}\beta\mu} \equiv \boldsymbol{R}_{\boldsymbol{j}\beta\mu} - \boldsymbol{R}_{\boldsymbol{i}\alpha\nu}$. Accordingly, it leads to

$$-i2\pi \frac{e}{h} \int_{\boldsymbol{R}_{\boldsymbol{i}\alpha\nu}}^{\boldsymbol{R}_{\boldsymbol{j}\beta\mu}} \boldsymbol{A}(\boldsymbol{r}) \cdot d\boldsymbol{r} = i2\pi \frac{eB}{h}\, \hat{\boldsymbol{x}} \cdot \boldsymbol{\delta}_{\boldsymbol{i}\alpha\nu}^{\boldsymbol{j}\beta\mu} \left[Y_{\boldsymbol{i}\alpha\nu} + \tfrac{1}{2} \hat{\boldsymbol{y}} \cdot \boldsymbol{\delta}_{\boldsymbol{i}\alpha\nu}^{\boldsymbol{j}\beta\mu} \right] . \tag{H.5}$$

In our case, $\hat{\boldsymbol{x}} \cdot \boldsymbol{\delta}_{\boldsymbol{i}\alpha\nu}^{\boldsymbol{j}\beta\mu} \equiv \omega_{\boldsymbol{i}\alpha\nu}^{\boldsymbol{j}\beta\mu} \frac{a}{2\sqrt{2}}$ should always hold for $\omega_{\boldsymbol{i}\alpha\nu}^{\boldsymbol{j}\beta\mu} \in \mathbb{Z}$. In light of this, it is useful to define $\chi \equiv \frac{eBa^2}{2h}$ along with $\Gamma_{\alpha\nu} \equiv \frac{1}{\sqrt{2}a} Y_{\boldsymbol{0}\alpha\nu} = \frac{1}{2}\nu + \frac{1}{\sqrt{2}a} \hat{\boldsymbol{y}} \cdot \boldsymbol{\delta}_\alpha$ and $\Upsilon_{\boldsymbol{i}\alpha\nu}^{\boldsymbol{j}\beta\mu} \equiv \frac{1}{\sqrt{2}a} \hat{\boldsymbol{y}} \cdot \boldsymbol{\delta}_{\boldsymbol{i}\alpha\nu}^{\boldsymbol{j}\beta\mu}$. By doing so,

$$-i2\pi \frac{e}{h} \int_{\boldsymbol{R}_{\boldsymbol{i}\alpha\nu}}^{\boldsymbol{R}_{\boldsymbol{j}\beta\mu}} \boldsymbol{A}(\boldsymbol{r}) \cdot d\boldsymbol{r} = i2\pi\chi\, \omega_{\boldsymbol{i}\alpha\nu}^{\boldsymbol{j}\beta\mu} \left[i_y + \Gamma_{\alpha\nu} + \tfrac{1}{2} \Upsilon_{\boldsymbol{i}\alpha\nu}^{\boldsymbol{j}\beta\mu} \right] . \tag{H.6}$$

Therefore, introducing an external magnetic field $B\hat{\boldsymbol{z}}$ in the system through the Peierls substitution has the effect of tranforming $\hat{H}_{MF}$ as

$$\begin{aligned}
\hat{H}_{MF} &\to \sum_{\boldsymbol{i}\alpha\nu} \varepsilon_\alpha \hat{n}_{\boldsymbol{i}\alpha\nu} + \sum_{\langle \boldsymbol{i}\alpha\nu, \boldsymbol{j}\beta\mu \rangle} t'_{\boldsymbol{j}\beta\mu,\boldsymbol{i}\alpha\nu} e^{i2\pi\chi\omega_{\boldsymbol{i}\alpha\nu}^{\boldsymbol{j}\beta\mu}\left[i_y + \Gamma_{\alpha\nu} + \frac{1}{2}\Upsilon_{\boldsymbol{i}\alpha\nu}^{\boldsymbol{j}\beta\mu} \right]} \hat{c}_{\boldsymbol{j}\beta\mu}^\dagger \hat{c}_{\boldsymbol{i}\alpha\nu} \\
&\equiv \hat{H}_{MF}^B .
\end{aligned} \tag{H.7}$$

We cannot go to momentum space just yet because of the dependence on $\boldsymbol{i}$ — more specifically on i_y — in the second term of (H.7). Fortunately, it is periodic when $\chi \in \mathbb{Q}$. In particular, setting $\chi = p/q$ an irreducible fraction where $p \in \mathbb{Z}$ and $q \in \mathbb{N}$, the y-direction periodicity will be of q current cells. Therefore, the Hamiltonian can be diagonalized by transforming to momentum space and by taking a *magnetic* unit cell in the y-direction composed of q current cells of two primitive cells each. We will assume that $q \geq 3$.

Let $\boldsymbol{i}^r \equiv i_x\hat{\boldsymbol{x}}+(qi_y+r)\hat{\boldsymbol{y}}$ and $\hat{c}^r_{\boldsymbol{i}\alpha\nu}/\hat{c}^{r\,\dagger}_{\boldsymbol{i}\alpha\nu}/\hat{n}^r_{\boldsymbol{i}\alpha\nu}$ be the annihilation/creation/number operator for an electron in orbital α of primitive cell ν in current cell $\boldsymbol{i}^r$ where $\boldsymbol{i} = \begin{pmatrix} i_x, & i_y \end{pmatrix} \in \mathbb{Z}^2$ now indexes the grid of magnetic cells and $r \in \{1, 2, ..., q\}$ indexes the lattice sites within a magnetic cell. The Hamiltonian of the system under an external magnetic field can then be rewritten in a much simpler way:

$$\hat{H}^B_{MF} = \sum_{\boldsymbol{i}\alpha\nu r} \varepsilon_\alpha \hat{n}^r_{\boldsymbol{i}\alpha\nu} + \sum_{\langle \boldsymbol{i}\alpha\nu r, \boldsymbol{j}\beta\mu r' \rangle} \tau^{r',r}_{\boldsymbol{j}\beta\mu,\boldsymbol{i}\alpha\nu} \hat{c}^{r'\,\dagger}_{\boldsymbol{j}\beta\mu} \hat{c}^r_{\boldsymbol{i}\alpha\nu}\,, \tag{H.8}$$

where $\tau^{r',r}_{\boldsymbol{j}\beta\mu,\boldsymbol{i}\alpha\nu} \equiv t'_{\boldsymbol{j}\beta\mu r',\boldsymbol{i}\alpha\nu r} e^{i2\pi\chi\omega^{\boldsymbol{j}\beta\mu r'}_{\boldsymbol{i}\alpha\nu r}\left[r+\Gamma_{\alpha\nu}+\frac{1}{2}\Upsilon^{\boldsymbol{j}\beta\mu r'}_{\boldsymbol{i}\alpha\nu r}\right]}$.

Similar to $t_{\boldsymbol{j}\beta,\boldsymbol{i}\alpha}$ which can be expressed as $t^n_{\beta\alpha}$ where n is the inequivalent bond between $\boldsymbol{i}\alpha$ and $\boldsymbol{j}\beta$, $\tau^{r',r}_{\boldsymbol{j}\beta\mu,\boldsymbol{i}\alpha\nu}$ can be expressed as $\tau^{r',r;\,n}_{\beta\mu,\alpha\nu}$ where n is the inequivalent bond between $\boldsymbol{i}\alpha\nu r$ and $\boldsymbol{j}\beta\mu r'$. The notation then changes accordingly and we can use the results from section 4:

$$\hat{H}^B_{MF} = \sum_{\boldsymbol{k}} \widetilde{\Psi}^\dagger_{\boldsymbol{k}} \begin{bmatrix} \boldsymbol{H}^B_{1,1}(\boldsymbol{k}) & \boldsymbol{H}^{B\,\dagger}_{2,1}(\boldsymbol{k}) \\ \boldsymbol{H}^B_{2,1}(\boldsymbol{k}) & \boldsymbol{H}^B_{2,2}(\boldsymbol{k}) \end{bmatrix} \widetilde{\Psi}_{\boldsymbol{k}}\,, \tag{H.9}$$

for

$$\boldsymbol{H}^B_{\nu,\nu}(\boldsymbol{k}) \equiv \begin{bmatrix} \boldsymbol{H}^{1,1}_{\nu,\nu}(\boldsymbol{k}) & \boldsymbol{H}^{1,2}_{\nu,\nu}(\boldsymbol{k}) & \dots & \boldsymbol{H}^{1,q-1}_{\nu,\nu}(\boldsymbol{k}) & \boldsymbol{H}^{q,1\,\dagger}_{\nu,\nu}(\boldsymbol{k}) \\ \boldsymbol{H}^{1,2\,\dagger}_{\nu,\nu}(\boldsymbol{k}) & \boldsymbol{H}^{2,2}_{\nu,\nu}(\boldsymbol{k}) & \dots & \boldsymbol{H}^{2,q-1}_{\nu,\nu}(\boldsymbol{k}) & \boldsymbol{H}^{2,q}_{\nu,\nu}(\boldsymbol{k}) \\ \vdots & \vdots & \ddots & \vdots & \vdots \\ \boldsymbol{H}^{1,q-1\,\dagger}_{\nu,\nu}(\boldsymbol{k}) & \boldsymbol{H}^{2,q-1\,\dagger}_{\nu,\nu}(\boldsymbol{k}) & \dots & \boldsymbol{H}^{q-1,q-1}_{\nu,\nu}(\boldsymbol{k}) & \boldsymbol{H}^{q-1,q}_{\nu,\nu}(\boldsymbol{k}) \\ \boldsymbol{H}^{q,1}_{\nu,\nu}(\boldsymbol{k}) & \boldsymbol{H}^{2,q\,\dagger}_{\nu,\nu}(\boldsymbol{k}) & \dots & \boldsymbol{H}^{q-1,q\,\dagger}_{\nu,\nu}(\boldsymbol{k}) & \boldsymbol{H}^{q,q}_{\nu,\nu}(\boldsymbol{k}) \end{bmatrix}, \tag{H.10a}$$

$$\boldsymbol{H}^B_{2,1}(\boldsymbol{k}) \equiv \begin{bmatrix} \boldsymbol{H}^{1,1}_{2,1}(\boldsymbol{k}) & \boldsymbol{H}^{1,2}_{2,1}(\boldsymbol{k}) & \dots & \boldsymbol{H}^{1,q}_{2,1}(\boldsymbol{k}) \\ \boldsymbol{H}^{2,1}_{2,1}(\boldsymbol{k}) & \boldsymbol{H}^{2,2}_{2,1}(\boldsymbol{k}) & \dots & \boldsymbol{H}^{2,q}_{2,1}(\boldsymbol{k}) \\ \vdots & \vdots & \ddots & \vdots \\ \boldsymbol{H}^{q,1}_{2,1}(\boldsymbol{k}) & \boldsymbol{H}^{q,2}_{2,1}(\boldsymbol{k}) & \dots & \boldsymbol{H}^{q,q}_{2,1}(\boldsymbol{k}) \end{bmatrix}, \tag{H.10b}$$

where $\widetilde{\Psi}^\dagger_{\boldsymbol{k}} \equiv \begin{bmatrix} \Psi^\dagger_{\boldsymbol{k}1} & \Psi^\dagger_{\boldsymbol{k}2} \end{bmatrix}$ for $\Psi^\dagger_{\boldsymbol{k}\nu} \equiv \begin{bmatrix} \Psi^{1\,\dagger}_{\boldsymbol{k}\nu} & \Psi^{2\,\dagger}_{\boldsymbol{k}\nu} & ... & \Psi^{q\,\dagger}_{\boldsymbol{k}\nu} \end{bmatrix}$ with $\Psi^{r\,\dagger}_{\boldsymbol{k}\nu} \equiv \begin{bmatrix} \hat{c}^{r\,\dagger}_{\boldsymbol{k}d\nu} & \hat{c}^{r\,\dagger}_{\boldsymbol{k}x\nu} & \hat{c}^{r\,\dagger}_{\boldsymbol{k}y\nu} \end{bmatrix}$ where $\hat{c}^r_{\boldsymbol{k}\alpha\nu}/\hat{c}^{r\,\dagger}_{\boldsymbol{k}\alpha\nu}$ is the annihilation/creation operator for an electron in orbital α of primitive cell ν in current cell r with crystal momentum $\hbar\boldsymbol{k}$ for $\boldsymbol{k} = \begin{pmatrix} k^x, & k^y \end{pmatrix} \in \frac{2\pi}{aN}\mathbb{Z}_N \times \frac{2\pi}{aqN}\mathbb{Z}_N$. The Brillouin zone BZ_q can be taken to be the set $\frac{1}{\sqrt{2}a}[-\pi,\pi] \times \frac{\pi}{\sqrt{2}aq}[-\pi,\pi]$. In fact, we have

that

$$\boldsymbol{H}^{r',r}_{\mu,\nu}(\boldsymbol{k}) = \begin{cases} \begin{bmatrix} \varepsilon_d & f^{r,r\,*}_{x\nu,d\nu}(\boldsymbol{k}) & f^{r,r\,*}_{y\nu,d\nu}(\boldsymbol{k}) \\ f^{r,r}_{x\nu,d\nu}(\boldsymbol{k}) & \varepsilon_p & f^{r,r\,*}_{y\nu,x\nu}(\boldsymbol{k}) \\ f^{r,r}_{y\nu,d\nu}(\boldsymbol{k}) & f^{r,r}_{y\nu,x\nu}(\boldsymbol{k}) & \varepsilon_p \end{bmatrix} & , \mu = \nu,\ r' = r \\ \begin{bmatrix} 0 & f^{r',r}_{d\mu,x\nu}(\boldsymbol{k}) & f^{r',r}_{d\mu,y\nu}(\boldsymbol{k}) \\ f^{r',r}_{x\mu,d\nu}(\boldsymbol{k}) & 0 & f^{r',r}_{x\mu,y\nu}(\boldsymbol{k}) \\ f^{r',r}_{y\mu,d\nu}(\boldsymbol{k}) & f^{r',r}_{y\mu,x\nu}(\boldsymbol{k}) & 0 \end{bmatrix} & , \text{otherwise} \end{cases} , \tag{H.11}$$

where $f^{r',r}_{\beta\mu,\alpha\nu}(\boldsymbol{k}) \equiv \sum_n \tau^{r',r;\,n}_{\beta\mu,\alpha\nu} e^{-i\boldsymbol{k}\cdot\boldsymbol{\delta}^{r',r;\,n}_{\beta\mu,\alpha\nu}}$ for $\boldsymbol{\delta}^{r',r;\,n}_{\beta\mu,\alpha\nu} \equiv \boldsymbol{R}_{\boldsymbol{j}^{r'}\beta\mu} - \boldsymbol{R}_{\boldsymbol{i}^{r}\alpha\nu}$ the bond vector on the inequivalent bond n from orbital α in primitive cell ν of current cell r to orbital β in primitive cell μ of current cell r' for corresponding $\boldsymbol{i}^r$ and $\boldsymbol{j}^{r'}$.

Additionally, the matrices $\boldsymbol{H}^B_{\nu,\nu}(\boldsymbol{k})$ and $\boldsymbol{H}^B_{2,1}(\boldsymbol{k})$ can be simplified because of the hopping occuring between nearest neighbors only. Accordingly, many block matrices and matrix elements are equal to zero; explicitly,

$$\boldsymbol{H}^B_{\nu,\nu}(\boldsymbol{k}) = \begin{bmatrix} \boldsymbol{H}^{1,1}_{\nu,\nu}(\boldsymbol{k}) & \boldsymbol{H}^{2,1\,\dagger}_{\nu,\nu}(\boldsymbol{k}) & \boldsymbol{0} & \dots & \boldsymbol{0} & \boldsymbol{H}^{1,q}_{\nu,\nu}(\boldsymbol{k}) \\ \boldsymbol{H}^{2,1}_{\nu,\nu}(\boldsymbol{k}) & \boldsymbol{H}^{2,2}_{\nu,\nu}(\boldsymbol{k}) & \boldsymbol{H}^{3,2\,\dagger}_{\nu,\nu}(\boldsymbol{k}) & \boldsymbol{0} & \dots & \boldsymbol{0} \\ \boldsymbol{0} & \boldsymbol{H}^{3,2}_{\nu,\nu}(\boldsymbol{k}) & & & & \vdots \\ \vdots & \boldsymbol{0} & & \ddots & & \boldsymbol{0} \\ \boldsymbol{0} & \vdots & & & & \boldsymbol{H}^{q,q-1\,\dagger}_{\nu,\nu}(\boldsymbol{k}) \\ \boldsymbol{H}^{1,q\,\dagger}_{\nu,\nu}(\boldsymbol{k}) & \boldsymbol{0} & \dots & \boldsymbol{0} & \boldsymbol{H}^{q,q-1}_{\nu,\nu}(\boldsymbol{k}) & \boldsymbol{H}^{q,q}_{\nu,\nu}(\boldsymbol{k}) \end{bmatrix} , \tag{H.12a}$$

$$\boldsymbol{H}^B_{2,1}(\boldsymbol{k}) = \begin{bmatrix} \boldsymbol{H}^{1,1}_{2,1}(\boldsymbol{k}) & \boldsymbol{H}^{1,2}_{2,1}(\boldsymbol{k}) & \boldsymbol{0} & \dots & \boldsymbol{0} & \boldsymbol{0} \\ \boldsymbol{0} & \boldsymbol{H}^{2,2}_{2,1}(\boldsymbol{k}) & \boldsymbol{H}^{2,3}_{2,1}(\boldsymbol{k}) & \boldsymbol{0} & \dots & \boldsymbol{0} \\ \boldsymbol{0} & \boldsymbol{0} & & & & \vdots \\ \vdots & \boldsymbol{0} & & \ddots & & \boldsymbol{0} \\ \boldsymbol{0} & \vdots & & & & \boldsymbol{H}^{q-1,q}_{2,1}(\boldsymbol{k}) \\ \boldsymbol{H}^{q,1}_{2,1}(\boldsymbol{k}) & \boldsymbol{0} & \dots & \boldsymbol{0} & \boldsymbol{0} & \boldsymbol{H}^{q,q}_{2,1}(\boldsymbol{k}) \end{bmatrix} . \tag{H.12b}$$

In such a way, a set of only 4 matrices has to be found in order to obtain the matrix form of the full mean-field Hamiltonian in momentum space under an external magnetic field.

Many of the matrix elements are equal to zero. Explicitly, the matrices are given by

$$\begin{aligned}
\boldsymbol{H}^{r,r}_{\nu,\nu}(\boldsymbol{k}) &= \begin{bmatrix} \varepsilon_d & f^{r,r\,*}_{x\nu,d\nu}(\boldsymbol{k}) & f^{r,r\,*}_{y\nu,d\nu}(\boldsymbol{k}) \\ f^{r,r}_{x\nu,d\nu}(\boldsymbol{k}) & \varepsilon_p & f^{r,r\,*}_{y\nu,x\nu}(\boldsymbol{k}) \\ f^{r,r}_{y\nu,d\nu}(\boldsymbol{k}) & f^{r,r}_{y\nu,x\nu}(\boldsymbol{k}) & \varepsilon_p \end{bmatrix} \qquad \boldsymbol{H}^{r+1,r}_{\nu,\nu}(\boldsymbol{k}) = \begin{bmatrix} 0 & 0 & 0 \\ 0 & 0 & f^{r+1,r}_{x\nu,y\nu}(\boldsymbol{k}) \\ 0 & 0 & 0 \end{bmatrix} \\
\boldsymbol{H}^{r,r}_{2,1}(\boldsymbol{k}) &= \begin{bmatrix} 0 & 0 & f^{r,r}_{d2,y1}(\boldsymbol{k}) \\ f^{r,r}_{x2,d1}(\boldsymbol{k}) & 0 & f^{r,r}_{x2,y1}(\boldsymbol{k}) \\ 0 & 0 & 0 \end{bmatrix} \qquad \boldsymbol{H}^{r-1,r}_{2,1}(\boldsymbol{k}) = \begin{bmatrix} 0 & f^{r-1,r}_{d2,x1}(\boldsymbol{k}) & 0 \\ 0 & 0 & 0 \\ f^{r-1,r}_{y2,d1}(\boldsymbol{k}) & f^{r-1,r}_{y2,x1}(\boldsymbol{k}) & 0 \end{bmatrix}
\end{aligned} \tag{H.13}$$

where the matrix elements are equal to

$$f^{r,r}_{x\nu,d\nu}(\boldsymbol{k}) = -\left[t_{pd} + iR_{pd}(-1)^{\nu}\right] e^{i2\pi\chi\left[r+\frac{4\nu-1}{8}\right]} e^{-i\frac{a}{2\sqrt{2}}[k_x-k_y]}\,, \tag{H.14a}$$

$$f^{r,r}_{y\nu,d\nu}(\boldsymbol{k}) = \left[t_{pd} - iR_{pd}(-1)^{\nu}\right] e^{i2\pi\chi\left[r+\frac{4\nu+1}{8}\right]} e^{-i\frac{a}{2\sqrt{2}}[k_x+k_y]}\,, \tag{H.14b}$$

$$f^{r,r}_{y\nu,x\nu}(\boldsymbol{k}) = \left[t_{pp} - i\phi R_{pp}(-1)^{\nu}\right] e^{-i\frac{a}{\sqrt{2}}k_y}\,, \tag{H.14c}$$

$$f^{r+1,r}_{x\nu,y\nu}(\boldsymbol{k}) = \left[t_{pp} - i\phi R_{pp}(-1)^{\nu}\right] e^{-i\frac{a}{\sqrt{2}}k_y}\,, \tag{H.14d}$$

$$f^{r,r}_{x2,d1}(\boldsymbol{k}) = \left[t_{pd} - iR_{pd}\right] e^{-i2\pi\chi\left[r+\frac{5}{8}\right]} e^{i\frac{a}{2\sqrt{2}}[k_x-k_y]}\,, \tag{H.14e}$$

$$f^{r,r}_{d2,y1}(\boldsymbol{k}) = -\left[t_{pd} + iR_{pd}\right] e^{i2\pi\chi\left[r+\frac{7}{8}\right]} e^{-i\frac{a}{2\sqrt{2}}[k_x+k_y]}\,, \tag{H.14f}$$

$$f^{r,r}_{x2,y1}(\boldsymbol{k}) = -2\begin{bmatrix} t_{pp}\cos\left\{\frac{a}{\sqrt{2}}k_x - 4\pi\chi\left[r+\frac{3}{4}\right]\right\} \\ +\phi R_{pp}\sin\left\{\frac{a}{\sqrt{2}}k_x - 4\pi\chi\left[r+\frac{3}{4}\right]\right\} \end{bmatrix}\,, \tag{H.14g}$$

$$f^{r-1,r}_{y2,d1}(\boldsymbol{k}) = -\left[t_{pd} + iR_{pd}\right] e^{-i2\pi\chi\left[r+\frac{3}{8}\right]} e^{i\frac{a}{2\sqrt{2}}[k_x+k_y]}\,, \tag{H.14h}$$

$$f^{r-1,r}_{d2,x1}(\boldsymbol{k}) = \left[t_{pd} - iR_{pd}\right] e^{i2\pi\chi\left[r+\frac{1}{8}\right]} e^{-i\frac{a}{2\sqrt{2}}[k_x-k_y]}\,, \tag{H.14i}$$

$$f^{r-1,r}_{y2,x1}(\boldsymbol{k}) = -2\begin{bmatrix} t_{pp}\cos\left\{\frac{a}{\sqrt{2}}k_x - 4\pi\chi\left[r+\frac{1}{4}\right]\right\} \\ -\phi R_{pp}\sin\left\{\frac{a}{\sqrt{2}}k_x - 4\pi\chi\left[r+\frac{1}{4}\right]\right\} \end{bmatrix}\,. \tag{H.14j}$$

REFERENCES

[1] Y. Ando. Topological insulator materials. *Journal of the Physical Society of Japan*, 82(10):102001, 2013.

[2] N. P. Armitage, P. Fournier, and R. L. Greene. Progress and perspectives on electron-doped cuprates. *Rev. Mod. Phys.*, 82:2421–2487, Sep 2010.

[3] J. Bardeen, L. N. Cooper, and J. R. Schrieffer. Theory of superconductivity. *Phys. Rev.*, 108:1175–1204, Dec 1957.

[4] J. G. Bednorz and K. A. Müller. Possible high t_c superconductivity in the balacuo system. *Zeitschrift für Physik B Condensed Matter*, 64(2):189–193, Jun 1986.

[5] M. V. Berry. Quantal phase factors accompanying adiabatic changes. *Proceedings of the Royal Society of London. Series A, Mathematical and Physical Sciences*, 392(1802):45–57, 1984.

[6] M. Born and V. Fock. Beweis des adiabatensatzes. *Zeitschrift für Physik*, 51(3):165–180, Mar 1928.

[7] S. Bulut, A. P. Kampf, and W. A. Atkinson. Instability towards staggered loop currents in the three-orbital model for cuprate superconductors. *Phys. Rev. B*, 92:195140, Nov 2015.

[8] S. Chakravarty. Quantum oscillations and key theoretical issues in high temperature superconductors from the perspective of density waves. *Reports on Progress in Physics*, 74(2):022501, 2011.

[9] S. Chakravarty. Quantum oscillations and key theoretical issues in high temperature superconductors from the perspective of density waves. *Reports on Progress in Physics*, 74(2):022501, 2011.

[10] S. Chakravarty, R. B. Laughlin, D. K. Morr, and C. Nayak. Hidden order in the cuprates. *Phys. Rev. B*, 63:094503, Jan 2001.

[11] M. C. Chang. Chapter 9: Fermi surfaces and metals. Course Slides, Feb 2013. `http://phy.ntnu.edu.tw/~changmc/Teach/SS/SS_note/chap09.pdf`.

[12] A. I. Coldea. Quantum oscillations probe the normal electronic states of novel superconductors. *Philosophical Transactions of the Royal Society of London A: Mathematical, Physical and Engineering Sciences*, 368(1924):3503–3517, 2010.

[13] N. Doiron-Leyraud, T. Szkopek, T. Pereg-Barnea, C. Proust, and G. Gervais. Berry phase in cuprate superconductors. *Phys. Rev. B*, 91:245136, Jun 2015.

[14] J. Eun, Z. Wang, and S. Chakravarty. Quantum oscillations in yba2cu3o6+ from period-8 d-density wave order. *Proceedings of the National Academy of Sciences*, 109(33):13198–13203, 2012.

[15] B. Fauqué, Y. Sidis, V. Hinkov, S. Pailhès, C. T. Lin, X. Chaud, and P. Bourges. Magnetic order in the pseudogap phase of high-T_C superconductors. *Phys. Rev. Lett.*, 96:197001, May 2006.

[16] J. Fuchs, Piéchon, M. O. F., Goerbig, and G. Montambaux. Topological berry phase and semiclassical quantization of cyclotron orbits for two dimensional electrons in coupled band models. *The European Physical Journal B*, 77(3):351–362, 2010.

[17] M. O. Goerbig, G. Montambaux, and F. Piéchon. Measure of diracness in two-dimensional semiconductors. *EPL (Europhysics Letters)*, 105(5):57005, 2014.

[18] M. Hashimoto, I. M. Vishik, R.-H. He, T. P. Devereaux, and Z.-X. Shen. Energy gaps in high-transition-temperature cuprate superconductors. *Nature Physics*, 10:483 – 495, 06 2014.

[19] M. S. Hybertsen, M. Schlüter, and N. E. Christensen. Calculation of coulomb-interaction parameters for la_2cuo_4 using a constrained-density-functional approach. *Phys. Rev. B*, 39:9028–9041, May 1989.

[20] T. Kato. On the adiabatic theorem of quantum mechanics. *Journal of the Physical Society of Japan*, 5(6):435–439, 1950.

[21] C. Kittel and P. McEuen. *Introduction to Solid State Physics*. John Wiley & Sons, Limited, 2018.

[22] L. D. Landau and E. M. Lifshitz. *Quantum Mechanics: Non-Relativistic Theory*, volume 3 of *Course of Theoretical Physics*. Pergamon Press, 1965.

[23] R. B. Laughlin. Hiawatha's valence bonding. *Ann. Improbable Res.*, 10(physics/0408066. 6):8, 2004.

[24] Y. Li, V. Balédent, N. Barišić, Y. C. Cho, Y. Sidis, G. Yu, X. Zhao, P. Bourges, and M. Greven. Magnetic order in the pseudogap phase of $hgba_2cuo_{4+\delta}$ studied by spin-polarized neutron diffraction. *Phys. Rev. B*, 84:224508, Dec 2011.

[25] Y. Li, V. Balédent, N. Barišić, Y. Cho, B. Fauqué, Y. Sidis, G. Yu, X. Zhao, P. Bourges, and M. Greven. Unusual magnetic order in the pseudogap region of the superconductor hgba2cuo4+. *Nature*, 455:372 EP –, 09 2008.

[26] H. C. Longuet-Higgins, U. Öpik, M. H. L. Pryce, and R. A. Sack. Studies of the jahn-teller

effect. ii. the dynamical problem. *Proceedings of the Royal Society of London A: Mathematical, Physical and Engineering Sciences*, 244(1236):1–16, 1958.

[27] J. M. Luttinger. The effect of a magnetic field on electrons in a periodic potential. *Phys. Rev.*, 84:814–817, Nov 1951.

[28] S. Martin, A. T. Fiory, R. M. Fleming, L. F. Schneemeyer, and J. V. Waszczak. Normal-state transport properties of $bi_{2+x}sr_{2-y}cuo_{6+\delta}$ crystals. *Phys. Rev. B*, 41:846–849, Jan 1990.

[29] G. Massarelli. Determination of berry's phase in d-density-wave model of the pseudogap in the cuprates. Master's thesis, McGill University, Montreal, 2016.

[30] G. P. Mikitik and Y. V. Sharlai. Manifestation of berry's phase in metal physics. *Phys. Rev. Lett.*, 82:2147–2150, Mar 1999.

[31] H. K. Nguyen and S. Chakravarty. Effects of magnetic field on the d-density-wave order in the cuprates. *Phys. Rev. B*, 65:180519, May 2002.

[32] M. R. Norman, D. Pines, and C. Kallin. The pseudogap: friend or foe of high t_c? *Advances in Physics*, 54(8):715–733, 2005.

[33] L. Onsager. Interpretation of the de haas-van alphen effect. *The London, Edinburgh, and Dublin Philosophical Magazine and Journal of Science*, 43(344):1006–1008, 1952.

[34] S. Pancharatnam. Generalized theory of interference and its applications. *Proceedings of the Indian Academy of Sciences - Section A*, 44(6):398–417, Dec 1956.

[35] L. Pauling and E. Wilson. *Introduction to Quantum Mechanics with Applications to Chemistry*. Dover Publications, 2012.

[36] V. M. Pudalov. David shoenberg and the beauty of quantum oscillations. *Low Temperature Physics*, 37(1):8–18, 2011.

[37] J. W. S. B. Rayleigh. *The Theory of Sound*. Number 1 in The Theory of Sound. Macmillan, 1894.

[38] R. Resta. Polarization as a berry phase. *Europhys. News*, 28(1):18–20, 1997.

[39] L. M. Roth. Semiclassical theory of magnetic energy levels and magnetic susceptibility of bloch electrons. *Phys. Rev.*, 145:434–448, May 1966.

[40] J. Sakurai and J. Napolitano. *Modern Quantum Mechanics*. . Addison-Wesley, 2011.

[41] A. Saxena. *High-Temperature Superconductors*. Springer Series in Materials Science. Springer Berlin Heidelberg, 2012.

[42] E. Schrödinger. Quantisierung als eigenwertproblem. *Annalen der Physik*, 385(13):437–490,

1926.

[43] S. E. Sebastian, N. Harrison, and G. G. Lonzarich. Towards resolution of the fermi surface in underdoped high-t_c superconductors. *Reports on Progress in Physics*, 75(10):102501, 2012.

[44] D. Shoenberg. *Magnetic Oscillations in Metals*. Cambridge Monographs on Physics. Cambridge University Press, 2009.

[45] Y. Sidis and P. Bourges. Evidence for intra-unit-cell magnetic order in the pseudo-gap state of high-t c cuprates. *Journal of Physics: Conference Series*, 449(1):012012, 2013.

[46] J. C. Solem and L. C. Biedenharn. Understanding geometrical phases in quantum mechanics: An elementary example. *Foundations of Physics*, 23(2):185–195, Feb 1993.

[47] T. Thonhauser, D. Ceresoli, D. Vanderbilt, and R. Resta. Orbital magnetization in periodic insulators. *Phys. Rev. Lett.*, 95:137205, Sep 2005.

[48] J. Townsend. *A Modern Approach to Quantum Mechanics*. University Science Books, 2012.

[49] C. Varma, S. Schmitt-Rink, and E. Abrahams. Charge transfer excitations and superconductivity in "ionic" metals. *Solid State Communications*, 62(10):681 – 685, 1987.

[50] C. M. Varma. Non-fermi-liquid states and pairing instability of a general model of copper oxide metals. *Phys. Rev. B*, 55:14554–14580, Jun 1997.

[51] C. M. Varma. Pseudogap phase and the quantum-critical point in copper-oxide metals. *Phys. Rev. Lett.*, 83:3538–3541, Oct 1999.

[52] C. M. Varma. Theory of the pseudogap state of the cuprates. *Phys. Rev. B*, 73:155113, Apr 2006.

[53] J. Xia, E. Schemm, G. Deutscher, S. A. Kivelson, D. A. Bonn, W. N. Hardy, R. Liang, W. Siemons, G. Koster, M. M. Fejer, and A. Kapitulnik. Polar kerr-effect measurements of the high-temperature $yba_2cu_3o_{6+x}$ superconductor: Evidence for broken symmetry near the pseudogap temperature. *Phys. Rev. Lett.*, 100:127002, Mar 2008.

[54] D. Xiao, M.-C. Chang, and Q. Niu. Berry phase effects on electronic properties. *Rev. Mod. Phys.*, 82:1959–2007, Jul 2010.

[55] J. Zak. Berry's phase for energy bands in solids. *Phys. Rev. Lett.*, 62:2747–2750, Jun 1989.

[56] Y. Zhang, Y.-W. Tan, H. L. Stormer, and P. Kim. Experimental observation of the quantum hall effect and berry's phase in graphene. *Nature*, 438:201–204, 11 2005.